TECHNISCHE UNIVERSITÄT DRESDEN

Mathematik und Naturwissenschaften Experimentalphysik, Institut für Kern- und Teilchenphysik

Validation of Monte Carlo samples and sensitivity studies of sensitive observables to the quartic Higgs-self-coupling parameter $\kappa_{2\mathrm{V}}$

Jonas Wagner

Master-Arbeit

TECHNISCHE UNIVERSITÄT DRESDEN

Mathematik und Naturwissenschaften Experimentalphysik, Institut für Kern- und Teilchenphysik

Validation of Monte Carlo samples and sensitivity studies of sensitive observables to the quartic Higgs-self-coupling parameter $\kappa_{2\mathrm{V}}$

Jonas Wagner

Geboren am: 29.05.1997 in Bad Muskau
Matrikelnummer: 4608118
Immatrikulationsjahr: 2021

Master-Arbeit

zur Erlangung des akademischen Grades

Master of Science (M.Sc.)

Betreuer

Dr. Frank Siegert
Prof. Arno Straessner

Eingereicht am: 30.07.2025

Zusammenfassung

In dieser Arbeit wird der Prozess $\mathrm{jj} \rightarrow \mathrm{W}^{\pm}\mathrm{W}^{\pm}\mathrm{hjj}$ im Hinblick auf den quartischen Kopplungsvertex WWhh untersucht. Ziel ist es einerseits, die beiden Monte-Carlo-Eventgeneratoren MadGraph und Sherpa hinsichtlich der von ihnen erzeugten Datensätze für diesen Prozess miteinander zu vergleichen. Andererseits soll das Verhalten sensitiver Observablen unter Variation des Kopplungsparameters $\kappa_{2\mathrm{V}}$ analysiert werden.

Dies geschieht zum einen anhand ausgewählter Observablen, die später als Grundlage für das Training eines Deep Neural Networks (DNN) zur Identifikation von Monte-Carlo-Samples mit abweichenden Werten von $\kappa_{2\mathrm{V}}$ dienen sollen. Zum anderen werden charakteristische Unterschiede zwischen den Generatoren auf Basis signalrelevanter Observablen identifiziert. Abschließend wird ein kurzer Ausblick auf das Verhalten des Signalprozesses bei einer Schwerpunktsenergie von $100\,\mathrm{TeV}$ gegeben.

Es konnte der Einfluss verschiedener Werte des Kopplungsparameters $\kappa_{2\mathrm{V}}$ auf den totalen Wirkungsquerschnitt des Prozesses sowohl veranschaulicht als auch quantifiziert werden. Zudem wurden die Sensitivitäten einzelner Observablen gegenüber $\kappa_{2\mathrm{V}}$ sowie Unterschiede zwischen den jeweils von MadGraph und Sherpa erzeugten Datensätzen herausgearbeitet.

Abstract

This work investigates the process $\mathrm{jj} \to \mathrm{W}^{\pm}\mathrm{W}^{\pm}\mathrm{hjj}$ with a focus on the quartic coupling vertex WWhh. The first objective is to compare the Monte Carlo event generators MadGraph and Sherpa in terms of the datasets they produce for this process.

Furthermore, the behavior of sensitive observables is studied as a function of the coupling parameter $\kappa_{2\mathrm{V}}$. On the one hand, selected observables are analyzed as a basis for training a Deep Neural Network (DNN) aimed at identifying Monte Carlo samples with anomalous values of $\kappa_{2\mathrm{V}}$. On the other hand, differences between the generators are explored using observables that are strongly correlated with the signal process.

In addition, a brief outlook is provided on the behavior of the signal process at a center-of-mass energy of $100\,\mathrm{TeV}$.

The impact of varying the coupling parameter $\kappa_{2\mathrm{V}}$ on the total cross section of the process is illustrated and quantified. Moreover, the sensitivity of individual observables to changes in $\kappa_{2\mathrm{V}}$, as well as the discrepancies between the datasets generated by MadGraph and Sherpa, are examined in detail.

Inhaltsverzeichnis

1 Introduction

The Higgs boson, the latest elementary particle added to the Standard Model of particle physics, was an important step in refining our understanding of fundamental interactions. Its discovery was the result of decades of intense theoretical and experimental efforts, that included the contributions of over 60 nations and thousands of scientists across the Large Hadron Collider's two main experiments, ATLAS and CMS. The theoretical framework for the Higgs mechanism was developed by Brout, Englert, and Higgs in the early 1960s, providing a mechanism to explain how particles acquire mass through spontaneous symmetry breaking. This prediction could finally be confirmed in July of 2012, marking a monumental milestone in particle physics.

The Higgs boson discovery addressed several critical issues that had long challenged the field, such as unitarity violations in longitudinal W-boson scattering and the origin of mass for gauge bosons and fermions. However, despite these breakthroughs, some open questions still remain after all. Notably, the hierarchy problem, which describes the circumstance of the Higgs mass being much lighter than the Planck scale despite quantum corrections. Furthermore, alternative theories such as composite Higgs models propose that the Higgs is not an elementary particle but rather a bound state arising from a new type of interaction [19]. Other pressing questions include the nature of electroweak symmetry breaking and the exact shape of the Higgs potential, which relates directly to vacuum stability and the fate of our universe.

One promising approach to probing the Higgs sector is through the kappa-framework, which parametrizes possible deviations of Higgs couplings from their Standard Model predictions and compares them systematically with the corresponding values measured in experimental data. For example, the triple Higgs self-coupling provides crucial insights into the above mentioned shape of the Higgs potential. The quartic gauge-Higgs coupling, which is also the focus in this thesis, is connected to testing the gauge cancellations predicted by the Standard Model. It can be an indicator of new physics phenomena beyond current theories, given that any deviations were to be observed.

Most recently the CMS collaboration has been able to set new certainty limits on the quartic gauge coupling modifier $\kappa_{2\mathrm{V}}$ of [0.40,1.60] [2] which are the tightest limits for $\kappa_{2\mathrm{V}}$ yet.

To interpret these experimental results accurately and compare them with theoretical expectations, Monte Carlo event generators play a crucial role. These generators are well-established computational tools widely used in high-energy physics, to simulate particle collisions by modeling both the hard scattering processes and subsequent parton showering, hadronization, and detector effects. A variety of Monte Carlo generators are available, with prominent examples including MadGraph, Sherpa, and POWHEG, each employing different methods and approximations. Since these generators can yield varying predictions for the same physical processes, it is essential to perform detailed cross-comparisons between them.

This thesis is organized as follows. First, there will be an introduction on the theoretical background, covering the electroweak theory within the Standard Model leading over into the Higgs mechanism, the characteristics of vector boson scattering (VBS) and a discussion of the signal process $\mathrm{jj} \rightarrow \mathrm{W}^{\pm}\mathrm{W}^{\pm}\mathrm{hjj}$, finishing with an overview of the statistical data analysis based on histogramming. Next there will be a short introduction on the Large Hadron Collider and the ATLAS detector, aiming to provide a relation to the real world experimental setup, as well as the fundamentals of matrix element generation and Monte Carlo event generation, being more connected to the simulation side.

Following this, the Monte Carlo generator configurations used in this work are presented, focusing on Sherpa and MadGraph samples, their generation parameters, and the analysis framework employed via Rivet. The core results section then provides a validation of the Sherpa, the Sherpa with an UFO-model implementation and MadGraph Standard Model predictions, presents a comparison of cross-section measurements for varying values of the quartic gauge-Higgs coupling modifier $\kappa_{2\mathrm{V}}$, and afterwards evaluates observables of different complexity regarding these different values of $\kappa_{2\mathrm{V}}$. In the end a brief study of event samples generated at a future 100 TeV center-of-mass energy under varying values of $\kappa_{2\mathrm{V}}$ will be performed.

2 Theoretical Background

In the following chapters, a first introduction to the electroweak theory within the Standard Model shall be provided. Based on that, the Higgs-Mechanism will be step by step introduced from a toy model approach up to the formulation within the Standard Model. For the research of this chapter, Ref. [32] was used. At the end of the discussion, the origin of the Higgs coupling modifier $\kappa_{2\mathrm{V}}$ will be derived. Afterwards there will be a characterization of the Vector boson scattering as a base for the signal process to be discussed in this thesis and ,following that, said signal process, being $\mathrm{jj} \rightarrow \mathrm{W}^{\pm}\mathrm{W}^{\pm}\mathrm{hjj}$, will be introduced. In the final section, a short introduction on the topic of histograms, as the main analysis tool in this thesis, will be given.

2.1 The Electroweak Theory within the Standard Model

The Standard Model of particle physics is a relativistic quantum field theory. It includes three of the four known fundamental forces: the electroweak interaction, unifying quantum electro dynamics (QED) and the weak theory, and quantum chromo dynamics (QCD), while gravity is excluded. The three forces covered by it can be theoretically described by Yang-Mills theories, which are local, non-abelian gauge theories. Those allow the prediction of some interesting properties of the gauge fields, for example the number of involved exchange bosons or the self-interaction of some of these bosons. The interactions are linked to different symmetry groups, e.g. the $\mathrm{U}(1)_{\mathrm{Y}} \times \mathrm{SU}(2)_{\mathrm{L}}$-groups generate the unified electroweak interaction and the $\mathrm{SU}(3)_{\mathrm{C}}$ the strong interaction. Therefore the Standard Model's gauge properties are formed by the product of all its inherent symmetry groups, yielding

$$\mathrm{U}(1)_{\mathrm{Y}} \otimes \mathrm{SU}(2)_{\mathrm{L}} \otimes \mathrm{SU}(3)_{\mathrm{C}} \tag{2.1}$$

with the first two groups $\mathrm{U}(1)_{\mathrm{Y}} \otimes \mathrm{SU}(2)_{\mathrm{L}}$ on their own representing the electroweak sector. The index next to the group notation refers to its corresponding generator, like the electromagnetic part has the weak hypercharge Y as its generator, which is simply a scalar value. The $\mathrm{SU}(2)$ generator of the weak interaction is the set of the three Pauli-matrices,

$$\sigma_1 = \begin{pmatrix} 0 & 1 \\ 1 & 0 \end{pmatrix} , \quad \sigma_2 = \begin{pmatrix} 0 & -\mathrm{i} \\ \mathrm{i} & 0 \end{pmatrix} , \quad \sigma_3 = \begin{pmatrix} 1 & 0 \\ 0 & -1 \end{pmatrix} \tag{2.2}$$

while the QCD's $\mathrm{SU}(3)$-group is constructed by the eight Gell-Mann matrices. Considering all these gauge structures, any transformation within the Standard Model can be formulated as

$$\psi \rightarrow \psi' = \exp\left[\mathrm{ig}\sum_{\mathrm{a}} \theta^{\mathrm{a}}(\mathrm{x}) \cdot \mathrm{T}^{\mathrm{a}}\right] \psi(\mathrm{x}) \tag{2.3}$$

with $\mathrm{T^a}$ being one of the aforementioned generators, g is a gauge-coupling strength and $\theta(\mathrm{x})$ being a local phase.

In the Wu experiment 1957 [34], it has been shown, that the weak interaction violates parity. This means that for the coupling of a weak gauge boson to a fermion, the fermion's chirality has to be considered. Weak gauge bosons only couple to left-handed particles or right-handed antiparticles. The 2×2 structure of the Pauli-matrices imply a wavefunction with 2 components, in this case a doublet in the charge of the weak interaction, the weak isospin $\mathrm{I_W}$. Each component has in total an isospin of $\mathrm{I_W} = \frac{1}{2}$, but the third component of the weak isospin is either $\mathrm{I_W^{(3)}} = \frac{1}{2}$ for the upper component or $\mathrm{I_W^{(3)}} = -\frac{1}{2}$ for the lower one. Left-handed antiparticles and right-handed particles cannot interact via the weak force and therefore are presented as weak isospin singlets. A full set of electroweak fields, associated to the symmetry of their gauge group, would look like

$$\mathrm{SU(2)} \Rightarrow \varphi(\mathrm{x}) = \begin{pmatrix} \nu_\mathrm{l} \\ \mathrm{l}^- \end{pmatrix}_\mathrm{L}, \begin{pmatrix} \mathrm{q_u} \\ \mathrm{q_{d'}} \end{pmatrix}_\mathrm{L}, \begin{pmatrix} \overline{\nu_\mathrm{l}} \\ \mathrm{l}^+ \end{pmatrix}_\mathrm{R}, \begin{pmatrix} \overline{\mathrm{q}}_\mathrm{u} \\ \overline{\mathrm{q}}_\mathrm{d'} \end{pmatrix}_\mathrm{R}$$
$$\mathrm{U(1)} \Rightarrow \varphi(\mathrm{x}) = (\bar{\mathrm{l}})_\mathrm{L}, (\overline{\nu_\mathrm{l}})_\mathrm{L}, (\bar{\mathrm{q}})_\mathrm{L}, (\mathrm{l})_\mathrm{R}, (\nu_\mathrm{l})_\mathrm{R}, (\mathrm{q})_\mathrm{R}.$$

Here, „l "denotes a lepton, ν_l denotes its corresponding neutrino and $\mathrm{q_u}$ and $\mathrm{q_d}$ denote up- and down-type quarks. Both, the leptons and quarks come in threefold family replication. The different generators of the forces already hint how differently the corresponding fields are influenced by their symmetries. Applying a local gauge transformation to a fermion, being a singlet in the electromagnetic field, only changes its phase, but it doesn't change any other properties of it. In the cases of the weak theory or QCD this is not necessarily the case. Furthermore it links the matrix-type of the generators to the non-abelian property of the corresponding gauge groups, which causes the weak and strong gauge bosons to be able to interact with each another. Since the electroweak section of the Standard Model is of much more interest for this work, further examinations of the QCD mechanism will be mostly left out from this point on.

Formulating the gauge transformation for the electroweak interaction, regarding (2.3) yields

$$\varphi(\mathrm{x}) \to \varphi'(\mathrm{x}) = \exp\left[\mathrm{i g_w} \boldsymbol{\theta}(\mathrm{x}) \mathbf{T}\right] \varphi(\mathrm{x}). \tag{2.4}$$

To ensure local gauge invariance three gauge fields are required in the $\mathrm{SU(2)}$-symmetry, $\mathrm{W^{(1)}}, \mathrm{W^{(2)}}, \mathrm{W^{(3)}}$. These are not yet the physical weak gauge bosons $\mathrm{W^\pm}$ and Z, but eigenstates they can be constructed from, like

$$\mathrm{W}_\mu^\pm = \frac{1}{\sqrt{2}} \left(\mathrm{W}_\mu^{(1)} \mp \mathrm{i W}_\mu^{(2)} \right) \tag{2.5}$$

The $\mathrm{U(1)}$-Symmetry only needs one gauge field, which will be denoted as B_μ. At this point, the fields $\mathrm{W^{(3)}}$ and B_μ are mixed, so they do not propagate as independent fields at this point. With a new diagonalized basis, it is possible to extract the physical fields Z_μ, which corresponds to the Z-boson, and A_μ, which represents the photon. They are described as a linear combination of B_μ and $\mathrm{W^{(3)}}$ like

$$\mathrm{A}_\mu = \frac{\mathrm{g' W^{(3)} + g_W B_\mu}}{\sqrt{\mathrm{g_W^2 + g'^2}}} \tag{2.6}$$

$$\mathrm{Z}_\mu = \frac{\mathrm{g_W W^{(3)} - g' B_\mu}}{\sqrt{\mathrm{g_W^2 + g'^2}}} \tag{2.7}$$

or with the weak mixing angle θ_W like

$$\mathrm{A}_\mu = \cos\theta_\mathrm{W} \mathrm{B}_\mu + \sin\theta_\mathrm{W} \mathrm{W}_\mu^{(3)} \quad , \quad \mathrm{Z}_\mu = -\sin\theta_\mathrm{W} \mathrm{B}_\mu + \cos\theta_\mathrm{W} \mathrm{W}_\mu^{(3)}. \tag{2.8}$$

The resulting Lagrangian for the electroweak sector of the Standard Model comes out to be

$$\begin{aligned}\mathcal{L}_{\mathrm{EW}} =& \mathrm{i}\begin{pmatrix}\overline{\nu_\mathrm{l}}\\ \mathrm{l}^+\end{pmatrix}_\mathrm{R}\gamma^\mu \mathrm{D}_\mu\begin{pmatrix}\nu_\mathrm{l}\\ \mathrm{l}\end{pmatrix}_\mathrm{L} + \begin{pmatrix}\overline{\mathrm{q}}_\mathrm{u}\\ \overline{\mathrm{q}}_{\mathrm{d}'}\end{pmatrix}_\mathrm{R}\gamma^\mu \mathrm{D}_\mu\begin{pmatrix}\mathrm{q}_\mathrm{u}\\ \mathrm{q}_{\mathrm{d}'}\end{pmatrix}_\mathrm{L}\\ &+\mathrm{i}(\mathrm{l}^+)_\mathrm{L}\gamma^\mu \mathrm{D}_\mu(\mathrm{l})_\mathrm{R}+\mathrm{i}(\overline{\mathrm{q}}_\mathrm{d})_\mathrm{L}\gamma^\mu \mathrm{D}_\mu(\mathrm{q}_\mathrm{d})_\mathrm{R}+\mathrm{i}(\overline{\mathrm{q}}_\mathrm{u})_\mathrm{L}\gamma^\mu \mathrm{D}_\mu(\mathrm{q}_\mathrm{u})_\mathrm{R}\\ &-\frac{1}{4}\mathrm{W}^\mathrm{a}_{\mu\nu}\mathrm{W}^{\mathrm{a},\mu\nu}-\frac{1}{4}\mathrm{F}_{\mu\nu}\mathrm{F}^{\mu\nu}.\end{aligned} \tag{2.9}$$

The notation of l and q is used as a stand in to represent every generation quarks and leptons and was chosen for the sake of saving space. The fields $\mathrm{W}^\mathrm{a}_{\mu\nu}$ and $\mathrm{F}_{\mu\nu}$ each represent the covariant field strength tensors of the corresponding symmetry groups. $\mathrm{W}^\mathrm{a}_{\mu\nu}$ is the field strength tensor for the $\mathrm{SU}(2)$ and $\mathrm{F}_{\mu\nu}$ the one for the $\mathrm{U}(1)$. They are defined like

$$\begin{aligned}\mathrm{F}_{\mu\nu} &= \partial_\mu \mathrm{B}_\nu - \partial_\nu \mathrm{B}_\mu\\ \mathrm{W}^\mathrm{a}_{\mu\nu} &= \partial_\mu \mathrm{W}^\mathrm{a}_\nu - \partial_\nu \mathrm{W}^\mathrm{a}_\mu - \mathrm{g_W}\mathrm{f}^{\mathrm{abc}}\mathrm{W}^\mathrm{b}_\mu \mathrm{W}^\mathrm{c}_\nu\end{aligned} \tag{2.10}$$

2.2 The Higgs-Mechanism

The Higgs-Mechanism is described as a quantum field theory. To start, let's set up the Lagrangian density of the Higgs formalism with the real scalar field φ:

$$\mathcal{L} = \frac{1}{2}(\partial_\mu\varphi)(\partial^\mu\varphi) - \mathrm{V}(\varphi) = \frac{1}{2}(\partial_\mu\varphi)(\partial^\mu\varphi) - \frac{1}{2}\mu^2\varphi^2 - \frac{1}{4}\lambda\varphi^4 \tag{2.11}$$

The left side of the sum can be interpreted as the kinetic term T and the right side as the potential term V.

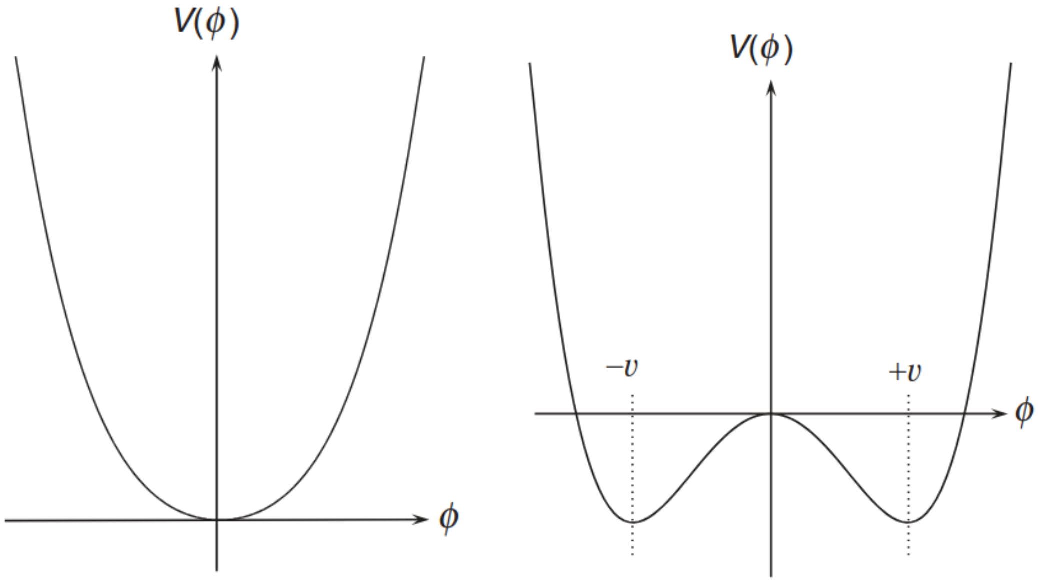

Abbildung 2.1: The unbroken (left) and broken (right) Higgs potentials for a real scalar field. [32]

The coefficients μ and λ are of crucial value for the further discussion, since they determine the location of the minimum of the potential and the associated value of the scalar field φ, the so-called vacuum expectation value v.If both coefficients are positive, it results in a global minimum of the potential at $\varphi = 0$. If $\mu^2 < 0$ while at the same time $\lambda > 0$, the potential splits into two separate minima, meaning $\varphi_0 = \pm\mathrm{v}$. Considering the potential term V in 2.11, the location of the minima, and thereby the value of v, can then be calculated to be

$$\varphi = \pm\mathrm{v} = \pm\left|\sqrt{\frac{-\mu^2}{\lambda}}\right| \tag{2.12}$$

By making the scalar field φ chose between one of these two degenerate ground states, the symmetry of the Lagrangian is spontaneously broken. If one vacuum state is chosen (for the further discussion assume it's $\varphi = +\mathrm{v}$), the resulting particle states can be attained by applying a perturbation theory around the minimum. So the scalar field φ can now be described by the expression $\varphi(\mathrm{x}) = \mathrm{v} + \mathrm{h}(\mathrm{x})$, where $\mathrm{h}(\mathrm{x})$ is the excitation along the Higgs potential. With that adjustment, the Lagrangian changes to

$$\mathcal{L} = \frac{1}{2}(\partial_\mu \mathrm{h})(\partial^\mu \mathrm{h}) - \frac{1}{2}\mu^2(\mathrm{v}+\mathrm{h})^2 - \frac{1}{4}\lambda(\mathrm{v}+\mathrm{h})^4 \tag{2.13}$$

When performing all the necessary multiplications and also using (2.12) to gain the relation $\mu^2 = -\lambda 2$, it is possible to further simplify the Lagrangian to

$$\mathcal{L} = \frac{1}{2}(\partial_\mu \mathrm{h})(\partial^\mu \mathrm{h}) + \frac{1}{4}\lambda\mathrm{v}^4 - \lambda\mathrm{v}^2\mathrm{h}^2 - \lambda\mathrm{v}\mathrm{h}^3 - \frac{1}{4}\lambda\mathrm{h}^4 \tag{2.14}$$

When investigating the resulting formula, the non-kinetic terms of the Lagrangian organized as follows: The terms connected to the third and fourth power of h are interaction terms, yielding triple and quartic self-interaction vertices of the scalar-field, while $-\lambda\mathrm{v}\mathrm{h}^3$ can be interpreted as a mass term. The left term of $\frac{1}{4}\lambda\mathrm{v}^4$ is simply a constant and therefore not of any deeper physical meaning.
In the next step, the aforementioned scalar field φ will no longer be assumed to be real, but to also have a complex part. Under this the assumption, the theory extends in the following way. The complex scalar field is denoted as

$$\varphi = \frac{1}{\sqrt{2}}\left(\varphi_1 + \mathrm{i}\varphi_2\right) \tag{2.15}$$

and thus the Lagrangian transforms to

$$\mathcal{L} = \frac{1}{2}\left(\partial_\mu\varphi_1\right)\left(\partial^\mu\varphi_1\right) + \frac{1}{2}\left(\partial_\mu\varphi_2\right)\left(\partial^\mu\varphi_2\right) - \frac{1}{2}\mu^2\left(\varphi_1^2 + \varphi_2^2\right) - \frac{1}{4}\lambda^2\left(\varphi_1^2 + \varphi_2^2\right)^2. \tag{2.16}$$

As in the case for the real scalar field, the next step is to describe the fields $(\varphi_1^{(0)}, \varphi_2^{(0)})$ as excitations η and ξ around the minimum of $\varphi(\mathrm{x})$. If, again, by choosing the vacuum state conveniently and without loss of generality, to be $(\varphi_1^{(0)}, \varphi_2^{(0)}) = (\mathrm{v}, 0)$, the resulting fields can be expressed as follows.

$$\varphi_1(\mathrm{x}) = \eta(\mathrm{x}) + \mathrm{v}\,, \varphi_2(\mathrm{x}) = \xi(\mathrm{x}) \Rightarrow \Phi = \frac{1}{\sqrt{2}}\left(\eta(\mathrm{x}) + \mathrm{i}\xi(\mathrm{x}) + \mathrm{v}\right) \tag{2.17}$$

Thus the Lagrangian for a complex scalar field results to be

$$\mathcal{L} = \frac{1}{2}(\partial_\mu\eta)(\partial^\mu\eta) + \frac{1}{2}(\partial_\mu\xi)(\partial^\mu\xi) - \mathrm{V}(\eta,\xi) \tag{2.18}$$

$$\begin{aligned}\mathrm{V}(\eta,\xi) &= \mu^2\varphi^2 + \lambda\varphi^4 \\ &= -\frac{1}{4}\lambda\mathrm{v}^4 + \lambda\mathrm{v}^2\eta^2 + \lambda\mathrm{v}\eta^3 + \frac{1}{4}\lambda\eta^4 + \frac{1}{4}\lambda\xi^4 + \lambda\mathrm{v}\eta\xi^2 + \frac{1}{2}\lambda\eta^2\xi^2.\end{aligned} \tag{2.19}$$

When investigating 2.19, not regarding the constant term $-\frac{1}{4}\lambda\mathrm{v}^4$ or the mass term $\lambda\mathrm{v}^2\eta^2$, several different types of interactions, consisting of triple and quartic vertices, and their corresponding couplings are predicted by the new potential.

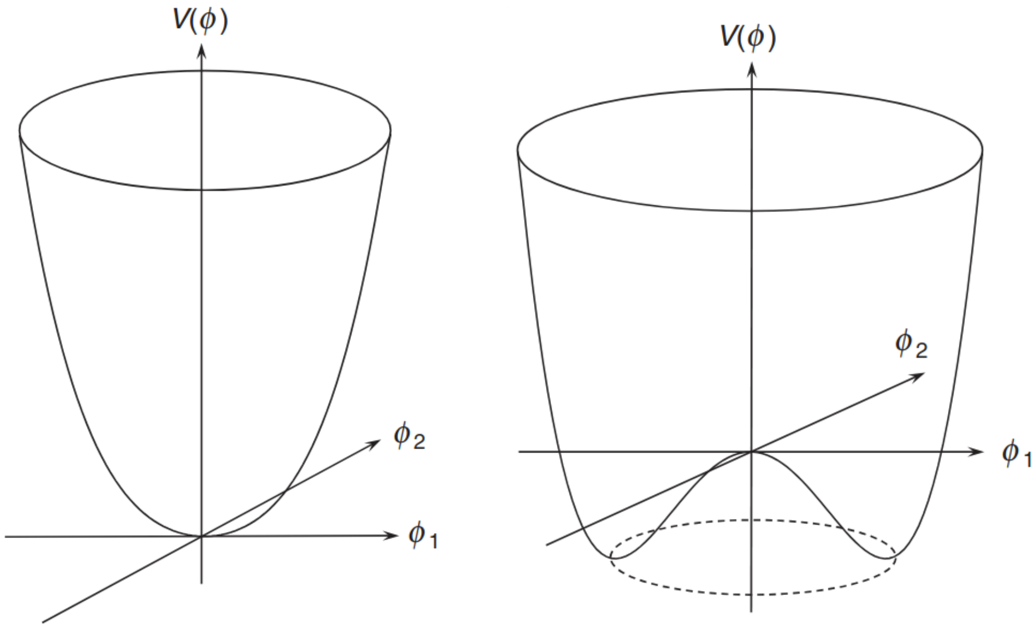

Abbildung 2.2: The unbroken (left) and broken (right) Higgs potentials for a complex scalar field. [32]

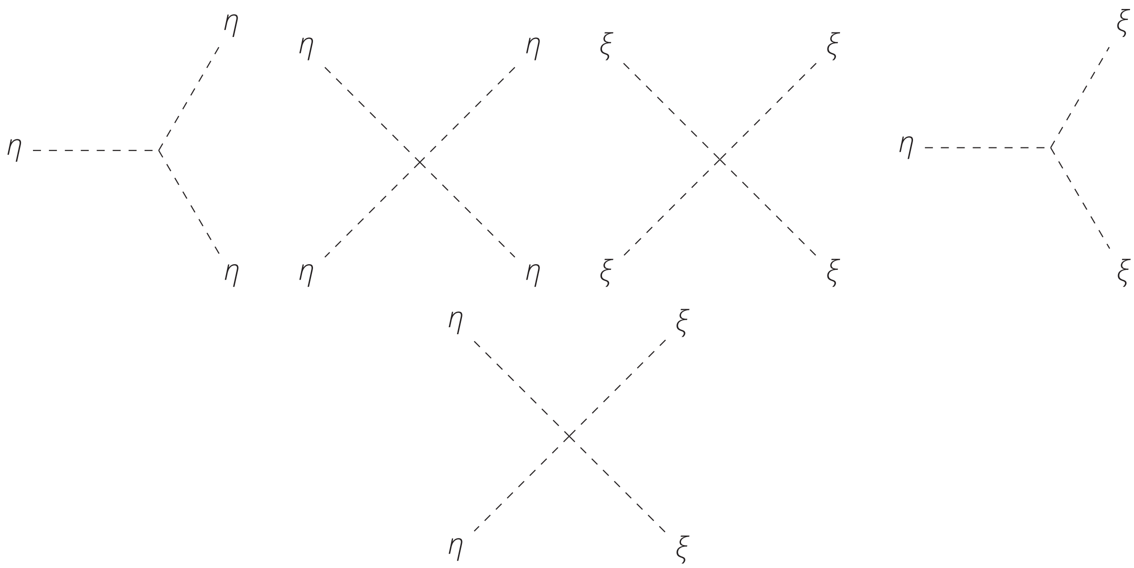

Abbildung 2.3: All triple and quartic interaction vertices between the excitation fields η and ξ.

The ξ-particle represents the excitations not in the direction of the real axis but perpendicular to it, where the potential does not change. This represents a massless Goldstone boson. The next step is to implement the $\mathrm{U}(1)$ local gauge symmetry into the complex scalar field, which can be reached by the introduction of a covariant derivative.

$$\partial_\mu \rightarrow \mathrm{D}_\mu = \partial_\mu + \mathrm{igB}_\mu \tag{2.20}$$

with B_μ being massless gauge field. While again using the perturbation approach for the excitation of a complex scalar field from 2.17, it's also necessary to adapt the covariant derivative. After all this, the Lagrangian expands to the following expression

$$\mathcal{L} = \frac{1}{2}(\partial_\mu \eta)(\partial^\mu \eta) - \lambda v^2 \eta^2 + \frac{1}{2}(\partial_\mu \xi)(\partial^\mu \xi) - \frac{1}{4}\mathrm{F}_{\mu\nu}\mathrm{F}^{\mu\nu} + \frac{1}{2}\mathrm{g}^2\mathrm{v}^2\mathrm{B}_\mu\mathrm{B}^\mu + \mathrm{gvB}_\mu(\partial^\mu \xi) - \mathrm{V}_{\mathrm{int}} \tag{2.21}$$

Now, the existence of the Goldstone boson within the Lagrangian has physical implications, that might seem odd at first glance, since overall it's the same Lagrangian as in 2.11 still handled here. For example, it seems like, when the $\mathrm{U}(1)$-symmetry is implemented, that the corresponding gauge field B_μ gains mass through breaking the $\mathrm{U}(1)$-symmetry. This would be a problem, because in the original Lagrangian there were only 4 degrees of freedom (the fields φ_1, φ_2 and the transverse polarization states of B_μ). Now that the field B_μ is massive, it gets an additional longitudinal polarization state, which is one more than initially existed. Also, because of the $\mathrm{gvB}_\mu(\partial^\mu \xi)$-term, it seems the gauge-field can transform into the Goldstone boson, which would not conserve spin. This issues can be taken care of in an elegant manner. By the use of the transformation

$$\mathrm{B}_\mu \rightarrow \mathrm{B}'_\mu = \mathrm{B}_\mu + \frac{1}{\mathrm{gv}}(\partial_\mu \xi), \tag{2.22}$$

it is possible to „gauge out“the unphysical $\mathrm{gvB}_\mu(\partial^\mu \xi)$-term. After that step, the Goldstone boson is also eliminated from the Lagrangian and its degree of freedom has been taken by the longitudinal polarization state of the now massive B_μ-field.

With all this previous steps it is possible to formulate the Standard Model Higgs mechanism, which means that now the theory has to be extended to fit the $\mathrm{SU}(2) \times \mathrm{U}(1)$-symmetry. Therefore the Higgs field is chosen to form a weak isospin doublet, consisting of 2 complex scalar fields where the upper component is charged and the lower one is neutral.

$$\varphi = \begin{pmatrix} \varphi^+ \\ \varphi^0 \end{pmatrix} = \frac{1}{\sqrt{2}} \begin{pmatrix} \varphi_1 + \mathrm{i}\varphi_2 \\ \varphi_3 + \mathrm{i}\varphi_4 \end{pmatrix} \tag{2.23}$$

This approach has the convenient property, that it provides enough degrees of freedom to cover the demanded longitudinal polarization states for all the massive gauge bosons in the theory, the $\mathrm{W}^\pm$ and Z. Also it predicts at least one additional massive scalar field. As for the aforementioned cases, the following description of the field will be handled as an excitation around the minimum of the Higgs-potential, thus moving the φ into the form,

$$\varphi(\mathrm{x}) = \frac{1}{\sqrt{2}} \begin{pmatrix} \varphi_1(\mathrm{x}) + \mathrm{i}\varphi_2(\mathrm{x}) \\ \mathrm{v} + \eta(\mathrm{x}) + \mathrm{i}\varphi_4(\mathrm{x}) \end{pmatrix} \tag{2.24}$$

on which the unitary gauge is applied on, leading to:

$$\Phi(\mathrm{x}) = \frac{1}{\sqrt{2}} \begin{pmatrix} 0 \\ \mathrm{v} + \mathrm{h}(\mathrm{x}) \end{pmatrix} \tag{2.25}$$

To acquire the mass terms for the gauge bosons and also the interaction terms, the covariant derivative for this $\mathrm{SU}(2) \times \mathrm{U}(1)$-symmetry is introduced.

$$\partial_\mu \rightarrow \mathrm{D}_\mu = \partial_\mu + \mathrm{i}\mathrm{g}_\mathrm{W}\mathbf{T}\cdot\mathbf{W}_\mu + \mathrm{i}\mathrm{g}'\frac{\mathrm{Y}}{2}\mathrm{B}_\mu, \tag{2.26}$$

where T are the Generators of the $\mathrm{SU}(2)$ as already shown in 2.2. To be able to interact with the Higgs-doublet, the terms ∂_μ and $\mathrm{i}\mathrm{g}'\frac{\mathrm{Y}}{2}\mathrm{B}_\mu$ are assumed to be arranged on the main-diagonal of a 2×2-matrix. Now the covariant derivative acts on the Higgs weak isospin double in the following way

$$\mathrm{D}_\mu\varphi = \frac{1}{2\sqrt{2}}\begin{pmatrix} \mathrm{i}\mathrm{g}_\mathrm{W}(\mathrm{W}_\mu^{(1)} - \mathrm{i}\mathrm{W}_\mu^{(2)})(\mathrm{v}+\mathrm{h}) \\ (2\partial_\mu - \mathrm{i}\mathrm{g}_\mathrm{W}\mathrm{W}_\mu^{(3)} + \mathrm{i}\mathrm{g}'\mathrm{B}_\mu)(\mathrm{v}+\mathrm{h}) \end{pmatrix}. \tag{2.27}$$

So when taking the hermitian conjugate of $\mathrm{D}_\mu\varphi$ and multiplying it with itself, $(\mathrm{D}_\mu\varphi)^\dagger(\mathrm{D}^\mu\varphi)$ results in

$$\begin{aligned}(\mathrm{D}_\mu\varphi)^\dagger(\mathrm{D}^\mu\varphi) =& \frac{1}{2}(\partial_\mu\mathrm{h})(\partial^\mu\mathrm{h}) + \frac{1}{8}\mathrm{g}_\mathrm{W}^2(\mathrm{W}_\mu^{(1)} + \mathrm{i}\mathrm{W}_\mu^{(2)})(\mathrm{W}^{(1)\mu} - \mathrm{i}\mathrm{W}^{(2)\mu})(\mathrm{v}+\mathrm{h})^2 \\ &+\frac{1}{8}(\mathrm{g}_\mathrm{W}\mathrm{W}_\mu^{(3)} - \mathrm{g}'\mathrm{B}_\mu)(\mathrm{g}_\mathrm{W}\mathrm{W}^{(3)\mu} - \mathrm{g}'\mathrm{B}^\mu)(\mathrm{v}+\mathrm{h})^2\end{aligned} \tag{2.28}$$

The mass terms now appear as the quadratic terms of the gauge bosons in (2.28), being $\frac{1}{2}\mathrm{m}_\mathrm{W}^2\mathrm{W}_\mu^{(1)}\mathrm{W}^{(1)\mu}$ and $\frac{1}{2}\mathrm{m}_\mathrm{W}^2\mathrm{W}_\mu^{(2)}\mathrm{W}^{(2)\mu}$, which implies the W-boson mass of $\mathrm{m}_\mathrm{W} = \frac{1}{2}\mathrm{g}_\mathrm{W}\mathrm{v}$.
The interaction terms of the gauge fields with the Higgs field, and for this work the interaction with the W-fields is of most interest, derive from the second term on the right side of equation (2.28). Through the definition of the physical W-fields in (2.5), it is easy to see the vertices that go into the interaction with the Higgs field. For $\frac{1}{4}\mathrm{g}_\mathrm{W}^2\mathrm{W}_\mu^+\mathrm{W}^{\mu-}(\mathrm{v}^2 + 2\mathrm{v}\mathrm{h} + \mathrm{h}^2)$, the first term yields the mass term of W^+ and W^-, the second one a triple vertex of two W-bosons to the Higgs-boson and the last one suggests a quartic coupling between Higgs- and W-bosons, which is of great interest in this thesis.

2.3 Vector-Boson-Scattering (VBS)

As mentioned in chapter 2.1, it is an interesting ability of the gauge fields of the weak interaction to be able to interact with each another or with themselves, allowing triple or even quartic vertices between them. This is, as mentioned above, resulting from the non-abelian nature of the generators of the $\mathrm{SU}(2)$-symmetry group. VBS describes all scattering processes, that involve two electroweak gauge bosons in the initial state and can be directly connected to other electroweak bosons in the final state. For the fulfillment of this definition it does not necessarily have to be the same type of electroweak gauge boson, so any process denoted as $\mathrm{VV}\rightarrow\mathrm{VV}$ does qualify as such [33]. The most common shapes of vertices in VBS are shown in figure 2.4.

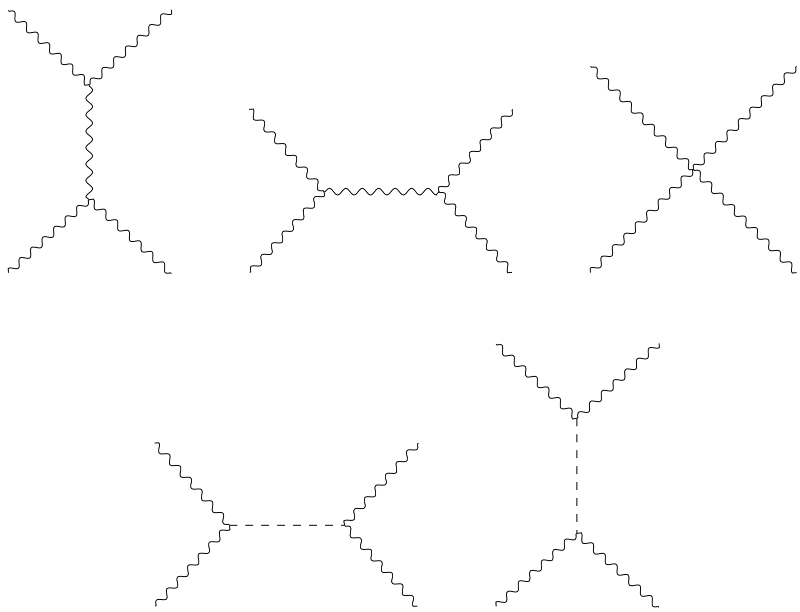

Abbildung 2.4: Most common Feynman diagrams at leading order concerning vector boson scattering, including s- and t-channel diagrams with intermediate γ, Z or H or the quartic W-boson vertex.

These shapes apply for opposite charged W-bosons in the initial state but also for same-sign ones. The latter variant will be of more interest in this work.

It is important to take all of these different diagrams in consideration when investigating on a final state where all of them could possibly contribute to. To ignore certain diagrams would cause the cross-section of the investigated process to diverge for higher center-of-mass energies, leading to probabilities larger than one, which would be physically not interpretable. By including all diagrams, they are able to interfere, thereby preventing a violation of unitarity and granting gauge invariance. Historically spoken, this was one reason why the existence of the Higgs-boson was considered. When investigating on the $\mathrm{W}^+\mathrm{W}^- \rightarrow \mathrm{W}^+\mathrm{W}^-$-process it became apparent, that the longitudinal polarization mode $\mathrm{W_L W_L} \rightarrow \mathrm{W_L W_L}$ would break unitarity for higher center-of-mass energies. The violation of unitarity only being connected to the longitudinal polarization mode of the gauge bosons can be explained with the Goldstone equivalence theorem [11], where for high regions of energy the longitudinal mode of the gauge bosons starts acting again like an independent particle (the Goldstone boson). The cross-section of the process $\mathrm{W_L W_L} \rightarrow \mathrm{W_L W_L}$, if only connected through triple couplings of the electroweak interaction, diverges for large center-of-mass energies. With the introduction of the quartic $\mathrm{W}^\pm$ coupling, this effect could be weakened, since both types of Feynman-diagrams diverge by a ratio of $\propto \mathrm{E}^4$, but since they diverge with different signs, both contributions cancel, leaving only a term proportional to E^2. For the cancellation of this term and thereby the conservation of unitarity, it was necessary to introduce an additional scalar particle, the Higgs boson.

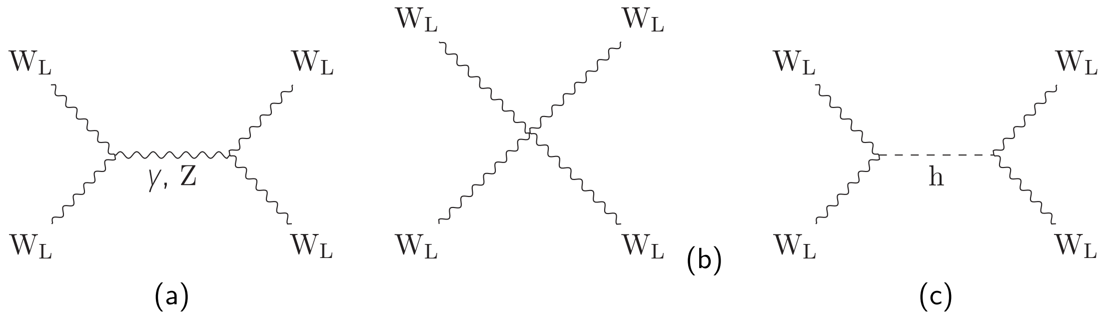

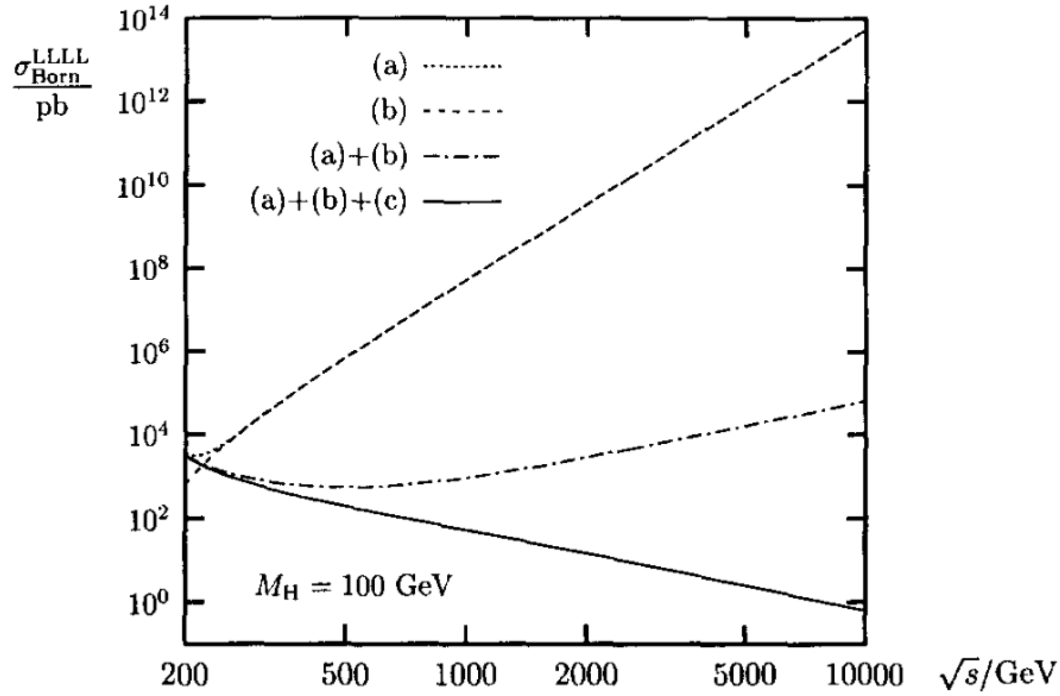

Abbildung 2.5: Cross-sections behavior in $\mathrm{W_L W_L}$-scattering including different sets of VBS vertices.[17]

2.4 The Signal Process $\mathrm{jj} \rightarrow \mathrm{W}^{\pm}\mathrm{W}^{\pm}\mathrm{hjj}$

For the analysis in this thesis the so called κ-**framework** is being used. The feature of the κ-framework is, that it combines the Standard Model coupling for one specific typ of Higgs coupling (e.g. $\lambda_{\mathrm{VVh}}^{(\mathrm{SM})}$,$\lambda_{\mathrm{hhh}}^{(\mathrm{SM})}$,$\lambda_{\mathrm{VVhh}}^{(\mathrm{SM})}$, ...) and one arbitrarily chosen factor for the coupling by the analyzer, within one parameter and thereby makes both of them comparable to each another. This way, the coupling modifier $\kappa_{\mathrm{i}} = \frac{\lambda_{\mathrm{i}}}{\lambda_{\mathrm{i}}^{(\mathrm{SM})}}$ describes the ratio of the newly chosen coupling to the SM one, where $\kappa_{\mathrm{i}} = 1$ refers to the SM case and any deviation from it to a beyond SM case.

There are different motivations for the investigation of the couplings of the Higgs boson, be it the coupling to itself or to the gauge bosons. For example, the Higgs self coupling vertices hhh and hhhh yield crucial information on the behavior of the Higgs potential around its minimum, since they are connected to the λ-parameter from the lagrangian of the Higgs formalism 2.11. In practical analyses, mostly the triple higgs coupling is of interest, because the quartic self coupling is, considering the center-of-mass energies the LHC is able to produce at the time, out of reach [24]. Hence an interest in the studies of the coupling modifier κ_{hhh}, often also denoted as κ_{λ}, is apparent. For the studies concerning $\kappa_{2\mathrm{V}}$ the same motivation does not apply, since the coupling, as could be concluded off of 2.28, does not have any connection to the λ-parameter and therefore has no influence on the shape of the Higgs potential. The study of the $\kappa_{2\mathrm{V}}$ gauge-Higgs coupling is essential to test the gauge cancellation between the VVh and VVhh couplings that is predicted in the Standard Model. If gauge cancellation was not provided with the experimentally acquired values for the gauge-Higgs couplings, unitarity would be violated. Another way to formulate that the contributions of $\kappa_{2\mathrm{V}}$ and κ_{V} have to fully cancel each other, is the expression $\kappa_{2\mathrm{V}} = (\kappa_{\mathrm{V}})^2$, since it implies that there are no further interactions at work in the quartic gauge-Higgs vertex. It is important to mention, that all vector bosons contribute to the $\kappa_{2\mathrm{V}}$-parameter, but the $\mathrm{W}^{\pm}$-bosons are more influential, since through them being charged, they can interact in more distinguishable ways than the Z-boson. Therefore, for this analysis, the expressions $\kappa_{2\mathrm{V}}$and κ_{WW} will be used synonymously.

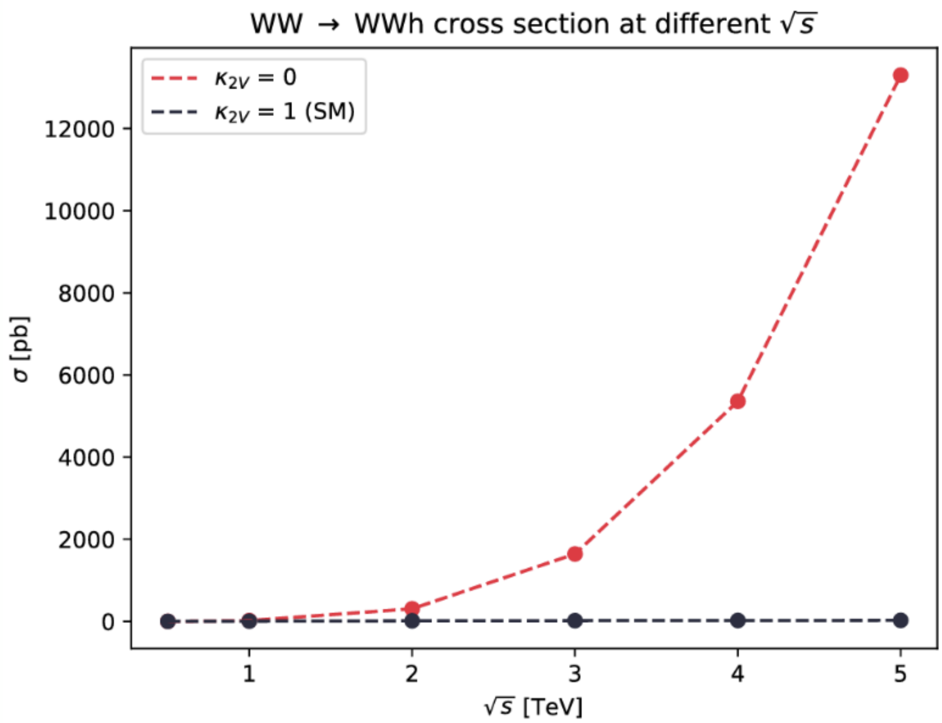

Abbildung 2.6: Theory prediction of the $\mathrm{W^\pm W^\pm} \rightarrow \mathrm{W^\pm W^\pm h}$ cross-section. The red graph shows the divergence of the cross-section for increasing $\sqrt{\mathrm{s}}$ when the influence of the $\kappa_{2\mathrm{V}}$ coupling is set to 0. The black curve represents the well behaved cross-section with the $\kappa_{2\mathrm{V}}$-contribution as it is predicted in the Standard Model. [13]

The process chosen for investigation in this thesis is the $\mathrm{jj} \rightarrow \mathrm{W^\pm W^\pm hjj}$ process, specifically because of its share of Feynman diagrams sensitive to the $\kappa_{2\mathrm{V}}$ gauge-Higgs coupling modifier. A general depiction is shown in 2.7b. It is necessary to emphasize, that this is not the only way to reach this final state. For example the same final state can be acquired with both radiated $\mathrm{W^\pm}$-bosons radiating a h-boson each, which together form a triple self coupling vertex. This means, the process $\mathrm{jj} \rightarrow \mathrm{W^\pm W^\pm hjj}$ is not just sensitive to variations of $\kappa_{2\mathrm{V}}$ but also to changes of κ_λ. Therefore it is important to consider all possible diagrams, which can lead to the final state in question. Although the proton consists of up and down quarks, through the permanent presence of gluons it is possible that spontaneously other quark-types form and annihilate, which are also able to take part in the interaction and therefore need to be treated. This effect is accounted for in the Monte Carlo simulations by applying a so called flavor scheme on the PDF of the initial protons. If a 4-flavor scheme is being used, the quarks of the first 2 generations are assumed to be non-massive, in the 5-flavor scheme the b-quark is also treated as massless. In the specific case of $\mathrm{jj} \rightarrow \mathrm{W^\pm W^\pm hjj}$, both schemes lead to almost similar results, as it has been shown in [23].

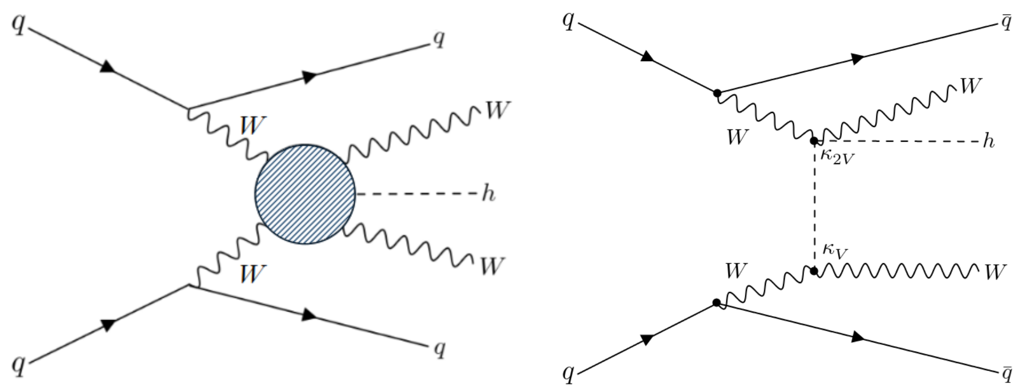

(a) (b)

Abbildung 2.7: a) shows the signal process $\mathrm{jj} \to \mathrm{W}^{\pm}\mathrm{W}^{\pm}\mathrm{hjj}$ process. b) Represents the signal diagram involving κ_{V} and $\kappa_{2\mathrm{V}}$ couplings within the $\mathrm{jj} \to \mathrm{W}^{\pm}\mathrm{W}^{\pm}\mathrm{hjj}$ process. The h-boson is set to decay into a $\mathrm{b\bar{b}}$ quark pair and the $\mathrm{W}^{\pm}$-bosons decay leptonically, into $\mathrm{e}^{\pm}$ or $\mu^{\pm}$ and their corresponding neutrinos. Schematically, in the collision both protons radiate a $\mathrm{W}^{\pm}$-boson of the same charge. One is connected to a quartic gauge-Higgs vertex, where one $\mathrm{W}^{\pm}$ and one h further decay, while the second h connects both of the initially radiated $\mathrm{W}^{\pm}$ as a virtual h.

Even though this thesis is based on a truth level analysis, some interesting properties that would come into play more prominently for real experimental data shall still be mentioned:

VBS-topology What makes the $\mathrm{jj} \to \mathrm{W}^{\pm}\mathrm{W}^{\pm}\mathrm{hjj}$ process favorable to analyze is its clear signature in the event data. As a VBS process it is characterized by a high center-of-mass energy of the light jets $\mathrm{m_{jj}}$ and a large angle between both jets, leading to a high $\Delta\eta$. This is, because the incoming beams are of such high energy, that they are not easily deflected from their original trajectory.

Same-sign $\mathrm{W}^{\pm}\mathrm{W}^{\pm}$ Scattering One favorable property of $\mathrm{W}^{\pm}\mathrm{W}^{\pm}$ same-sign scattering is that it is well recognizable. Firstly, it is clearly distinguishable from other electroweak decay channels, since it always leaves two same-charged leptons and two neutrinos, that have to be reconstructed via the missing transverse energy. The decay channels for other vector boson configurations are more likely to be similar to others. For example, the leptonic decay of two opposite sign W-bosons can also be mimicked by two Z bosons in the final state. It is also favorable considering the influence of QCD background, since it is not possible to emit two same-charge W-bosons of the same quark line. It is also necessary to mention, that positively and negatively charged W-bosons do not contribute at equal parts. The W^{+}-bosons contribute more prominently, due to the fact that there are more up-quarks present in the proton, than there are down-quarks. A more detailed analysis on this topic is given in Ref. [25].

VBS over Vector-Boson-Fusion Vector-Boson-Fusion (VBF) is a different production channel than VBS. It is often used in Di-Higgs-production [14] and it sets itself apart from VBS by having the initial vector-bosons annihilated in the interaction, so that they can not be found in the final state. This yields the VBF-process shown in figure 2.9.

In terms of simply measuring the true value of $\kappa_{2\mathrm{V}}$, this process is of better use, since it has a way higher cross-section than the signal process ($\sigma_{\mathrm{VBF}} = 1.73\,\mathrm{fb}$ [14] and $\sigma_{\mathrm{VBS}} = 0.018\,\mathrm{fb}$ [13]). However, the information on how the different vector bosons contributed is lost. For a more subtile understanding of every contribution from all vector bosons to the $\kappa_{2\mathrm{V}}$-parameter,

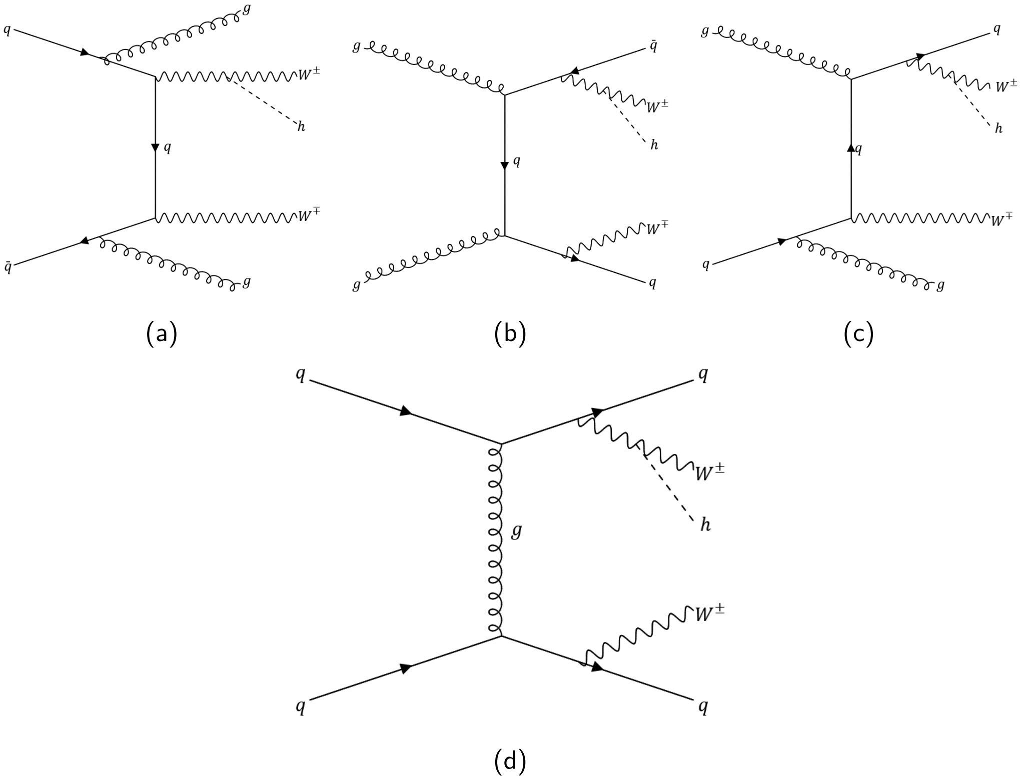

Abbildung 2.8: Feynman diagrams of QCD processes. The diagrams in a), b) and c) show different ways the W-bosons are emitted by the same quark line and therefore can not be of the same charge. The diagram in d) shows an example for an emission from two separated quark lines which enables two W-bosons of the same charge in the final state.

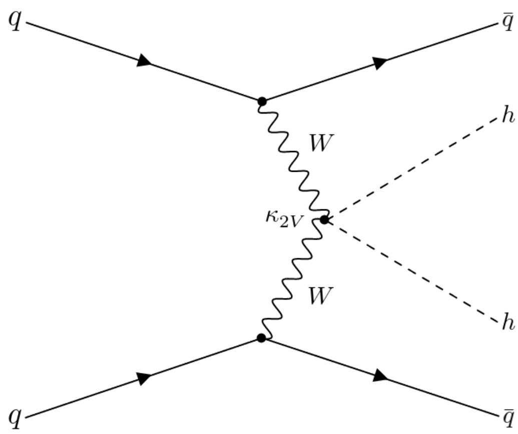

Abbildung 2.9: VBF-process for di-Higgs production, also containing the gauge-Higgs quartic coupling vertex.

the VBS-process is more valuable, since the vector bosons that took part in the scattering still exist in the final state.

2.5 Histograms and Event Weights

In this thesis, the most prominent way of data presentation will be through the creation of histograms, so this shall be a short introduction on the topic, including a short insight on event weights.
The bins of a histogram can either be equidistant, so the interval of $\mathrm{O_{min}}$ to $\mathrm{O_{max}}$ will be divided into N equal spacings, with each bin i having a width of $\frac{\mathrm{O_{max}-O_{min}}}{\mathrm{N}}$, or the bin boundaries can be chosen completely arbitrarily. Because of the latter case, for all the histograms in this thesis, each bin will be divided by its bin width. That way, the differential distribution of the observables behaves more like a probability distribution function. Note that this procedure influences the unit corresponding to the y-axis of the histogram by a factor of one over the unit the bin interval is separated by. To fill the histogram, the value of the observable O is measured for each event and the bins corresponding to the interval the measured value falls into will be raised by one quantity. In this specific case, the height of each bin would directly correspond to the actual number of events that lie within this area of values of O. These events would then be referred to as *unweighted*, since, in the creation of the samples, no additional factor has been applied to compensate for the different probabilities of the occurrence of some of the events. If there was such a factor involved, the resulting samples would be referred to as *weighted* and the associated factor for each event number n would be called a weight $\mathrm{w_i}$. The motivation for the usage of weighted events becomes apparent for the studies of rare processes. In real detector samples or unweighted event data, there is no guaranty that certain rare processes are included in the results. For weighted event generation, all possible events are drawn from an even distribution and afterwards, when filling the histogram, a weight factor is applied, hence in this case the bin height doesn't increase by a unit of one for each additional event, but by the value of the weight factor. If the histograms can be normalized to a certain value, be it e.g. one or the total cross-section σ_{tot} of the process. To do this in a general manner, which does work for any type of event, it is necessary to calculate the sum of weights W:

$$\mathrm{W} = \sum_{\mathrm{i}} \left(\sum_{\mathrm{j=1}}^{\mathrm{n_i}} \mathrm{w(j)} \right)_{\mathrm{i}} \tag{2.29}$$

where i is the bin number, $\mathrm{n_i}$ is the number of events in the ith bin and $\mathrm{w(j)}$ is the weight of the event number j. For the special case of unweighted events, the weight $\mathrm{w(j)} = 1$ and therefore, if summed together, is only the total number of all events. Usually, in event simulation, it is general practice to normalize to the sum of weights or especially the total number of events, since, in comparison to actual data from a collider experiment, the total number of events bares no additional information, since events can be generated almost arbitrarily. To normalize to the cross-section, each bin must be afterwards multiplied with the differential cross-section $\frac{\mathrm{d}\sigma_{\mathrm{i}}}{\mathrm{dO_i}}$ of the corresponding bin representing the interval in the phase space of O. The production of Monte Carlo samples with event generators can strongly vary in terms of time to generate a certain amount of events. Especially when samples are drawn from a really exotic phase space region, the time to produce a certain amount of unweighted events can be orders of magnitudes higher than the time it would take to produce the same number of weighted events. That being said, unweighted events have way more statistical meaningfulness related to event count than weighted ones, which can be correlated to the way their errors scale. This becomes apparent when looking into respective bins containing different magnitudes of numbers of events. For unweighted events the error is large for a small event count and shrinks with increasing number of events, because the error scales, as in poisson distributions, like $\propto \frac{1}{\sqrt{\mathrm{N}}}$. This is different for the behavior of errors in weighted events, where a fixed relative error is being added on top of each other, which prevents the error to converge towards zero for large numbers of events.

3 Experimental Setup

The Analysis in this thesis mimics the Run 2 Data from the LHC at $\sqrt{\mathrm{s}} = 13\,\mathrm{TeV}$. Even though it will be performed at truth-level, there shall still be a drawn a connection to the real experimental setup at the LHC and further the ATLAS detector. In the second part of this chapter there will be an outline on the matrix element generation and Monte Carlo integration methods that are went through before the event generation. Afterwards a step by step description of all the processes necessary to model Monte Carlo samples, including the modeling of the hard process, the parton showering or the hadronization, follow.

3.1 The Large Hadron Collider

The CERN organization has been founded in the year 1954 [9], with 12 European countries contributing to the project initially (today up to 25 states). The first particle accelerators were build by the end of the 1950s, namely a synchrotron in 1957 and a proton synchrotron in 1959. In the following decades CERN was able to reach several milestones, like the recording of the first proton-proton collision in 1971 or the discovery of the weak gauge bosons in 1983. After 4 years of technical proposal and planning the general-purpose experiments ATLAS and CMS were approved in 1993, which are opting for research in fundamental physics, with topics as the Standard Model interactions, super symmetry or the search for the Higgs boson. Finally in 2008 the Large Hadron Collider (LHC) has its first successful run, starting a new era for the research in high energy particle physics.

The LHC can be considered one of the most complex machines to be build by mankind. It is designed to perform proton-proton collisions or to collide lead-ions at high center of mass energies. That way it is possible to probe or validate theoretical extensions of the Standard Model and thereby extend our understanding of particle physics. The LHC is about 27 kilometers long and lies 50 to 175 meters deep in the ground. It has 4 spots that are designated for collisions, which are the points where the detectors of the contributing experiments are positioned, e.g. the detectors of ATLAS, CMS, ALICE, TOTEM and LHCb. The tunnel of the LHC is equipped with a structure of superconducting magnets that keeps the accelerated particles on track. They use radio frequency (RF) cavities, which generate an electric field parallel to the proton bunches trajectories at the exact moment one of them passes. Through there well time-coordinated activation the proton bunches are being accelerated [10]. For the experiments, bunches of hadrons are being accelerated in clockwise direction and anti-clockwise direction. In the case of a proton-proton experiment, the bunches can consist of up to 115 billion protons each. At the point of the planned collisions, the proton beams are redirected to a way narrower volume by an additional set of magnets, to provoke a higher number of collisions (This volume has the dimensions of a diameter of $16\mu\mathrm{m}$ and a length of $8\mathrm{cm}$).This way the luminosity L, a value for how many particles actually meet each other within a square-centimeter within in the collider, is established. L depends on the number of particles in a bunch, the collision

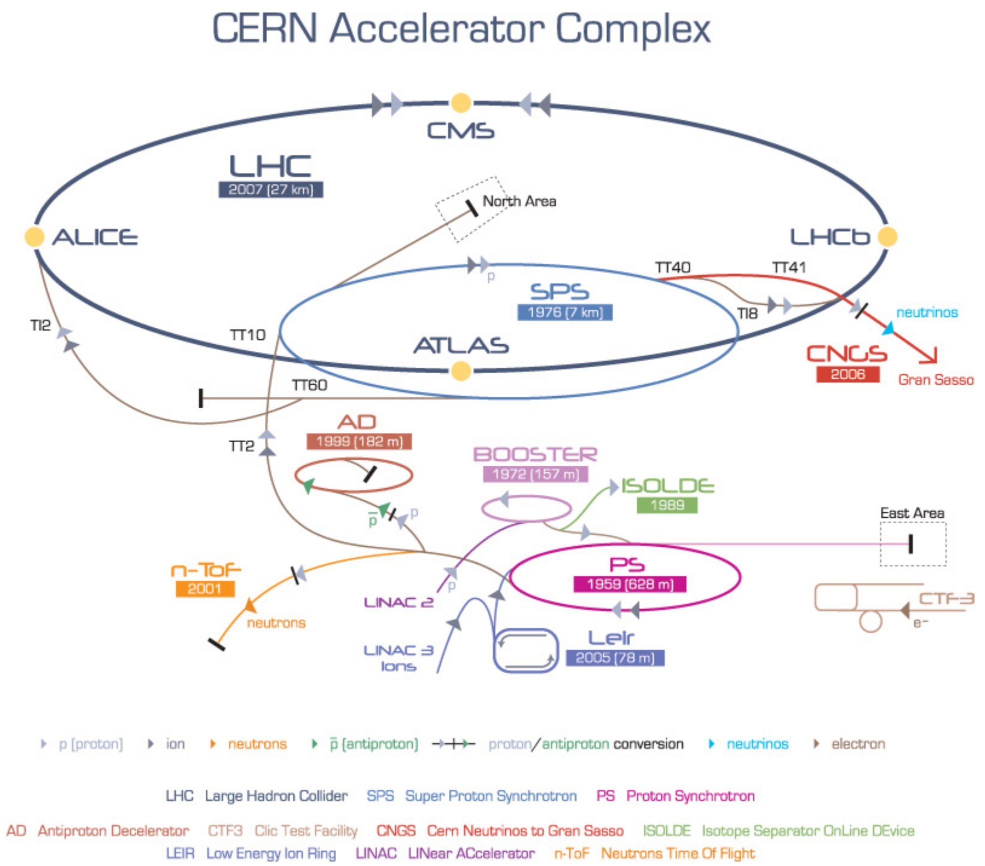

Abbildung 3.1: Overview on the complete LHC complex and its facilities at the time when the ATLAS experiment was taking data for Run 2 [27].

frequency and the inverse of the beam's width. When the integral of L over time gets multiplied with the cross-section σ, which represents the likelihood of two bunch particles that meet each other to actually interact, the result is the absolute number of interactions in the collider. The LHC is able to generate a luminosity of $\mathrm{L} = 10 \times 10^{34}\mathrm{cm}^{-2}\mathrm{s}^{-1}$ and a center-of-mass energy of $\sqrt{\mathrm{s}} = 14\mathrm{TeV}$.

3.2 The ATLAS Detector

The ALTAS-detector [16] was designed and constructed by the ATLAS collaboration. It is a general purpose detector, designed to catch and distinguish the resulting particles of any major type from high energy collisions in the LHC. It has a cylindrical shape, with a length of 46 meters and a height of 25 meters [8], and is constructed symmetrical in forward/backward direction, considering the interaction point. Going from the most inner layer outwards, closest to the beam axis lies an inner detector, which records the track of charged particles and transverse momenta, then there are electromagnetic and hadronic calorimeters and the furthest outside lies the muon spectrometer .

The inner detector has a core of a central solenoid, that can create a magnetic field with a strength of up to 2 T. It is surrounded by precision tracking devices, so called pixel and silicon microstrip (SCT) trackers closer to the beam and Transition radiation trackers (TRT) on the outer side. They are spatially arranged in 2 regions, for one part as concentric cylinders around the beam axis, the barrel region, and for the others as disks perpendicular to the beam axis, the end-cap region, allowing to cover an area of $|\eta| < 2.5.$. The pixel detector has the highest granularity, with its pixels being subdivided in $\mathrm{R} - \Phi$ and z, with a minimum pixel size of $50 \times 400\mu\mathrm{m}^2$. It has around 80.4 channels in all its layer combined that are readout. The following layer is the SCT, which consists of discrete microstrips running parallel to the beam axis. They form four layers arranged in a circle around the beam, thereby allowing to gain information of the $\mathrm{R}-\Phi$ and z coordinates at a time. It has, compared to the pixel detector, only 6.3 million readout channels. The remaining most outer part of the inner detector is the TRT, which is made up of tungsten straw tubes, filled with xenon-gas, which are running parallel to the beam axis. It only provides information on the $\mathrm{R} - \Phi$ coordinates with $130\mu\mathrm{m}$ of accuracy per straw. In the barrel region they are parallel to the beam axis and in the cap-end region they are placed like circles. The TRT is approximately read out for 351000 channels.
Outside of the inner detector are the electromagnetic (EM) and hadronic calorimeters. They cover a region of $|\eta| < 4.9$ and can apply different methods of measurement at different locations of the detector, depending on the investigated process. For example, there is a finer granularity in the area covered by the inner detector, that shall allow a more precise measurement of electrons and photons. Also the thickness of the detector is crucial, to avoid punch through of irreducible muons in the EM calorimeter and to allow to resolve the jet-energies as accurately as possible in the hadronic calorimeter. The EM calorimeter also consists of a barrel region and an end-cap region. The barrel region is formed by two identical half-barrels with a slim gap of $4\mathrm{mm}$ between them and the end-cap region consist of an inner and outer wheel, covering different areas of η. In total, the EM calorimeter is a lead-LAr (liquid Argon) detector with accordion-shaped kapton electrodes and it is completely covered in lead absorber plates.
The EM calorimeter is completely surrounded by the hadronic calorimeter, which consists of the Tile calorimeter, the LAr hadronic end-cap calorimeter and the LAr forward calorimeter. The tile calorimeter is closest to the EM calorimeter and is found in the barrel region. It is a sampling calorimeter with steel as an absorber material and it has scintillating tiles as active material. The hadronic end-cap calorimeter is made up of to separate wheels on each end-cap and it is also close to the EM calorimeter in this region. The wheels are each assembled by 32 identical copper modules, and consists of two units. A slimmer one with a thickness of $25\mathrm{mm}$, closer to the interaction point, and a thicker one further away with a thickness of $50\mathrm{mm}$. The gaps in between the single copper plates are filled with liquid Argon to provide an active medium for the sampling calorimeter. The last part, the LAr forward calorimeter, which consists of 3 distinguished modules, one that is specialized in electromagnetic measurements and which is made out of copper, and two other ones

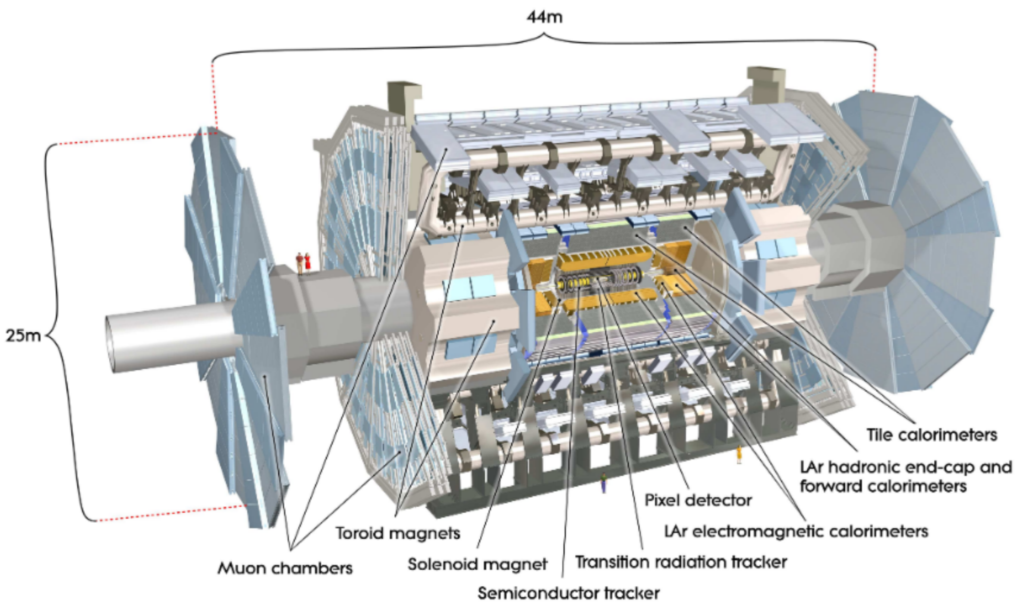

Abbildung 3.2: An overview on the ATLAS-detector, showing all the inner components like inner detector, electromagnetic and hadronic calorimeters and muon spectrometer in context. [16]

for the measurement of the hadronic interaction energy, that are made out of tungsten. The electro-sensitive structures are installed within longitudinal channels , being concentric rods and tubes, which are regularly spaced in metal matrices. The gaps between the inner tubes are filled with LAR, which is the sensitive medium.
The muon spectrometer consists of a large barrel toroid with smaller end-cap magnets at each of its ends. Its goal is the distraction of the muon trajectories through the magnetic toroid, where they can be measured with high precision and separate triggers. The tracks are measured in three cylindrical layers, positioned around the beam axis, thereby covering the barrel region, where as in the transition and end-cap region, there are three plane chambers, placed perpendicular to the beam direction.

3.3 Event Generation with Monte Carlo Generators

Monte Carlo Event Generators are a crucial tool for research in high energy particle physics. They are useful to predict experimental results and therefore demand a deep understanding for the processes of interest to create a realistic simulation. They even allow to implement theoretical models beyond the Standard Model and how the resulting interactions would influence experimental measurements. In this section, there will be an overview on the general steps a Monte Carlo event generator advances through in order to generate Monte Carlo samples. To write this section, the sources [28], [29] and [31] have been used.

Preparation and matrix element calculation: For the generation of an event, one phase space point will be picked at random, that will represent the four-vectors of the initial (and final) state particles. Often those phase space points are not sampled from an even, but a further refined distribution, that concentrates more approximated for of the integrand. This method is called *importance sampling*, while the first one is called *uniform sampling*. After a phase space point is picked, the next step is to integrate over the matrix element over the restricted phase space area. The integration involving every step for the construction of a complete event gets quickly convoluted since every modeling instance can add multiple dimensions to the integral, hence an analytical treatment of the calculation is not possible. That is why phase space integrals in Monte Carlo event generation are calculated by numerical methods, more specifically, Monte Carlo integration [22]. In general, the Monte Carlo integration is described by the average value of a function $g(x)$ within the phase space times the volume of the phase space. In the one-dimensional case this can be formulated like

$$\int_a^b g(x)dx = \langle g(x) \rangle \cdot (b-a) \approx \frac{(b-a)}{N} \sum_{i=1}^{N} g(x_i). \tag{3.1}$$

The error that comes with Monte Carlo integration is proportional to $\frac{1}{\sqrt{N}}$, which implies, that with increasing number of events N, the value of the integral converges towards the analytical integration value. One simple example for a Monte Carlo integration method is the „Hit-or-Miss-Method", in which the goal is to implement a function $f(x)$ that, as minimally as possible, overestimates the actual distribution of particle states $g(x)$ in the phase space. Now a random point within the confines of $f(x)$ is being drawn, that will be rejected if it is not also included in $g(x)$. So mathematically, if $\frac{f(x)}{g(x)} < R$, where R is the random point, the point is dismissed.

When a phase space point has been chosen, the next step is to calculate the matrix element. This is a non-trivial task, because while the calculation for $2 \to 2$ or $2 \to 3$ processes can theoretically be done via pen and paper, the number of Feynman diagrams necessary to include grows at a factorial rate. There are different way to do matrix element calculations. In the matrix element generators Madgraph or Amegic, helicity amplitudes are used for the calculation, but in the case of Comix (which is going to be used in the Sherpa event generations) the Berends-Giele method is being used. More on that can be found in Ref. [21].

Monte Carlo event simulation: With all this preparation, it is finally possible to generate an event. In general, the following steps are contained within the modeling process:

1. Hard Process
2. Parton Shower
3. Hadronization
4. Underlying event
5. Unstable Hadron Decay
6. QED Radiation

The **hard process** is the interaction of highest momentum transfer and in Monte Carlo simulations this corresponds to the main process of interest. The hadronic cross-section with N particles in the final state can be calculated like

$$\sigma_N = \sum_{a,b} \int dx_1 dx_2 \, f_a \left(x_1, \mu^2\right) f_b \left(x_2, \mu^2\right) \hat{\sigma}_N^{a,b} \tag{3.2}$$

with the partonic cross-section $\hat{\sigma}_N^{a,b}$ being described like

$$\hat{\sigma}_N^{a,b} = \int_{PS} \left[\prod_{i=1}^{N} \frac{d^3 q_i}{(2\pi)^3 2E_i} \right] \cdot \delta^4 \left(p_1 + p_2 - \sum_i^N q_i \right) \cdot \left| \mathcal{M}^{ab}_{p_1, p_2 \to \{\vec{q}\}} \right|. \tag{3.3}$$

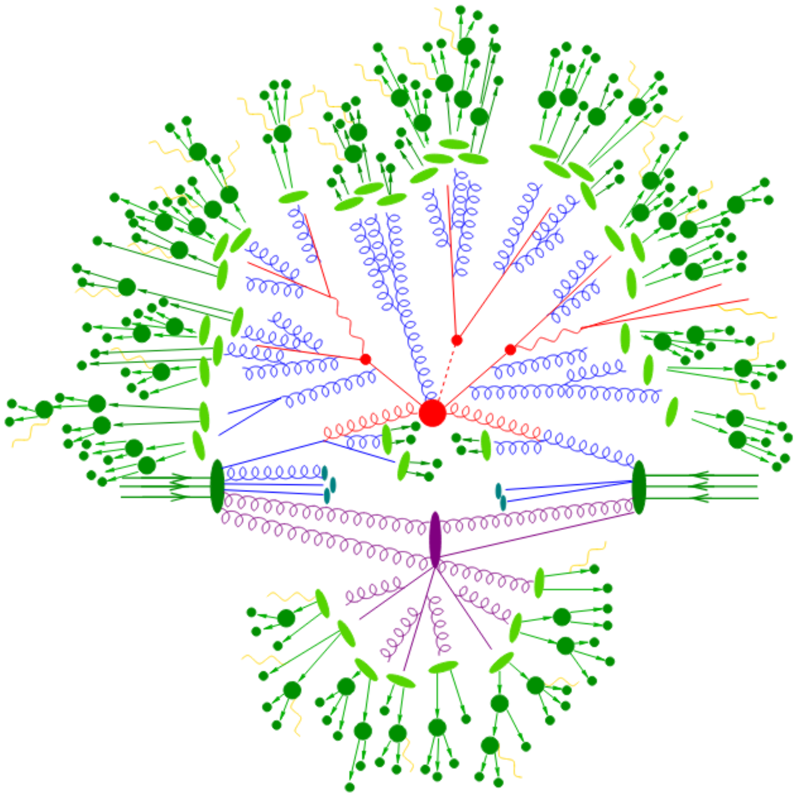

Abbildung 3.3: Stepwise depiction of a collision in the Large Hadron Collider [15].

with $\mathrm{f_{a,b}}$ being the parton density functions of the colliding protons, μ^2 being the renormalization scale and $\left|\mathcal{M}^{\mathrm{ab}}_{\mathrm{p_1,p_2}\to\{\vec{\mathrm{q}}\}}\right|$ being the parton-level matrix element. The starting point of the simulation process is marked by the point of the hard process interaction. It then propagates in specific energy scales on to the initial state protons and also into the final state hadrons. For the simulation of the proton collision, the protons are not considered as one homogeneous entity, but as an arrangement of confined partons, which are modeled by a parton distribution function (PDF). The PDF carries the information of how big each partons share to the overall momentum in the proton is. Parallel to the hard process a series of secondary soft collisions might take place.

Often, as an intermediate result of the hard collision, for a very brief moment heavy unstable particles are formed, for example the weak gauge bosons or the Higgs boson. These have extremely short lifetimes (e.g. $\tau_{\mathrm{Higgs}} \approx 2.1 \times 10^{-22}\,\mathrm{s}$ [12]), so brief in fact, that they are not able to leave the confines of the inner detector before they decay into further lighter particles. The resulting quarks and leptons initiate further radiation via bremsstrahlung, creating cascades of **particle showers**. The accurate simulation of the propagation of these showers is not a trivial task, since the QCD matrix elements describing this process can diverge at different points in the phase space, e.g. in the collinear limit, which is the case when two emitted partons are emitted in a fairly close angle to each another. A more thorough discussion on the topic can be found in the corresponding chapter in Ref.[28]. The core assumption follows according to the KLN-theorem, that states „Infrared singularities arising in real-emission diagrams cancel against alike divergences in virtual corrections "[1].A real emission can be thought of as a radiated parton with a larger transverse momentum than the rest of the jet, which can therefore be resolved as an independent jet, whereas a parton in a virtual emission has a transverse momentum to small to be resolved. For the mimic of the splitting behavior of the partons it is useful to treat the splitting similar to a radioactive decay. The first step is to formulate a probability that a parton will not split within a certain span of time $\Delta\mathrm{t}$ and then to subdivide this interval further into smaller steps:

$$\begin{aligned} \text{One time interval } \Delta\mathrm{t}: &\qquad 1-\Delta\mathrm{t}\cdot\mathrm{P}(\mathrm{t}) \\ \mathrm{n} \text{ time intervals }: &\qquad \left(1-\frac{\Delta\mathrm{t}}{\mathrm{n}}\mathrm{P}(\mathrm{t})\right)^{\mathrm{n}} \\ \text{For } \mathrm{n}\to\infty: &\qquad \exp\left(-\int_0^{\Delta\mathrm{t}}\mathrm{d}\mathrm{t}\mathrm{P}(\mathrm{t})\right) \end{aligned}$$

with $\mathrm{P}(\mathrm{t})$ being the probability to split within the time scale of $\Delta\mathrm{t}$, also called the Dokshitzer-Gribow-Lipatow-Altarelli-Parisi splitting kernel (DGLAP). The final exponential expression is called a Sudakov-form-factor. When the splitting function $\mathrm{P}(\mathrm{t})$ and the Sudakov-form factor $\Delta\mathrm{t}$ are multiplied, it gives the expression $\mathcal{P}(\mathrm{t})$, which represents the splitting probability at a time t. For practical application, it is necessary to randomly sample from the distribution given by the Sudakov-form-factor to gain the specific points in time for the splitting of the parton. Depending on the distribution in $\Delta\mathrm{t}$ it might be necessary to involve a veto algorithm [30].

The QCD-potential increases linearly with increasing distance, in contrast to electromagnetic potentials that get weaker the further two charges are separated. This property of the QCD-field is called confinement. After a certain amount of emissions have occured in he showering process and $\langle\mathrm{E}\rangle$ is at around $\sim 1\,\mathrm{GeV}$, the mean energy of all partons in the final state is low enough to form confined potentials. At higher $\langle\mathrm{E}\rangle$ the partons would still be able to tunnel out of these confined potential, thereby forming new quark-pairs. In this phase of the simulation process the **hadronization** begins. There are two prominent ways to decide how partons, closest to each other, should hadronize, the Lund string model and the cluster model. The Lund string model focuses on the potential in between two quarks, which can be thought of as a string. The further the partons are separated the more tension builds, causing them to bounce back together at some point leading to an oscillation. This is described as so called yo-yo-modes. The cluster model organizes the resulting partons that are color connected into clusters. Through preconfinement, gluon emissions into a similar direction are suppressed because of destructive interference, which causes partons close in color space to also be close in phase space. From there heavier clusters are decaying into lighter clusters until the contained partons can finally hadronize. The difference between these two models is their notion of „closeness“. The Lund string model will pair the two closet compatibly charged partons into a string, while the cluster model will organize partons together which are close in color space. For a realistic approach a mixture of both is recommended, but this stillremains an active area of research.

To create a more realistic event, it is also necessary to simulate the **underlying event** through secondary parton-parton interactions that do not belong to the hard process. The other scatterings can be constructed by using the PDF of the proton, thereby simulating all the additional kinematic information and parton showers of the other parton-parton collisions. Even though the parton showering algorithm is the same, the resulting hadronized final states can be tracked back to the different initial collision by their color connections.

Often heavy hadrons formed in the hadronization process are not in their final form when they are being measured and the remaining **unstable particles must be decayed**. This is usually achieved with decay tables, which are equipped with there own models and matrix-elements to handle multibody decays. They are further decayed into pions and kaons, that are long-lived enough to be measured in a detector.

The HHVBF_UFO-model As mentioned beforehand, Monte Carlo event generators are not just able to model high energy physics as it is formulated by the Standard Model, but they also allow to extend the theoretical description through certain models. The HHVBF_UFO-model [4] allows to tune the coupling modifiers correlating to the Higgs self- and gauge-couplings introduced in the end of section 2.2. They are denoted as the parameters $\mathrm{C_V}$, which is connected to the VVh-vertex, $\mathrm{C_3}$, which modifies the Higgs triple-self-coupling vertex hhh and $\mathrm{C_{2V}}$, which refers to the quartic-gauge-Higgs coupling in the VVhh-vertex. It is commonly used for di-Higgs analyses, but has also found its use in VBS studies [6],[23]. The HHVBF-model does only operate at leading order and is also only compatible with the matrix element generator Comix when used with Sherpa.

4 Simulation Setup

4.1 Event Generation with Sherpa

All Monte Carlo samples that have been generated for this thesis for the Sherpa side were created with the Sherpa 3.0.1 [15] installation on the high performance computing system Barnard at TU Dresden. The Standard Model sample for the Sherpa version without the additional HHVBF_UFO model contains 100000 unweighted events. In the case with the inclusion of the HHVBF_UFO model, there were multiple sets generated with values of $\kappa_{2\mathrm{V}}$ varying between [-7, -4, -2, 0, 1, 2, 4, 6, 8]. This range has been chosen corresponding to the values of $\kappa_{2\mathrm{V}}$ used in Ref. [13]. It the area within the actual value of $\kappa_{2\mathrm{V}}$ is to be expected. The values of κ_{V} and κ_{λ} remained unaltered at the value 1 throughout the generation of all samples. All the samples, for the Standard Model value of $\kappa_{2\mathrm{V}}$ or the samples linked to beyond the Standard Model values of $\kappa_{2\mathrm{V}}$ contain 30000 events each. The number of events corresponding to each value of $\kappa_{2\mathrm{V}}$ is relatively low compared to the above mentioned analysis, mainly to conserve computation resources, simply because of the sheer number of additional samples and the increasingly more exotic phase space to sample from. To compensate for this, all the matrix elements and the event samples have been generated with a slurm job using the mpirun-command, which enables the production of events but multiple cores in parallel.

The general settings for all the Input parameters can be found in table 4.2, but there shall be given a short explanation for some of the choices made here. The goal is to simulate a proton-proton collision at a center-of-mass energy of $13\,\mathrm{TeV}$, which corresponds to run 2 data of the ATLAS experiment [20]. All the information on the particle types are handed to the generator through the particle ID (PID) specified in the particle data group [26], for example, $\mathrm{PID}(1) = \mathrm{u}$-quark or $\mathrm{PID}(11) = \mathrm{e}$.

Particle ID	Description
2212	proton p
93	jet particle container
1, 2, 3, 4, 5	down-, up-, strange-, charm-, bottom-quark
11, 13	electron e^{-}, muon μ^{-}
12, 14	electron-neutrino ν_{e}, muon-neutrino ν_{μ}
24, -24	W^{+}-, W^{-}-boson
25	Higgs-boson h

Tabelle 4.1: .

The light quarks (up-, down-, strange-, charm-quark) and all the leptons are set to be massless. When using the particle container 93, which simply refers to a hadronic jet, all the light quarks, so also the bottom quark, are set massless by definition. In this case it has been necessary to set the

bottom quark to be massive, on the one side so the Higgs boson would later be able to couple to it, since it can only couple to massive particles, and on the other so the Higgs boson would be able to decay. This leads to the b-quark being excluded from the particle container 93. Since the PDF-library PDF4LHC21_40_pdfas chosen for the simulation is independent from this fact, utilizing a 5-flavor scheme has no further influence on the simulation. As the hard scattering, the $\mathrm{jj} \rightarrow \mathrm{W}^{\pm}\mathrm{W}^{\pm}\mathrm{hjj}$ process is formulated in terms of PIDs. Sherpa enables the user to specify the number of coupling orders of a certain interaction that should be used in the Feynman diagrams drawn for the matrix element calculation. In this case, no QCD diagrams shall be considered, but the default setting 'Any' is used for the order of electroweak couplings. At LO, this translates to 5 orders of electroweak couplings. The $\mathrm{W}^{\pm}$-bosons and the Higgs-boson, resulting directly from the hard scattering, are forced through the hard decay setting to further decay like $\mathrm{h} \rightarrow \mathrm{b}\bar{\mathrm{b}}$, and $\mathrm{W}^{+} \rightarrow \mathrm{l}_{\mathrm{e},\mu} + \bar{\nu}_{\mathrm{e},\mu}$ or $\mathrm{W}^{-} \rightarrow \mathrm{l}_{\mathrm{e},\mu} + \nu_{\mathrm{e},\mu}$. The additional setting $\{\mathrm{Status{:}2}\}$ means that the decay channel is being forced. The order of QCD interactions is set to 0 to avoid the production of non-contributing events, which can be set without risking gauge invariance.
The runcard also gives some restrictions on the phase space the events are being sampled from. So only jets with a minimum transverse momentum of $\mathrm{p_T} > 10\,\mathrm{GeV}$, a pseudorapidity $\eta = -\ln\tan\left(\frac{\theta}{2}\right)$ range within $-5.5 < \eta < 5.5$ and a minimum angular separation of $\Delta\mathrm{R} = \sqrt{(\eta_{\mathrm{j},1} - \eta_{\mathrm{j},2})^2 + (\varphi_{\mathrm{j},1} - \varphi_{\mathrm{j},2})^2} > 0.4$ between the jets are being sampled. This pre-selection increases the number of viable events to use for the analysis later. Since Sherpa only allows to set selector cuts on particles appearing in the final state of the hard scattering, it was not possible to further cut on the b-tagged jets or the leptons, since those only appear in the hard decay.

In this thesis the Narrow-Width-Approximation is being used. A condition to use the it is that the decay width of a particle is low compared to its mass, which is fulfilled for the Higgs boson and the W-boson. With the Narrow-Width-Approximation it is possible to factorize the production and decay matrix element, which simplifies, for example, the phase space integration. To implement this into the event generation, the decay width of the bosons are set to zero and they only become unstable in the decay process. The problem arising from this, regarding the signal process in this thesis, is that Feynman diagrams with an intermediate Higgs boson in them exist, which leads to divergences since the Higgs boson can go on-shell. This is avoided by leaving the decay width of the Higgs > 0, thereby not risking this behavior, but also, strictly spoken, makes the process not gauge invariant. This considered, leads to the process being defined in Sherpa as 93 93 -> 24 24 25 93 93.

Model-type	Input Parameter	Setting
Standard Model :		
	Beam-type Beam energies PDF interface Matrix element generator	BEAM: 2212 BEAM_ENERGIES: 6500 PDF_LIBRARY: PDF4LHC21_40_pdfas ME_GENERATOR: Comix
	Particle parameters	PARTICLE_DATA: 1, 2, 3, 4: {Massive: false} 11, 13, 15: {Massive: false} 5: {Massive: true} 24: {Mass: 8.038485e+01} 25: {Mass: 1.250000e+02, Stable: 0}
	Process definition	PROCESSES: 93 93 -> 24 24 25 93 93 93 93 -> -24 -24 25 93 93 Order: {QCD: 0, EW: Any}
	Hard decay definition	HARD_DECAYS: 25,5,-5: {Status: 2} 24,12,-11: {Status: 2} 24,14,-13: {Status: 2} -24,-12,11: {Status: 2} -24,-14,13: {Status: 2}
	Selection cuts	SELECTORS: [PT, 93, 10.0, E_CMS] [DR, 93, 93, 0.4, 100] [Eta, 93, -5.5, 5.5]
HHVBF_UFO Model:		
	Process definition	93 93 -> 24 24 25 93 93 93 93 -> -24 -24 25 93 93 Order: {QCD: 0, QED: Any, C3: Any, C2V: Any, CV: Any}
	Additional UFO-info	UFO_PARAMS: 1 1 # CV 2 1 # C2V 3 1 # C3

Tabelle 4.2: Table of the the relevant runcard settings for the Standard Model and UFO model settings in Sherpa. The general settings for the UFO model are mostly similar to the ones of the Standard Model, so only the extensions are added to the table. If not further specified the Standard Model value is assumed for generation.

4.2 Madgraph Samples

The events that are being compared with the Sherpa samples have been generated with MadGraph5_aMC@NLO in the Athena framework, version AthGeneration-23.6.6. . They have been generated in similar fashion to the samples used in connection to the research in Ref. [13] and have not been changed in any way, but only imported for this analysis. As a matrix element generator Madgraph (version 3.3.1.atlas4) had been used and for the parton shower Pythia 8 (version 3.0.8) has been added. The only exception from that marks the Standard Model sample, which was showered with Herwig 7.2.3. All necessary runcard inputs are shown in table 4.3. The sample size for the Standard Model case count 100000, for all beyond Standard Models 10000 events per setting of the $\kappa_{2\mathrm{V}}$-parameter are used. All Madgraph samples have been created for the same set of values of $\kappa_{2\mathrm{V}}$, as mentioned in the beforehand section using also the HHVBF_UFO model. Madgraph allows to implement additional cuts on the hard decay products when generating events. This not only allows to generate events more fitting to the phase space area that is relevant to the signal process, the cuts on the angular distribution of the jets and leptons avoid overlap between them. Also it is worth to mention, that Madgraph does not factor in the branching ratio of the selected decay channel (in this case $\mathrm{h} \to \mathrm{b\bar{b}}$) into the total cross-section, which is automatically performed in Sherpa. A difference to the Sherpa setup is, that the b-quark is explicitly set to be massless in the Madgraph runcard, which is valid to assume, since the energy scale treated here is large enough to render its mass negligible. The coupling to the Higgs-boson is still granted through the Yukawa-coupling not being set to zero.

Input Parameter	Setting
Beam-type	lpp1 = 1, lpp2 = 1
Beam energies	ebeam1 = 6500.0, ebeam2 = 6500.0
PDF interface	pdlabel = MadGraph_NNPDF30NLO_Base_Fragment
Matrix element generator	MadGraph(v.3.3.1.atlas4), Pythia8(v.3.0.8)
Particle parameters	Masses: $\mathrm{m_{u,d,s,c,b}} = 0$ $\mathrm{m}_{\nu_\mathrm{e}}, \mathrm{m}_{\nu_\mu}, \mathrm{m}_{\nu_\tau} = 0$ $\mathrm{m_e} = 0.511\,\mathrm{MeV}$ $\mathrm{m}_\mu = 0.106\,\mathrm{GeV}$ $\mathrm{m}_\tau = 1.777\,\mathrm{GeV}$ $\mathrm{m_Z} = 91.188\,\mathrm{GeV}$ $\mathrm{m_W} = 80.385\,\mathrm{GeV}$ $\mathrm{m_h} = 125\,\mathrm{GeV}$ Decay Width: $\Gamma_\mathrm{u,d,s,c,b} = 0$ $\Gamma_{\mathrm{e},\mu,\tau,\nu_\mathrm{e},\nu_\mathrm{mu},\nu_\tau} = 0$ $\Gamma_\mathrm{t} = 1.508\frac{1}{\mathrm{GeV}}$ $\Gamma_\mathrm{Z} = 2.495\frac{1}{\mathrm{GeV}}$ $\Gamma_\mathrm{W} = 2.085\frac{1}{\mathrm{GeV}}$ $\Gamma_\mathrm{h} = 0.0041\frac{1}{\mathrm{GeV}}$
Process definition	generate p p > w+ w+ h j j QCD=0, w+ > l+ vl QCD=0 @0 add process p p > w- w- h j j QCD=0,w- > l- vl QCD=0 @0
Selection cuts	ptj = 10.0, ptl = 4.0 etaj = 5.5, etal = 4.0 drjj = 0.4, drll = 0.2, drjl = 0.2

Tabelle 4.3: All relevant setting for the Madgraph event generation. There is no additional paragraph for the settings with the HHVBF_UFO model, since even the Standard Model was produced with it, set to the SM limit.

4.3 Analysis via Rivet

All the event samples in this thesis will be analyzed with the analysis tool kit Rivet [5], more specific with different versions of Rivet 4 [3]:

- The Sherpa event samples have been analyzed with the Rivet4.0.1 installation on Barnard. The resulting data is stored in the yoda format, version 2.0.1 .
- The event samples generated in Madgraph were analyzed within the Athena framework version 23.6.50, which has Rivet4.1.0 implemented and uses the yoda version 2.1.0. . To deal with the EVNT-format of the Madgraph samples, since Rivet on its own was not able to interpret these, the i_Rivet wrapper in Athena is necessary, which can be used with an additional job option.

Where multiple yoda files have been created, which still contribute to the same event sample (e.g. the Standard Model samples from the Madgraph), they have been merged with the yodamerge command. The used analyses have been compiled in separate directories with the corresponding versions of Rivet. All the analyses are at truth-level, meaning that there are no additional tools at work for the reconstruction of inherent properties, like e.g. particle type, or kinematic ones. Some baseline assumptions are: Tau leptons are excluded from the final state, only electrons or muons and their anti-particles are considered. The jet reconstruction is done with the Anti-kt algorithm [7], the R-parameter is set to 0.4. There are also some basic cuts necessary to avoid segmentation faults while running which all concern the minimum number of certain particles. Events are vetoed if $\mathrm{N_{leptons}} < 2$, $\mathrm{N_{jets}} < 4$, $\mathrm{N_{b-jets}} \neq 2$ or $\mathrm{N_{light\,jets}} < 2$, where the leptons are selected from the prompt final state.
The analyses in the following chapters deal with the following observables and use the below mentioned additional cuts:

Validation observables: The goal in this part is to investigate on possible differences between the event generators Madgraph and Sherpa, concerning the VBS process $\mathrm{jj} \rightarrow \mathrm{W^{\pm}W^{\pm}hjj}$, therefore observables that are strongly connected to this process are investigated here, like:

- $\mathrm{m_{jj}}$: Invariant mass of the 2 leading jets. This observable is depicted in 2 separate plots, one for a low energy region ($\mathrm{m_{jj}}$-close) and also one for higher energies ($\mathrm{m_{jj}}$-wide) .
- $\Delta\eta_{\mathrm{jj}}$: Difference in pseudorapidity η between both of the leading jets.

There are only baseline cuts added, like $\mathrm{p_{T_j}}, \mathrm{p_{T_l}} > 20\,\mathrm{GeV}$, $\left|\eta_{\mathrm{j}}\right| < 4.5$ and $\left|\eta_{\mathrm{lep}}\right| < 2.5$, to avoid additional low-energy decay products, resulting from particle showers.

The DNN-Analysis observables: In [13] there is a section on how a deep neural network (DNN) is trained and used to distinguish SM events from beyond SM ones, using only elementary features of a high energy particle collision. The features in question span:

- $\mathrm{p_{T,l_1}}$, $\mathrm{p_{T,l_2}}$: Transverse momentum of the leading and sub-leading lepton.
- $\eta_{\mathrm{l_1}}$, $\eta_{\mathrm{l_2}}$: Pseudorapidity of the leading and sub-leading lepton.
- $\varphi_{\mathrm{l_1}}$, $\varphi_{\mathrm{l_2}}$: Azimuthal angle of the leading and sub-leading lepton.
- $\mathrm{m_{hj_1}}$, $\mathrm{m_{hj_2}}$: Higgs jet mass of the leading and sub-leading b-tagged jet.
- $\mathrm{p_{T,hj_1}}$, $\mathrm{p_{T,hj_2}}$: Transverse momentum of the leading and sub-leading b-tagged jet.
- $\eta_{\mathrm{hj_1}}$, $\eta_{\mathrm{hj_2}}$: Pseudorapidity of the leading and sub-leading b-tagged jet.
- $\varphi_{\mathrm{hj_1}}$, $\varphi_{\mathrm{hj_2}}$: Azimuthal angle of the leading and sub-leading b-tagged jet.
- $\mathrm{E_{T,Miss}}$: Missing transverse energy.

In this case there are no further specified cuts.

Analysis for κ_{2V} sensitive observables: These observables have already been used in Ref. [23] for the analysis of the triple-higgs coupling modifier κ_λ but they are also promising for the investigation of the κ_{2V}-parameter. The observables are of higher complexity than the ones used in the DNN-analysis:

- m_{WWh}: Invariant mass of the $W^\pm$-bosons and the Higgs boson.
- m_{WWh_T}: Transverse mass of the $W^\pm$-bosons and the Higgs boson.
- m_{ll_T}: Transverse mass of the leading leptons.
- m_{WW_T}: Transverse mass of the $W^\pm$-bosons.
- p^{bal}_{WW}: Transverse momentum balance between $W^\pm$-bosons. It is defined like:

$$p^{bal}_{WW} = \frac{\sqrt{p_{x,W_1} + p_{x,W_2} + p_{y,W_1} + p_{y,W_2}}}{p_{T,W_1} + p_{T,W_2}} \tag{4.1}$$

- R_{p_T}: Ratio transverse momenta of leptons and jets. It is defined like:

$$R_{p_T} = \frac{p_T^{l_1} \cdot p_T^{l_2}}{p_T^{j_1} \cdot p_T^{j_2}} \tag{4.2}$$

The observables related to the transverse mass are calculated like:

$$m_T = \sqrt{\left(\sum_i^3 \sqrt{(m_i^2 + p_{T,i}^2)}\right)^2 - \left(\sum_i^3 \vec{p}_{T,i}\right)^2} \tag{4.3}$$

In this case additional cuts are being used, to better select for events with a more fitting VBS-character. The invariant mass of the leading jets m_{jj} is set to $m_{jj} > 300\,\mathrm{GeV}$ and the missing transverse energy $\mathrm{MET} > 30\,\mathrm{GeV}$. There is also an additional cut setting the number of $n_{W^\pm} > 2$ and $n_h > 1$ to again avoid segmentation faults when running the analysis.

5 Results

5.1 Standard Model Validation of Sherpa, Sherpa + UFO-Model and Madgraph Samples

The validation of the Standard Model samples, created in the aforementioned setups, shall provide a first insight on if the implementation of the UFO-model influences the resulting events in any other way then intended. Therefore a set of samples created with the standard configuration of Sherpa is being compared with samples from Sherpa and Madgraph, using the HHVBF_UFO model, in the Standard Model limit.

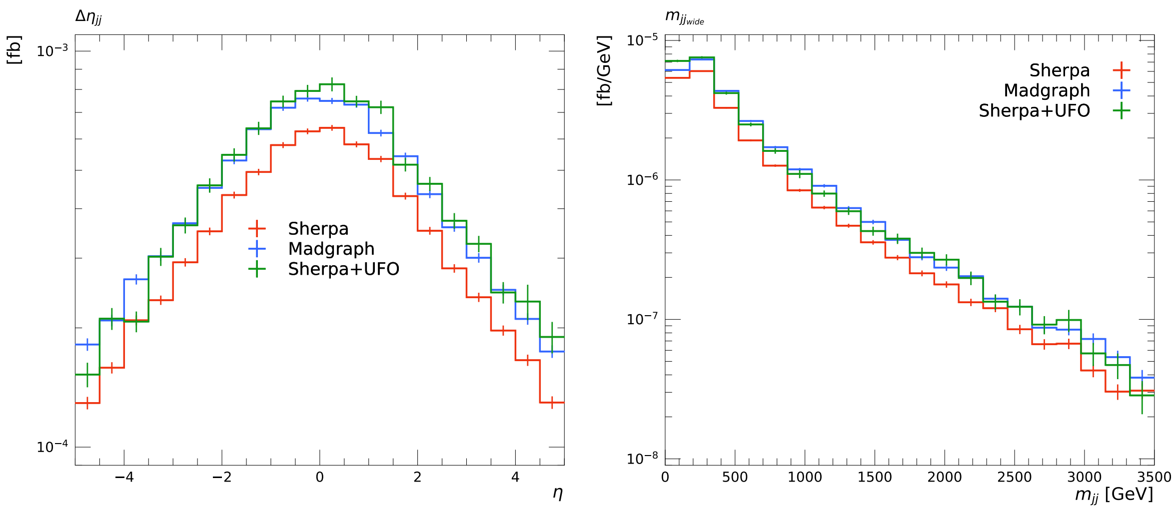

(a) (b)

Abbildung 5.1: Comparison of the event generators Sherpa, Sherpa with the HHVBF-UFO-model implementation and Madgraph regarding the observables $\Delta\eta_{\mathrm{jj}}$ and $\mathrm{m_{jj}}$.

As visible in figure 5.1, the shape of the plots are very similar, differences between them mostly arise from different total cross-sections, creating an offset between the standard Sherpa setup and the ones with the UFO-implementation (It should be mentioned that the graph representing the Madgraph samples has already been adjusted for the not included branching ratio of $\mathrm{BR(h \rightarrow b\bar{b})}$). The actual values are thus $\sigma_{\mathrm{Sherpa}} = 8.62 \cdot 10^{-3}\mathrm{fb}$, $\sigma_{\mathrm{Sherpa+UFO}} = 1.12 \cdot 10^{-2}\mathrm{fb}$ and $\sigma_{\mathrm{Madgraph}} = 1.05 \cdot 10^{-2}\mathrm{fb}$. The most likely cause for the difference in cross-sections is the vast difference in Feynman diagrams, that are being used for the matrix element generation. It is possible to have all the drawn Feynman diagrams, that were created in the matrix element generation, printed and added to the output. Since the jets in the $\mathrm{jj} \rightarrow \mathrm{W^{\pm}W^{\pm}hjj}$-process are represented by a particle container, the diagrams must consider all possible quark lines that can be formed through the light quarks $\mathrm{u, d, s, c}$ (the b-quark is not contained in the particle container since it is set to be massive).

Process with specified quark lines	Number of Diagrams
• $\mathrm{jj} \rightarrow \mathrm{W^+W^+hjj}$:	
$\mathrm{u\bar{d}} \rightarrow \mathrm{W^+W^+h} \quad \mathrm{d\bar{u}}$	288
$\mathrm{uc} \rightarrow \mathrm{W^+W^+h} \quad \mathrm{ds}$	144
$\mathrm{\bar{d}\bar{d}} \rightarrow \mathrm{W^+W^+h} \quad \mathrm{\bar{u}\bar{u}}$	288
$\mathrm{uu} \rightarrow \mathrm{W^+W^+h} \quad \mathrm{dd}$	288
$\mathrm{\bar{d}\bar{s}} \rightarrow \mathrm{W^+W^+h} \quad \mathrm{\bar{u}\bar{c}}$	144
$\mathrm{c\bar{d}} \rightarrow \mathrm{W^+W^+h} \quad \mathrm{s\bar{u}}$	144
$\mathrm{u\bar{d}} \rightarrow \mathrm{W^+W^+h} \quad \mathrm{s\bar{c}}$	144
• $\mathrm{jj} \rightarrow \mathrm{W^-W^-hjj}$:	
$\mathrm{d\bar{c}} \rightarrow \mathrm{W^-W^-h} \quad \mathrm{u\bar{s}}$	144
$\mathrm{dd} \rightarrow \mathrm{W^-W^-h} \quad \mathrm{uu}$	288
$\mathrm{\bar{u}\bar{u}} \rightarrow \mathrm{W^-W^-h} \quad \mathrm{\bar{d}\bar{d}}$	288
$\mathrm{ds} \rightarrow \mathrm{W^-W^-h} \quad \mathrm{uc}$	144
$\mathrm{\bar{u}\bar{c}} \rightarrow \mathrm{W^-W^-h} \quad \mathrm{\bar{d}\bar{s}}$	144
$\mathrm{d\bar{u}} \rightarrow \mathrm{W^-W^-h} \quad \mathrm{c\bar{s}}$	144
$\mathrm{d\bar{u}} \rightarrow \mathrm{W^-W^-h} \quad \mathrm{u\bar{d}}$	288

Tabelle 5.1: All used sets of quark lines for the generation of Feynman diagrams in the signal process by the standard Sherpa configuration.

For the standard Sherpa setup, this results in seven different quark configurations for each W-boson charge with again either 288 or 144 Feynman diagrams attached. The number of diagrams is halved in some cases through the switch in quark generation taking place. In case of the Sherpa setup with the HHVBF_UFO model implementation, there are in total 34 quark configurations considered for each W-boson charge, each being linked to 360 Feynman diagrams. This indicates that in the standard Sherpa case, the creation of Feynman diagrams is in some way selective, while in the UFO model case all possibilities are being considered

5.2 Validation for Samples with Varying $\kappa_{2\mathrm{V}}$

Since it could be shown, that the generated events from Madgraph and Sherpa, both using the HHVBF_UFO-model, act fairly similar in the Standard Model limit, the generators shall now be tested for varying values of the $\kappa_{2\mathrm{V}}$ coupling parameter. As mentioned before, the $\kappa_{2\mathrm{V}}$ - parameter is set to the values $[8, 6, 4, 2, 1, 0, -2, -4, -7]$. As in the previous section, the observables $\Delta\eta_{\mathrm{jj}}$ and $\mathrm{m_{jj}}$ are being used to compare the influence of the different values of the $\kappa_{2\mathrm{V}}$-parameter (see figure 5.2). In all plots it is clearly visible that the total cross-sections increase the more the $\kappa_{2\mathrm{V}}$ parameter deviates from the Standard Model value. This happens in almost symmetrical fashion, with graphs belonging to $\kappa_{2\mathrm{V}}$ values that are equally deviant from the Standard Model value, lying closely together. While the variation of the $\kappa_{2\mathrm{V}}$-coupling parameter does not seem to have an impact on the shape of the graphs in the $\Delta\eta_{\mathrm{jj}}$-plot, there is a visible difference in shape in the $\mathrm{m_{jj}}$-plot, at least when the Standard Model limit is compared to the beyond Standard Model cases. In the Standard Model case, the distribution peaks at a lower energy than for any beyond Standard Model case and it also falls of steeper towards higher energies until the graph starts to flatten. For the distributions with $\kappa_{2\mathrm{V}} \neq 1$, they all peak at close to $\mathrm{m_{jj}} = 500\,\mathrm{GeV}$ and decrease for higher energies exponentially, showing in the logarithmic plot as an almost straight line.

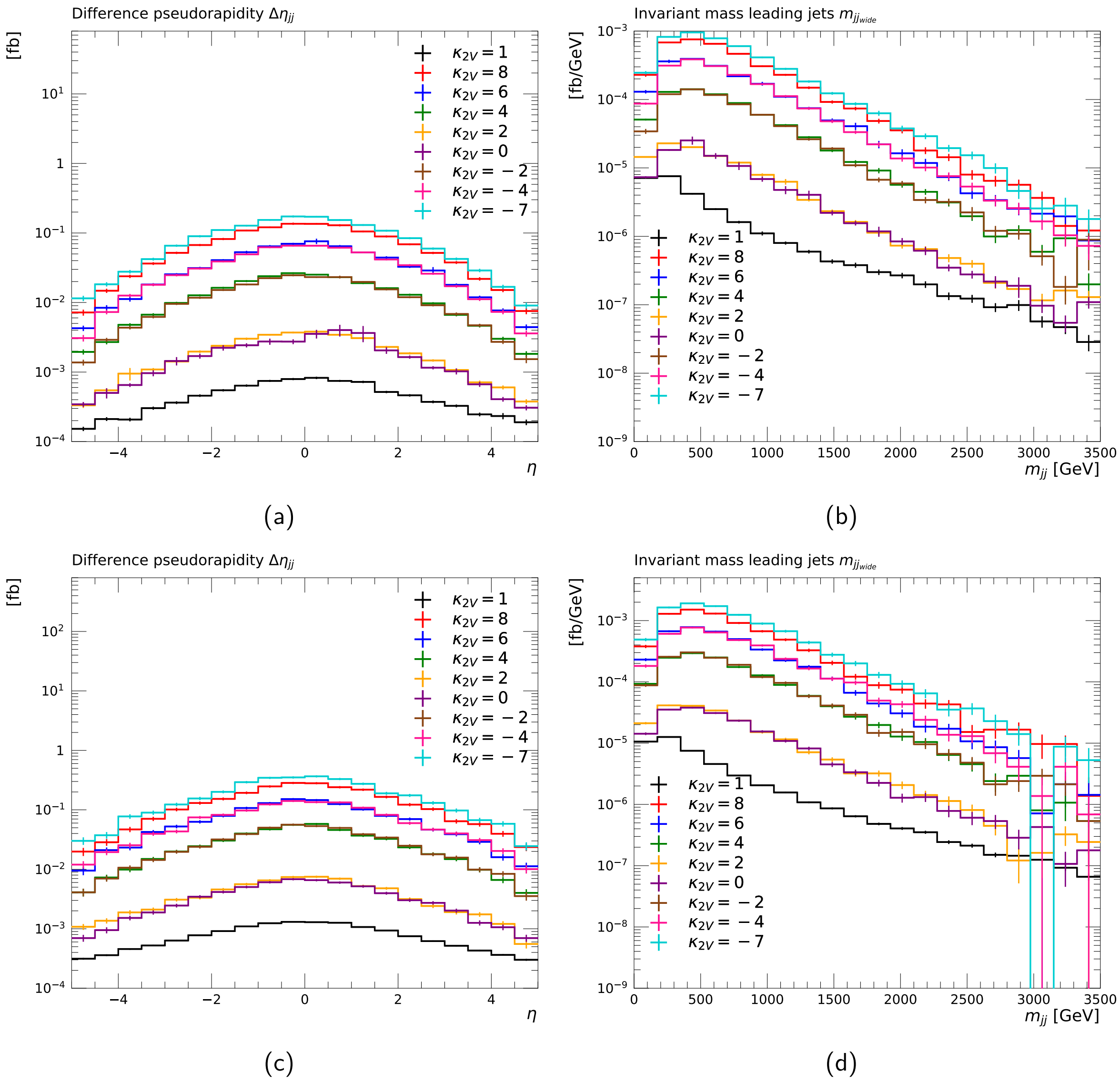

Abbildung 5.2: Comparison of the observables $\Delta\eta_{\mathrm{jj}}$ and $\mathrm{m_{jj}}$ for multiple values of $\kappa_{2\mathrm{V}}$ applied for samples generated by a), b) Sherpa and c), d) Madgraph.

When comparing the results from the different samples of Madgraph and Sherpa, no differences in shape are directly apparent, but there are are still remaining some differences in the total cross-sections, even when taking account for the missing branching ratio factor in the Madgraph samples. All the total cross-sections for the samples are displayed in table 5.2, where the values for the Sherpa samples have been collected from the output-file after the event generation and the cross-sections for the Madgraph samples were taken from [13]. In addition to both of the total cross-sections for different coupling parameters there is a column giving the scaling factor from the total cross-section from the Sherpa samples compared to the ones from Madgraph, adjusted for the missing branching ratio. The course of this ratio along the different values of $\kappa_{2\mathrm{V}}$ is visualized in 5.3. Only for the Standard Model case the Sherpa samples as well as the Madgraph samples have similar total cross-sections. For an increase of $\kappa_{2\mathrm{V}}$ deviating from the Standard model case, the ratio between both samples seems to stabilize at a factor close to ≈ 0.8.

Value κ_{2V}	total σ_{Sherpa} [pb]	total σ_{Madgraph} [pb]	$\frac{\sigma_{\text{Sherpa}}}{\sigma_{\text{Madgraph}} \cdot \text{BR}(h \to b\bar{b})}$
1	0,0000112 $\pm 7.298 \cdot 10^{-8}$	0,0000181 $\pm 3,330 \cdot 10^{-7}$	1,0669
8	0,00113 $\pm 8,899 \cdot 10^{6}$	0,00238 $\pm 5,137 \cdot 10^{-6}$	0,8186
6	0,000578 $\pm 5,026 \cdot 10^{6}$	0,00123 $\pm 3,056 \cdot 10^{-6}$	0,8102
4	0,000201 $\pm 1,38 \cdot 10^{-6}$	0,000459 $\pm 8,355 \cdot 10^{-7}$	0,7550
2	0,000036 $\pm 2,599 \cdot 10^{7}$	0,0000703 $\pm 1,453 \cdot 10^{-7}$	0,8829
0	0,0000312 $\pm 7,709 \cdot 10^{7}$	0,0000614 $\pm 1,336 \cdot 10^{-7}$	0,8760
-2	0,000201 $\pm 1,071 \cdot 10^{6}$	0,000459 $\pm 9,446 \cdot 10^{-7}$	0,7550
-4	0,000543 $\pm 3,557 \cdot 10^{6}$	0,00118 $\pm 2,571 \cdot 10^{-6}$	0,7934
-7	0,00139 $\pm 1,145 \cdot 10^{5}$	0,00302 $\pm 5,736 \cdot 10^{-6}$	0,7936

Tabelle 5.2: Total cross-sections of the event samples created with Sherpa, with Madgraph and the ratio of the total cross-section of Sherpa and Madgraph adjusted for branching ratio.

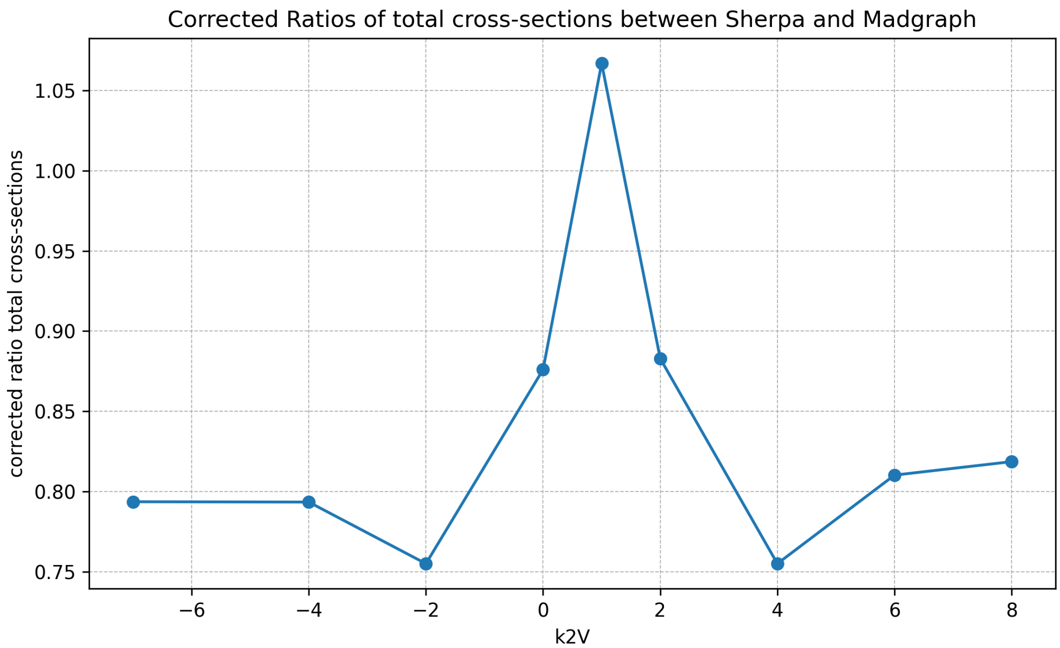

Abbildung 5.3: Ratios of the total cross-sections between Sherpa and Madgraph, corrected for the branching ration $\text{BR}(h \to b\bar{b}) \approx 0.58$.

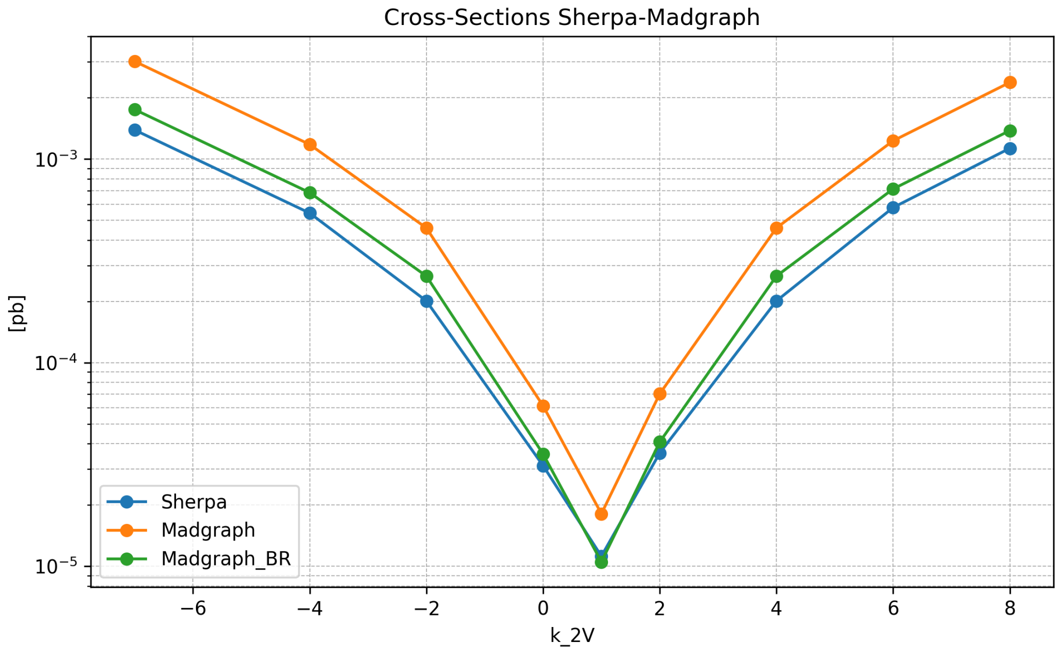

Abbildung 5.4: Comparison of all the total cross-sections for the event samples from Sherpa, Madgraph without adjusting for the branching ratio and Madgraph with adjustment.

5.3 Studies of Sensitive Observables with Varying $\kappa_{2\mathrm{V}}$

5.3.1 Cut-Flow-Analysis

The generated samples for the $\mathrm{jj} \to \mathrm{W}^{\pm}\mathrm{W}^{\pm}\mathrm{hjj}$-process are, at this point of the analysis, not further selected for any kinematic properties. Since for the further analysis, events with VBS characteristics are necessary, certain cuts were applied (described in section 4.3). To investigate on how these cuts influence the total amount of samples, a Cut Flow plot has been created. The bin the furthest to the left represents the sample size without any cuts applied and any further bin shows the amount of events left after a cut.

As shown in figure 5.5, certain cuts have more influence on the total sample size than others. The ones with the most impact are the one for securing more than 2 leptons in the prompt final state, the one allowing only exactly 2 b-tagged jets in the final state and the one demanding an invariant mass higher than $300\,\mathrm{GeV}$ between the non-b-tagged light jets. While for the Standard Model limit almost 80% of the total number of events are rejected, for varying values of $\kappa_{2\mathrm{V}}$ the total amount is only decreased by around 50%. This seems reasonable, since an increased value of $\kappa_{2\mathrm{V}}$ emphasizes the diagrams contributing to the signal process with exactly the VBS characteristics searched for here.

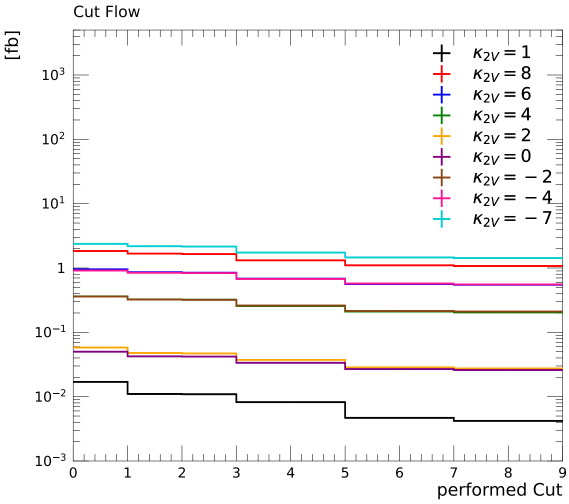

(a)

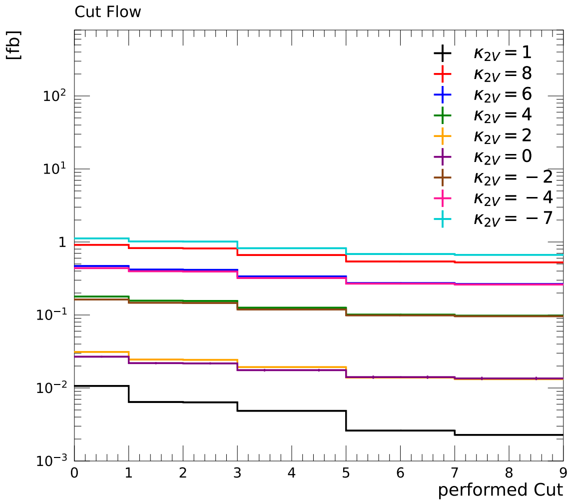

(b)

Abbildung 5.5: Cut-Flow plots for a) Madgraph samples and b) Sherpa samples concerning the VBS Cuts mentioned in 4.3 for varying values of $\kappa_{2\mathrm{V}}$. The bins represent the cuts 1) more than 2 leptons, 2) more than 4 jets, 3) Exactly 2 b-tagged jets, 4) more than 2 light jets, 5) Invariant mass of light jets is higher than $300\,\mathrm{GeV}$, 6) the leptons are same-sign, 7) more than $30\,\mathrm{GeV}$ of $\mathrm{E_{Tmiss}}$ and 8) more than or exactly 2 $\mathrm{W}^{\pm}$-bosons and more than or exactly 1 Higgs boson.

5.3.2 Study of Sensitive Observables

To get a better insight on how the different values of $\kappa_{2\mathrm{V}}$ influence the distribution, all corresponding histograms are shown together in one plot. This will be done separately for the Sherpa and the Madgraph data sets. Only after that first examination differences between both event generator will be addressed.
The histograms of the ratio of the transverse momenta $\mathrm{R_{pt}}$ only really vary in total cross-section and their shapes do not seem to be influenced by the alteration of the $\kappa_{2\mathrm{V}}$-parameter. Also, the Madgraph samples result in histograms that do not allow any meaningful interpretation, since the variance from bin to bin is simply to significant for higher deviations of $\kappa_{2\mathrm{V}}$ from the Standard Model. Therefore it will not be further discussed here. Apart from the increase in total cross-sections, some of the histograms show a variation of shape for further deviant $\kappa_{2\mathrm{V}}$ value. The most subtile changes in shape between the Standard Model case and the beyond Standard Model histograms take place for the distributions of the $\mathrm{m_{WWh_T}}$-observable. Depending on the choice of samples, there is either a steeper decrease in events for higher energies or one that acts at the same rate as in the beyond Standard Model case. This will be visualized later in this section. The transverse momentum balance $\mathrm{p_{T,WW}^{bal}}$ shifts from a more even distribution with an indistinguishable maximum to a clear peak at low values of $\mathrm{p_{T,WW}^{bal}}$. Since this behavior is equally visible in both, the Madgraph and the Sherpa samples, they will not be further investigated in this regard here. The corresponding plots can be found in the appendix.
All the other observables, $\mathrm{m_{ll_T}}$, $\mathrm{m_{WW_T}}$ and $\mathrm{m_{WWh}}$ show a clear variation in shape for different values of $\kappa_{2\mathrm{V}}$.

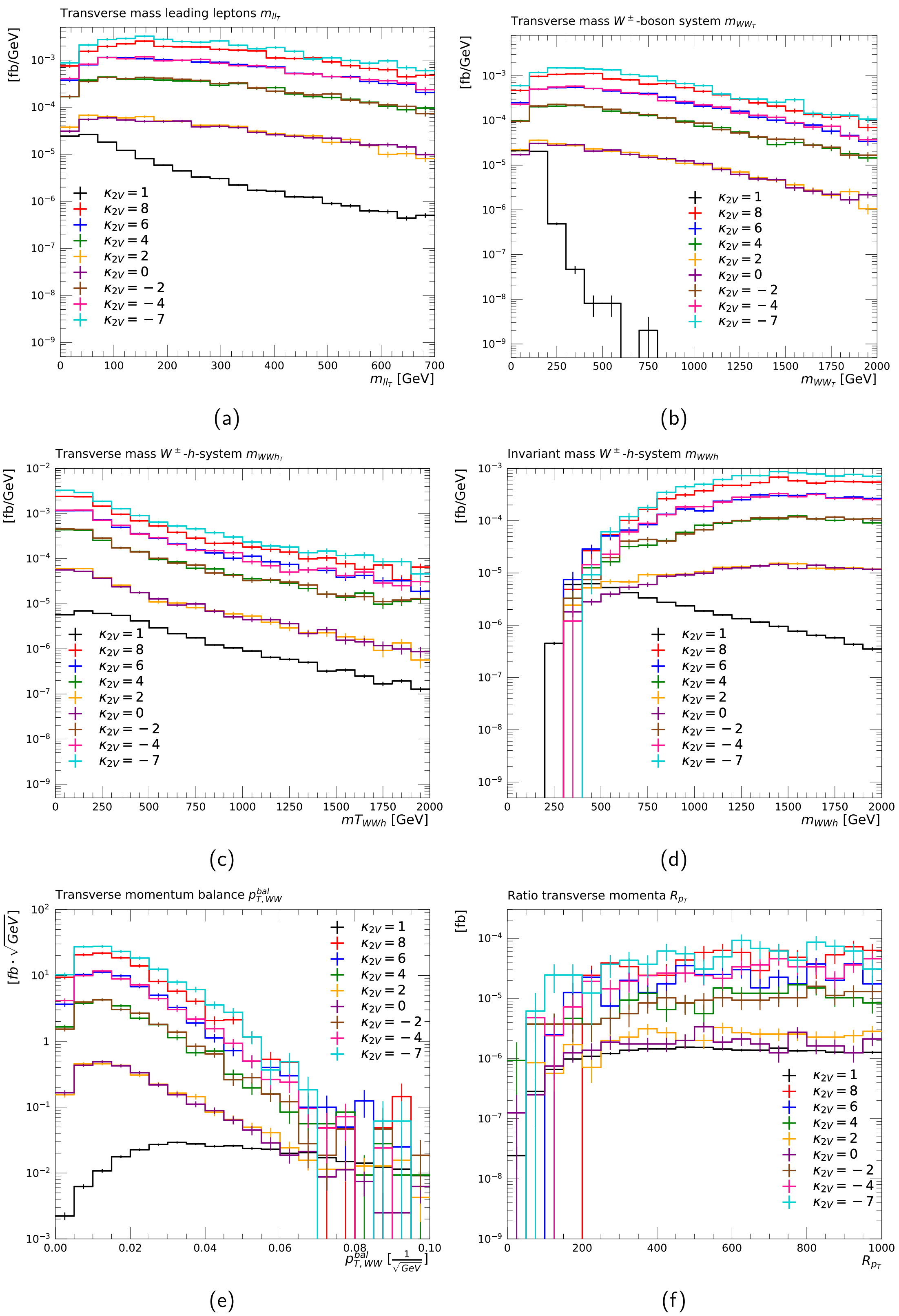

Abbildung 5.6: Plots for the sensitive observables a)Transverse mass of leasding leptons $\mathrm{m_{ll_T}}$, b) Transverse mass of $\mathrm{W^{\pm}}$-boson system $\mathrm{m_{WW_T}}$ c) Transeverse mass of $\mathrm{W^{\pm} - h}$-boson system $\mathrm{m_{WWh_T}}$, d) Invariant mass of $\mathrm{W^{\pm}}$–h system $\mathrm{m_{WWh}}$, e) Transverse momentum balance $\mathrm{p^{bal}_{T,WW}}$ and f) Ratio of transverse momenta $\mathrm{R_{p_T}}$ through varying values of κ_{2V} in Madgraph event samples.

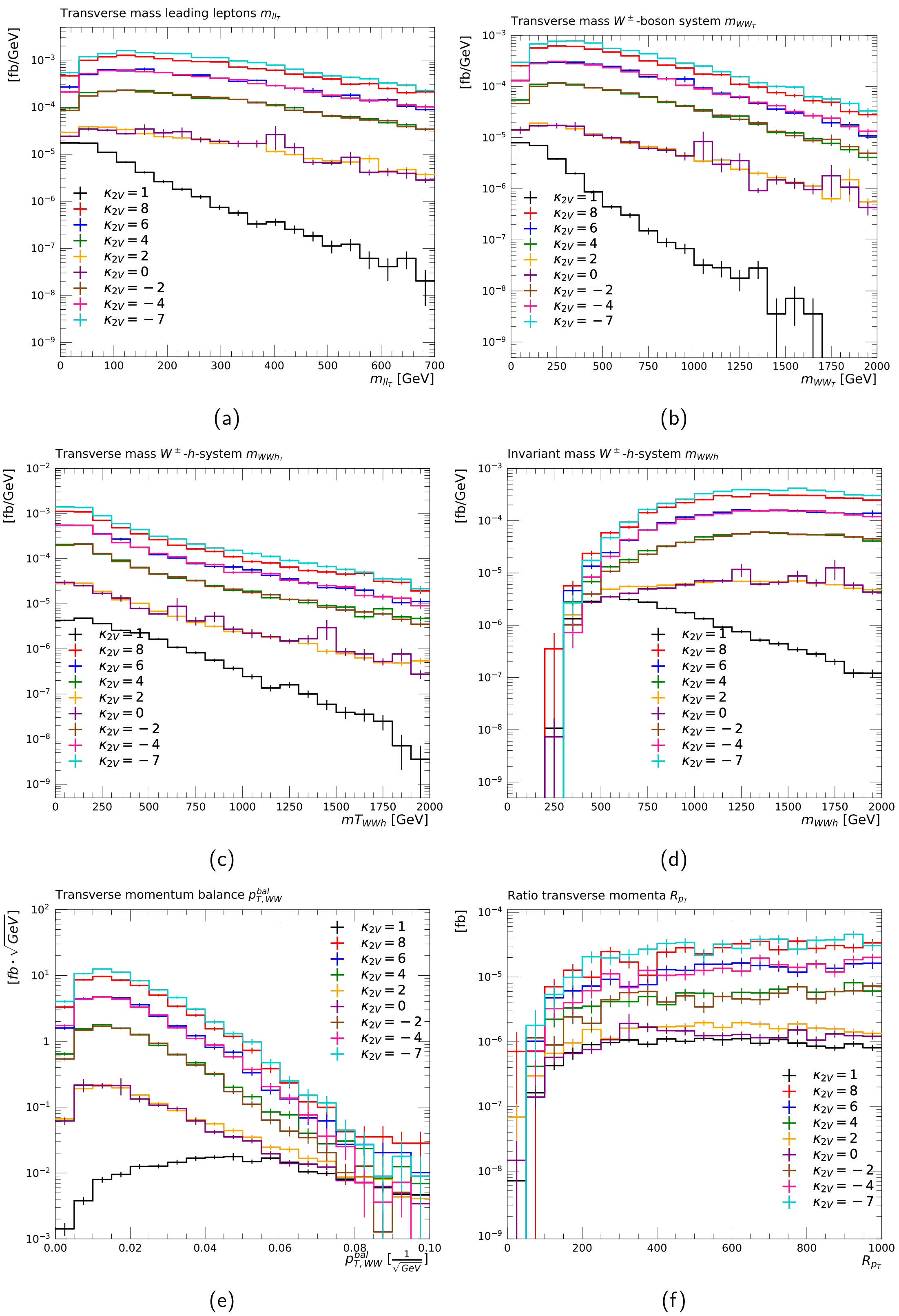

Abbildung 5.7: Plots for the sensitive observables a)Transverse mass of leading leptons $\mathrm{m_{ll_T}}$, b) Transverse mass of $\mathrm{W^{\pm}}$-boson system $\mathrm{m_{WW_T}}$ c) Transverse mass of $\mathrm{W^{\pm} - h}$-boson system $\mathrm{m_{WWh_T}}$, d) Invariant mass of $\mathrm{W^{\pm}}$–h system $\mathrm{m_{WWh}}$, e) Transverse momentum balance $\mathrm{p^{bal}_{T,WW}}$ and f) Ratio of transverse momenta $\mathrm{R_{p_T}}$ through varying values of κ_{2V} in Sherpa event samples.

All observables left to discuss, so $\mathrm{m_{WWh_T}}$, $\mathrm{m_{ll_T}}$, $\mathrm{m_{WW_T}}$ and $\mathrm{m_{WWh}}$ show visible deviations in the Standard Model limit when comparing the Sherpa and Madgraph samples, as being shown in figure 5.8. The difference for higher energies in $\mathrm{m_{ll_T}}$ can be caused by the selector cut option in Madgraph that allows to apply a cut on the leptons in the prompt final state, which is not possible in Sherpa. This can even influence the $\mathrm{W^{\pm}}$-bosons, since, as the leptons are decay products of the $\mathrm{W^{\pm}}$-bosons, their kinematic properties are connected. This becomes even more apparent when comparing the plots of $\mathrm{m_{WW_T}}$ and $\mathrm{m_{WWh_T}}$. Where both histograms for the Sherpa and Madgraph samples act mostly similar in the $\mathrm{m_{WWh_T}}$-plot (except for higher energies), this is not the case for the $\mathrm{m_{WW_T}}$-plot. For the Madgraph plot, the distribution drops down after the second bin by almost two orders of magnitude, which seems like there is a cut applied which to some extend influences the distribution of the transverse $\mathrm{W^{\pm}}$-boson mass. The influence of the selector cut option in the Madgraph samples will be investigated in the following chapter.

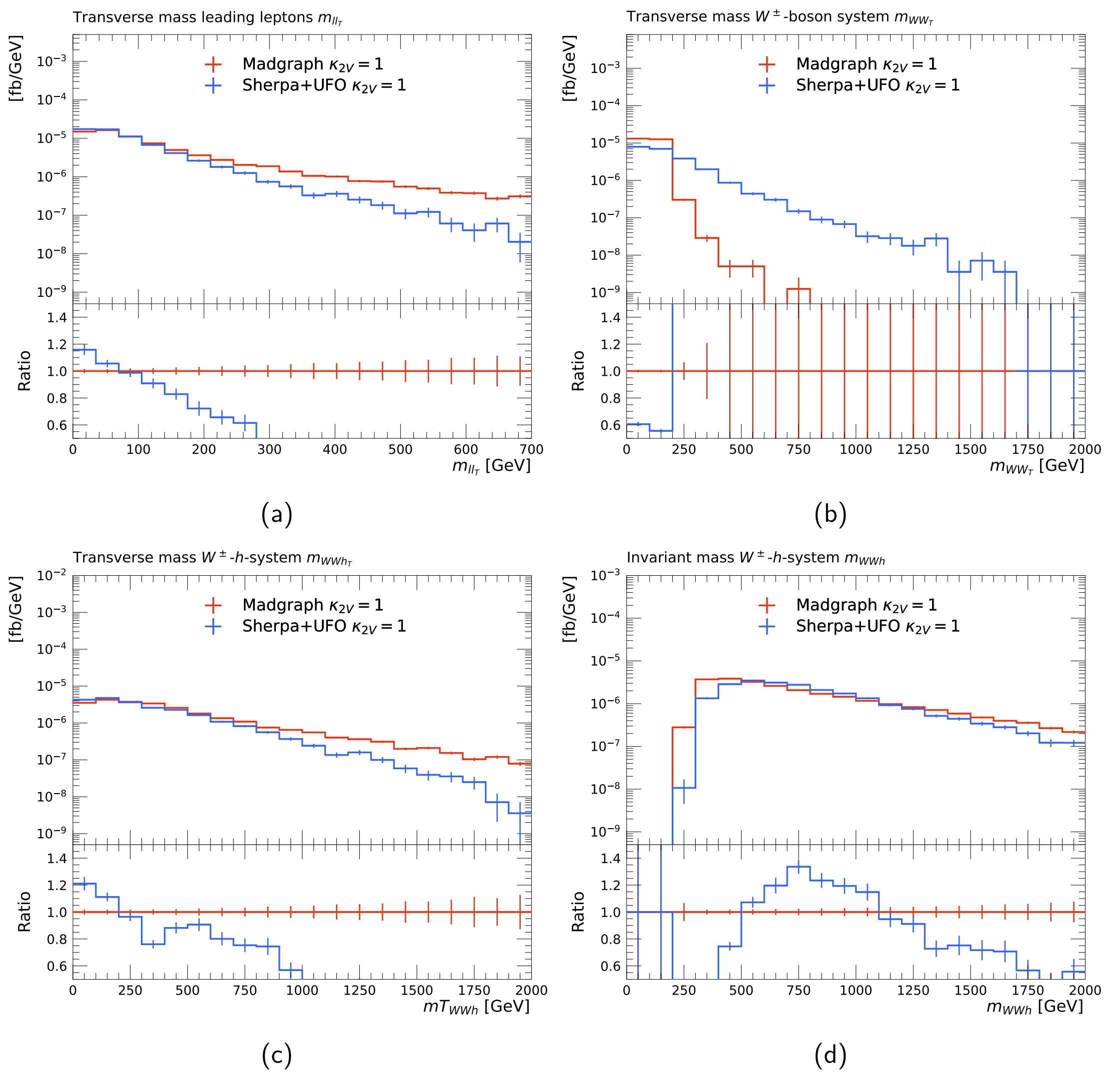

Abbildung 5.8: Comparison of the observables a) $\mathrm{m_{ll_T}}$, b) $\mathrm{m_{WW_T}}$, c) $\mathrm{m_{WWh_T}}$ and d) $\mathrm{m_{WWh}}$ in the Standard Model limit of Madgraph and Sherpa samples.

When analyzing the single plots for every value of κ_{2V}, the most obvious deviations take place for the Standard Model case. For the beyond Standard Model plots the differences in histograms are mostly not following a recognizable pattern. The single plots of the $\mathrm{m_{WW_T}}$ observable are an exception from that, since for all of the κ_{2V} values the results linked to the Sherpa samples are starting at a higher differential cross-section for lower energies and after a few bins they drop below the results from the Madgraph samples. All of the single plots of $\mathrm{m_{WW_T}}$ can be seen in figure 5.9 and the not further discussed single plots for the other observables are shown in the appendix.

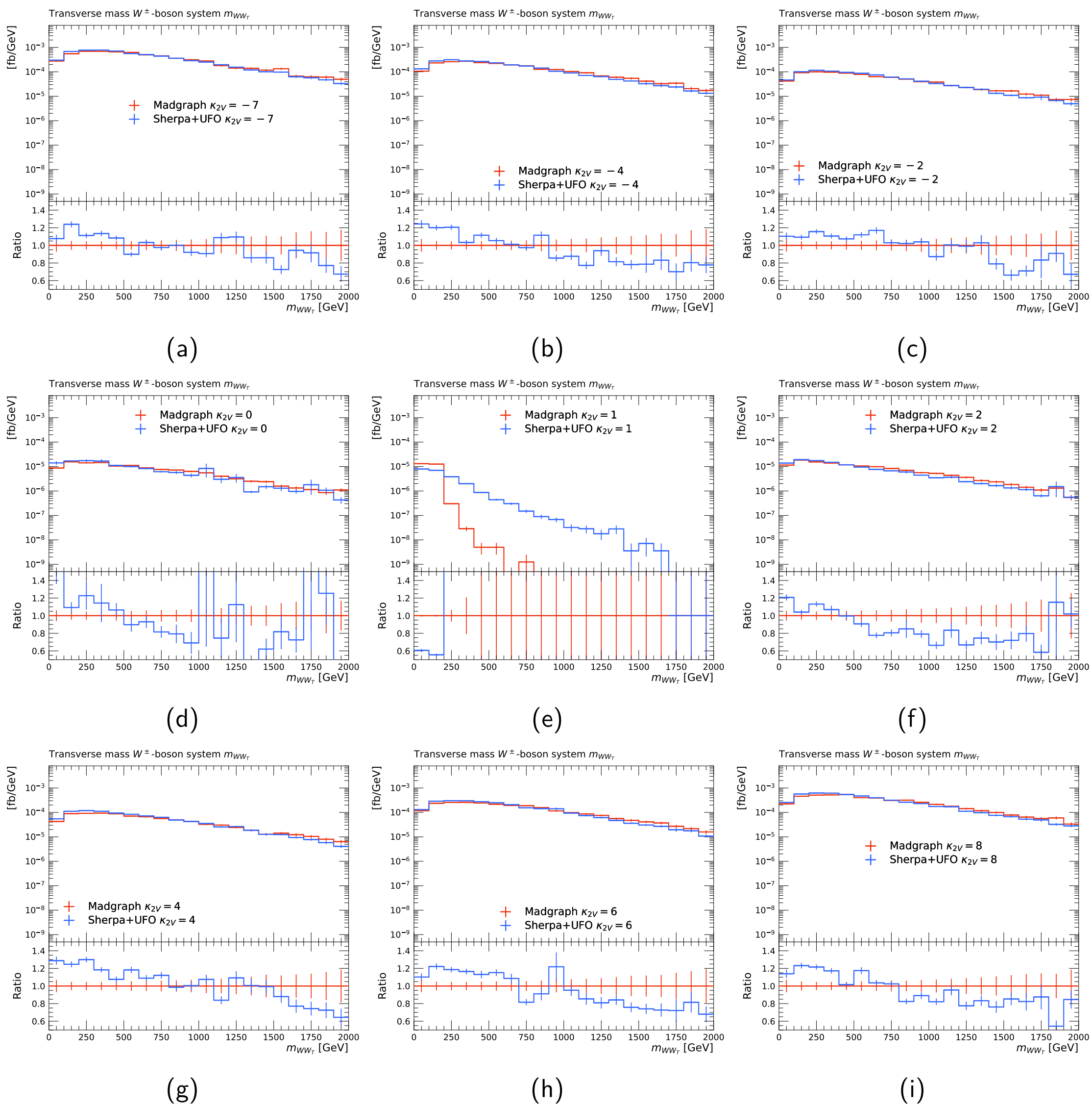

Abbildung 5.9: A comparison of the Madgraph and Sherpa samples regarding the $\mathrm{m_{WW_T}}$ observable for all values of $\kappa_{2\mathrm{V}}$ used in the Analysis.

5.3.3 Standard Model Validation with Madgraph Generation Level Cuts

To see if the angular selector cut settings only used in the Madgraph event generation, $\Delta\mathrm{R_{jj}} > 0.4, \Delta\mathrm{R_{ll}} > 0.2$ and $\Delta\mathrm{R_{lj}} > 0.2$, cause the visible differences between the Madgraph and Sherpa samples, the Rivet analysis will be extended by these cuts. Furthermore a new Sherpa event sample is generated, that will share at least the generation level cuts, existent in Madgraph, on the jets, being $\mathrm{p_T} > 10\,\mathrm{GeV}$, $\eta < 5.5$ and $\Delta\mathrm{R_{jj}} > 0.4$. To also match the sample size of the Madgraph Standard Model sample, a total of 100000 unweighted events were generated with Sherpa. The effects of each of these cuts in the Standard Model case is shown in a cut flow diagram, comparing all of the influences on the total cross-section of the samples. For the application of the generator level cuts in Madgraph, it is important to take into account, that there a jet j is defined with all light leptons, including the b-quark. Therefore, since particles created in the hard decay are also influenced by the generator level cuts in madgraph, these cuts must also be applied to the b-jets, resulting from the decay of the Higgs-boson. The effect of all the additional angular cuts can be seen in figure 5.10.

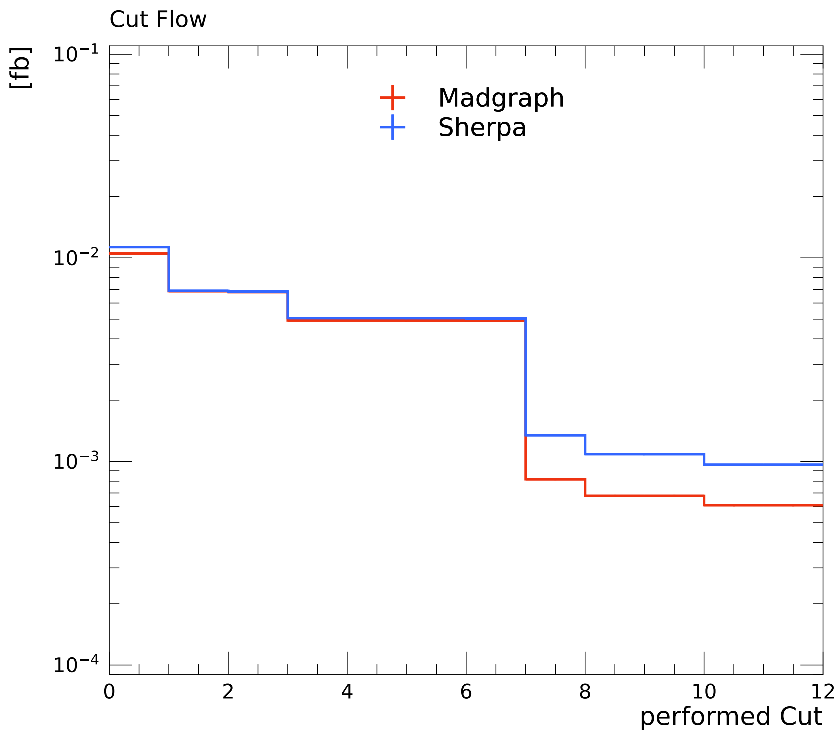

Abbildung 5.10: Diagram of the total cross-section being influenced by each applied cut. The additional angular cuts appear right to the bin edges 5.) $\Delta\mathrm{R_{jj}} > 0.4$, 6.) $\Delta\mathrm{R_{ll}} > 0.2$ and 7.) $\Delta\mathrm{R_{lj}} > 0.2$. The other cuts before and after these are the same as defined in section 5.3.1.

Surprisingly, the generator level cuts heavily influence both, the Sherpa and the Madgraph samples. This could result from the fact that Madgraph, when using these generator level cuts, addresses only singular quarks and not jets, since Madgraph on its own is no capable of simulating a particle shower. Since a jet is not a one-dimensional trajectory, but expands over a larger volume in a conic structure, it might interfere with a lepton's path that would otherwise be easily resolvable from it.

To get an overview on how these cuts influence the event samples, the observables $\Delta\eta_{\mathrm{jj}}$ and $\mathrm{m_{jj}}$ are plotted with the applied angular cuts. The cuts cause a crucial change in the distributions of representing both samples. For the $\Delta\eta_{\mathrm{jj}}$ observable, the histogram connected to the Sherpa sample is now much flatter instead of the clear maximum at around $\Delta\eta_{\mathrm{jj}} = 0$. Also it hints now two minima in the distribution, that are way more pronounced in the histogram linked to the Madgraph sample. The variation for the $\mathrm{m_{jj}}$ observable is directly apparent for the Madgraph sample plot, since it looks like noticeably fewer events land in the former area the distributions maximum was located in. The effects in the Sherpa samples are way more subtile, where the maximum of the distribution is slightly flattened and shifted more to higher energies. The cut flow in Ref. 5.10 allows to attribute all the major changes in the distributions for $\Delta\eta_{\mathrm{jj}}$ and $\mathrm{m_{jj}}$ to the lack of events where jets and leptons are spatially close.

After all, the application of these cuts do not provide an explanation for the differences in the distributions of the aforementioned sensitive observables, created with the Sherpa and Madgraph samples.

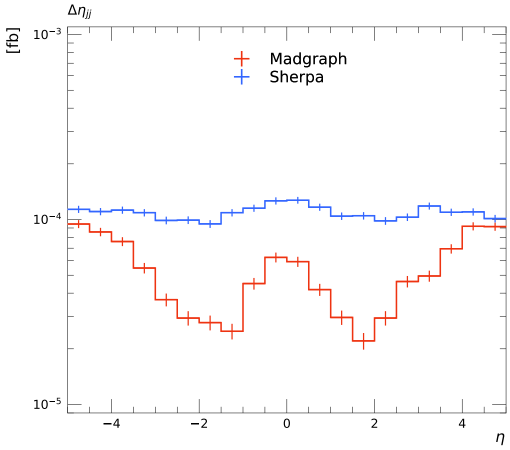

(a)

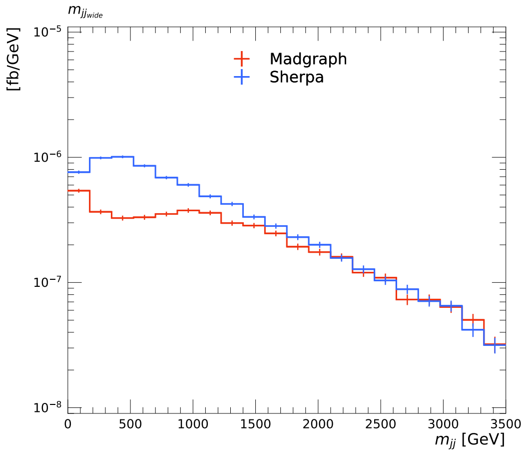

(b)

Abbildung 5.11: The histograms for the observables $\Delta\eta_{\mathrm{jj}}$ and $\mathrm{m_{jj}}$ after the generation level cuts have been applied to the Madgraph and Sherpa samples at analysis level.

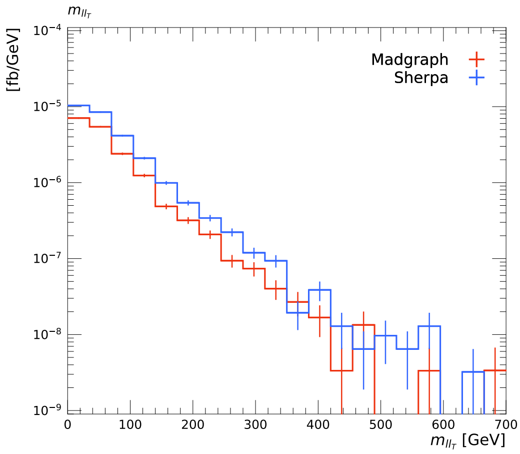

(a)

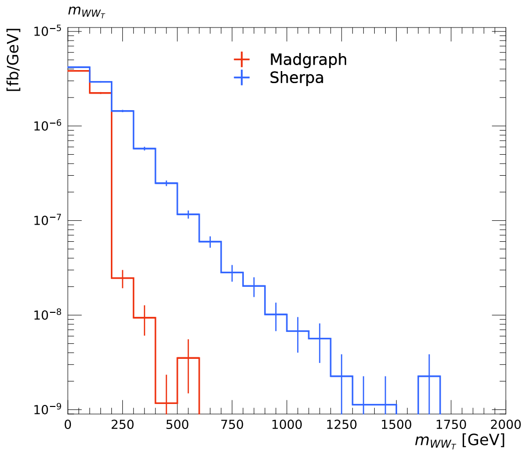

(b)

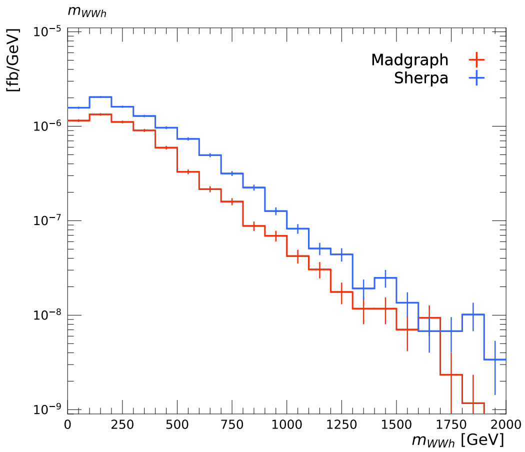

(c)

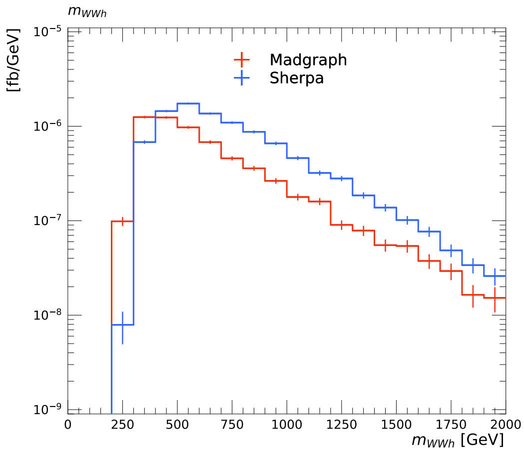

(d)

Abbildung 5.12: Comparison of the observables a) $\mathrm{m_{ll_T}}$, b) $\mathrm{m_{WW_T}}$, c) $\mathrm{m_{WWh_T}}$ and d) $\mathrm{m_{WWh}}$ in the Standard Model limit of Madgraph and Sherpa samples with the addition of the application of the angular generation level cuts.

5.4 Check of DNN-Observables

The goal of this section is to investigate the observables specified in the ATLAS note [13] in terms of sensitivity and to observe their behavior under changing values of the $\kappa_{2\mathrm{V}}$-parameter to train a Deep Neural Network (DNN) to distinguish experimental data generated with beyond Standard Model values of $\kappa_{2\mathrm{V}}$ from Standard Model samples. In the following section their will be brief comments on any changes in the histograms of the observables when varying $\kappa_{2\mathrm{V}}$ and based on that a study on differences of the representations of the Madgraph and Sherpa event samples.

5.4.1 Non-sensitive Observables

The observables showing the least sensitivity of all are the ones related to the angle Φ, which is the case for the leptons and the Higgs-jets. The plots of the Φ related observables are mainly influenced by an increase in cross-section, which means that it is simply showing an offset along the y-axis without altering the shape of the plot at all. The histograms describing the Φ distribution of the Higgs-jets and the leptons are evenly distributed at all angles and for all tested values of $\kappa_{2\mathrm{V}}$. The even distribution for this observable can be explained through the azimuthal symmertry of the colider. Since there is also no difference comparing the Madgraph and Sherpa samples, these observables will not be further discussed. To provide an overview to the reader, the plots concerning Φ_{hj_1} and Φ_{l_1}, will be shown in the following figures.

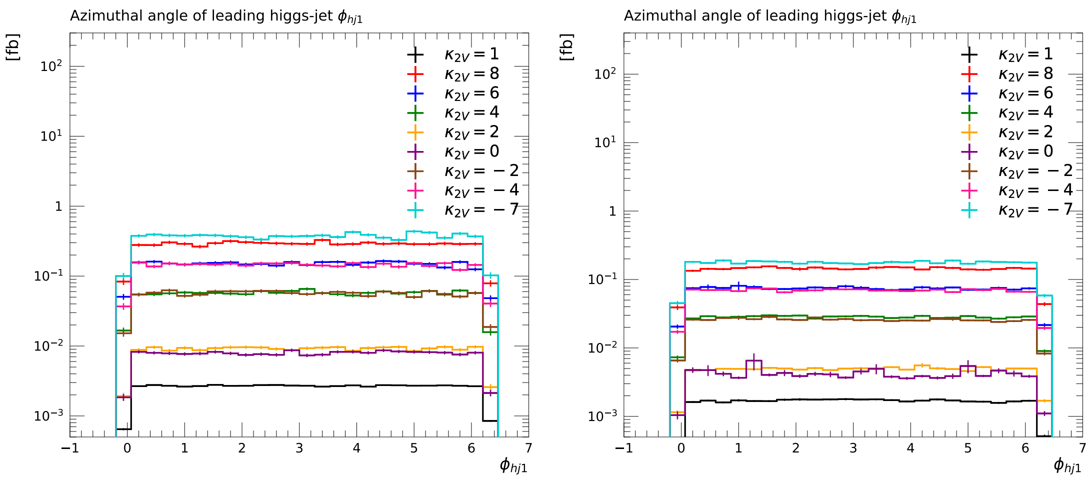

(a) (b)

Abbildung 5.13: Distributions of azimuthal angle Φ of the leading Higgs-jet for varying values of $\kappa_{2\mathrm{V}}$ for the a) Madgraph and b) Sherpa samples.

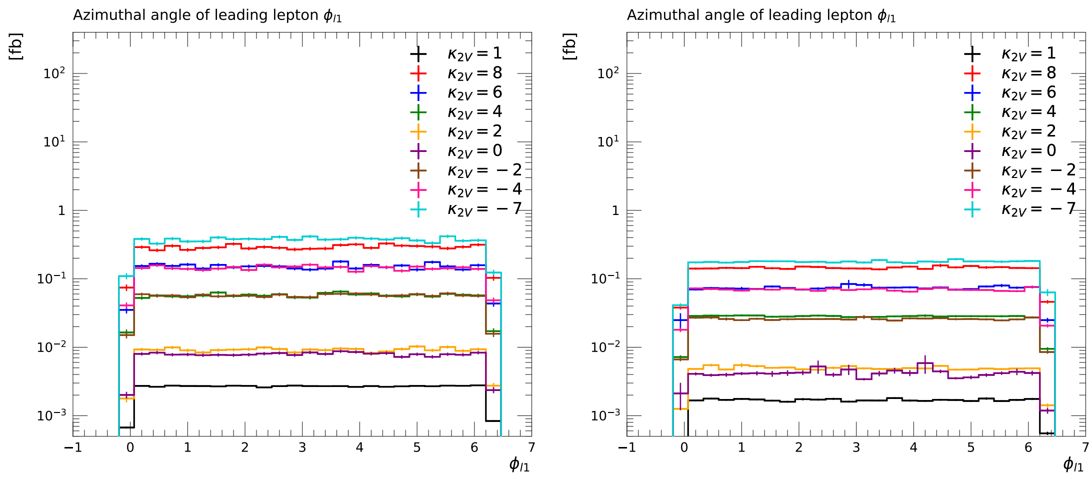

(a) (b)

Abbildung 5.14: Distributions of azimuthal angle Φ of the leading lepton for varying values of $\kappa_{2\mathrm{V}}$ for the a) Madgraph and b) Sherpa samples.

5.4.2 Sensitive Observables and Validation of Madgraph and Sherpa Event Samples

When investigating the observable η, a difference becomes apparent when comparing the Standard Model to the beyond Standard Model case. The maximum of the plot flattens for $\kappa_{2\mathrm{V}} = 1$ and gets more pronounced $\kappa_{2\mathrm{V}}$ deviates from it. So with an increase in deviation of $\kappa_{2\mathrm{V}}$, more events with a more central pseudorapidity η can be measured. Corresponding to this, it can be seen that the distributions for the hadronic and leptonic transverse momenta become harder the further $\kappa_{2\mathrm{V}}$ departures from the Standard Model. The reason for this is, that with an higher deviatios in $\{\kappa_{2\mathrm{V}}$ the coupling of $\mathrm{W}^{\pm}$-bosons and the Higgs-boson gets favored, which encourages the contribution of Feynman diagrams containing a virtual Higgs. Through the additional heavy boson, the $\mathrm{W}^{\pm}$-bosons and the h-boson in the prompt final state decay almost at rest, leading to large angles in their decay products. To provide an idea of the behavior of the investigated observables for all the values of $\kappa_{2\mathrm{V}}$, all of them shall be shown in the following. Since the general behavior of the observables is similar for both event sample types, it is sufficient to show the plots generated from one sample set, in this case Sherpa.

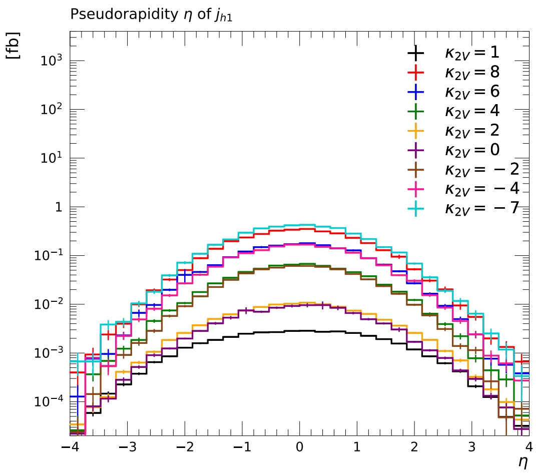

(a)

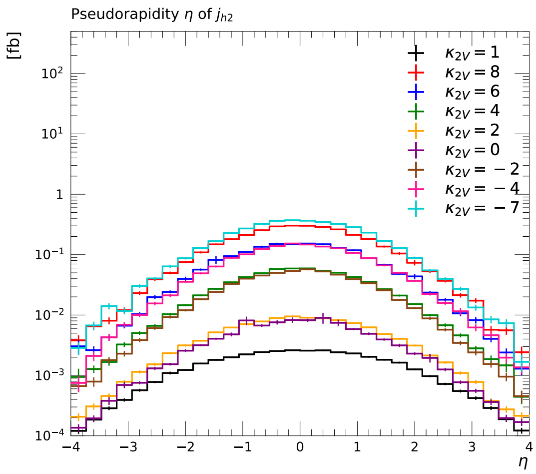

(b)

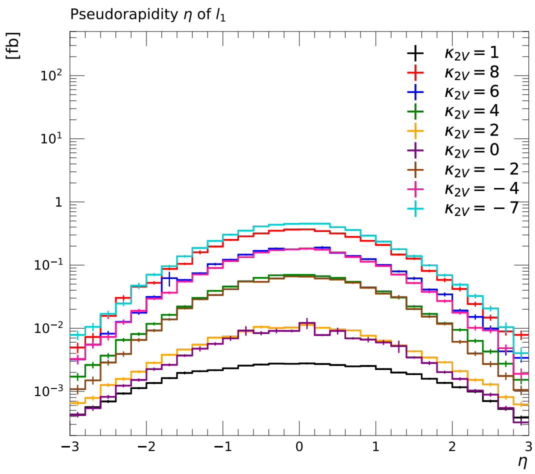

(c)

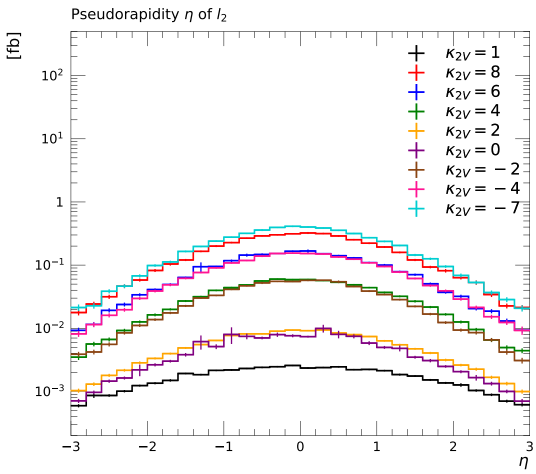

(d)

Abbildung 5.15: Distributions of pseudorapidity η of the leading and sub-leading Higgs-jet and the leading and sub-leading leptons for varying values of $\kappa_{2\mathrm{V}}$ for the Sherpa samples.

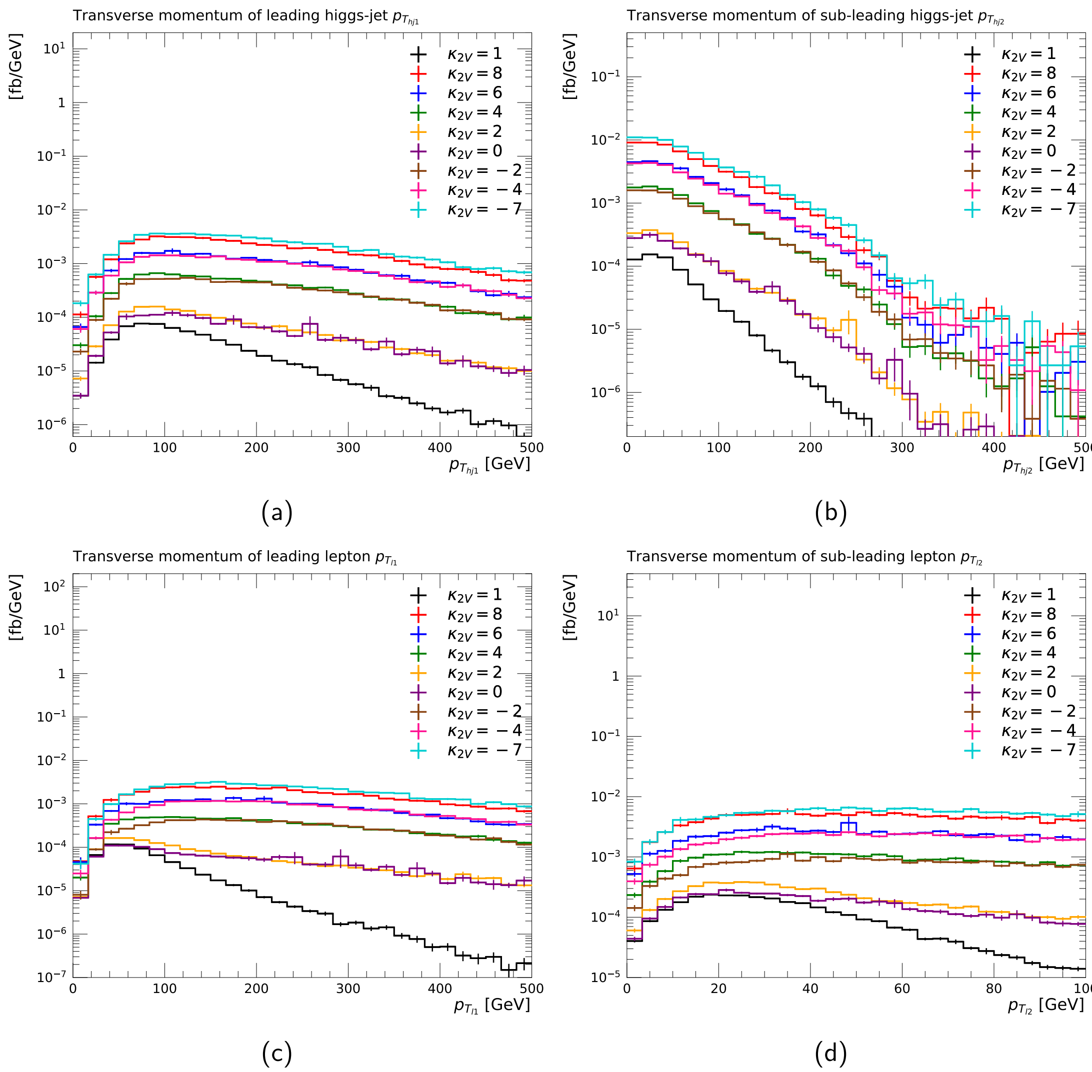

Abbildung 5.16: Distributions of the transverse momentuma $\mathrm{p_T}$ of the leading and sub-leading Higgs-jet and the leading and sub-leading leptons for varying values of $\kappa_{2\mathrm{V}}$ for the Sherpa samples.

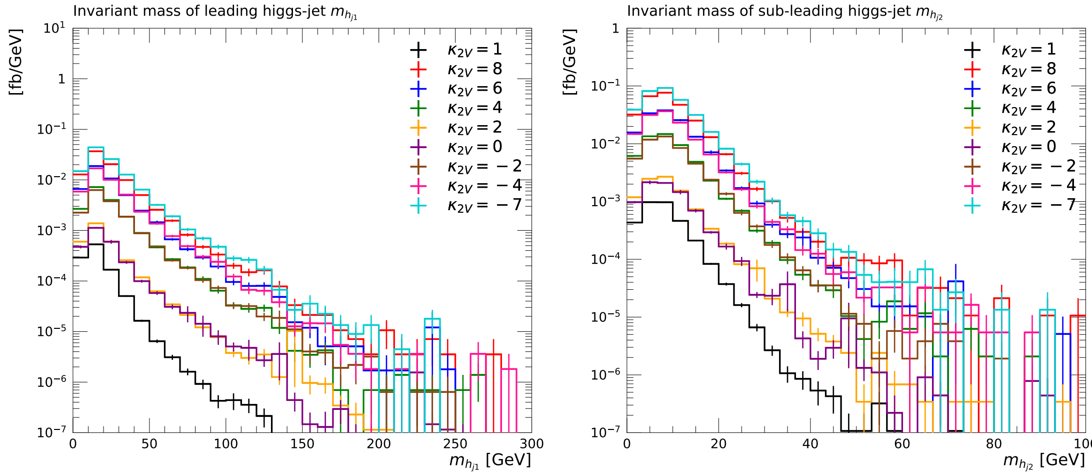

(a) (b)

Abbildung 5.17: Distributions of the invariant masses $\mathrm{m_{hj}}$ of the leading and sub-leading Higgs-jets for varying values of $\kappa_{2\mathrm{V}}$ for the Sherpa samples.

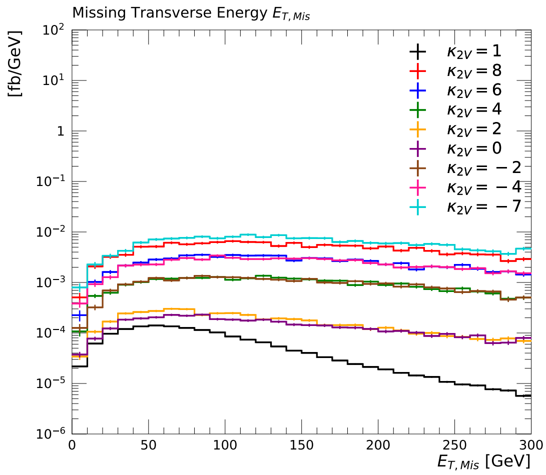

Abbildung 5.18: Distributions of missing transverse energy $\mathrm{E_{T,Miss}}$ for varying values of $\kappa_{2\mathrm{V}}$ for the Sherpa samples.

The validation analysis regarding the samples from both, Madgraph and Sherpa, already show deviations in the histograms for the transverse momenta, the missing transverse energy and the invariant mass of the Higgs jets. In the following, in every plot that compares single Madgraph and Sherpa samples with each another, the Madgraph histogram gets scales by the ratio $\frac{\sigma_{\text{Sherpa}}}{\sigma_{\text{Madgraph}} \cdot \text{BR}(\text{h} \to \text{b}\bar{\text{b}})}$ specified in the table 5.2, to emphasize differences in shapes between both plots. When considering the ratioplots, the general tendency seems to be, that the distributions linked to the Sherpa samples peak at lower energies and fall of quicker for higher energies than the plot from the Madgraph sample.

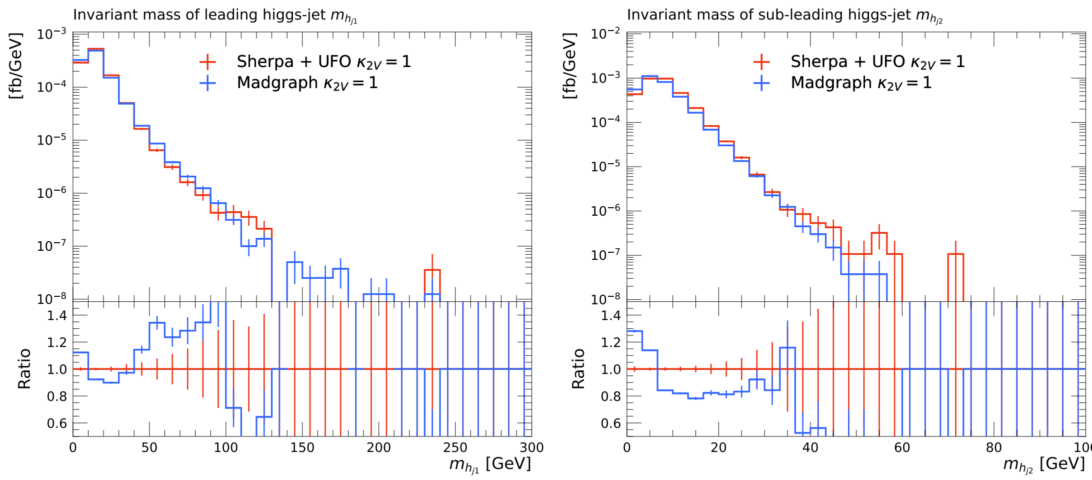

(a) (b)

Abbildung 5.19: Comparison plots of the invariant mass $\mathrm{m_{hj}}$ for the leading and sub-leading Higgs-jets for the Madgraph and Sherpa samples in the Standard Model limit.

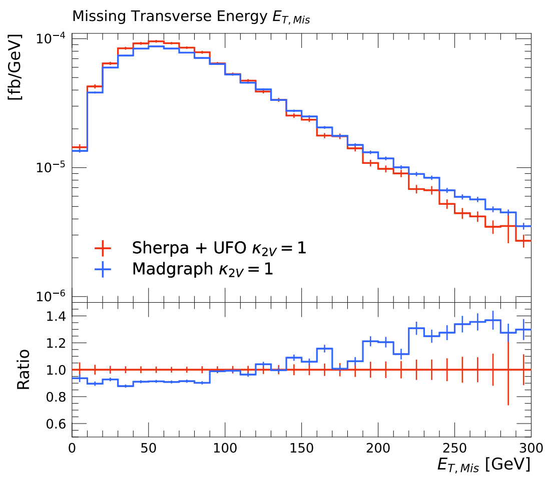

Abbildung 5.20: Comparison plots of the missing transverse energy $\mathrm{E_{T,Miss}}$ for the Madgraph and Sherpa samples in the Standard Model limit.

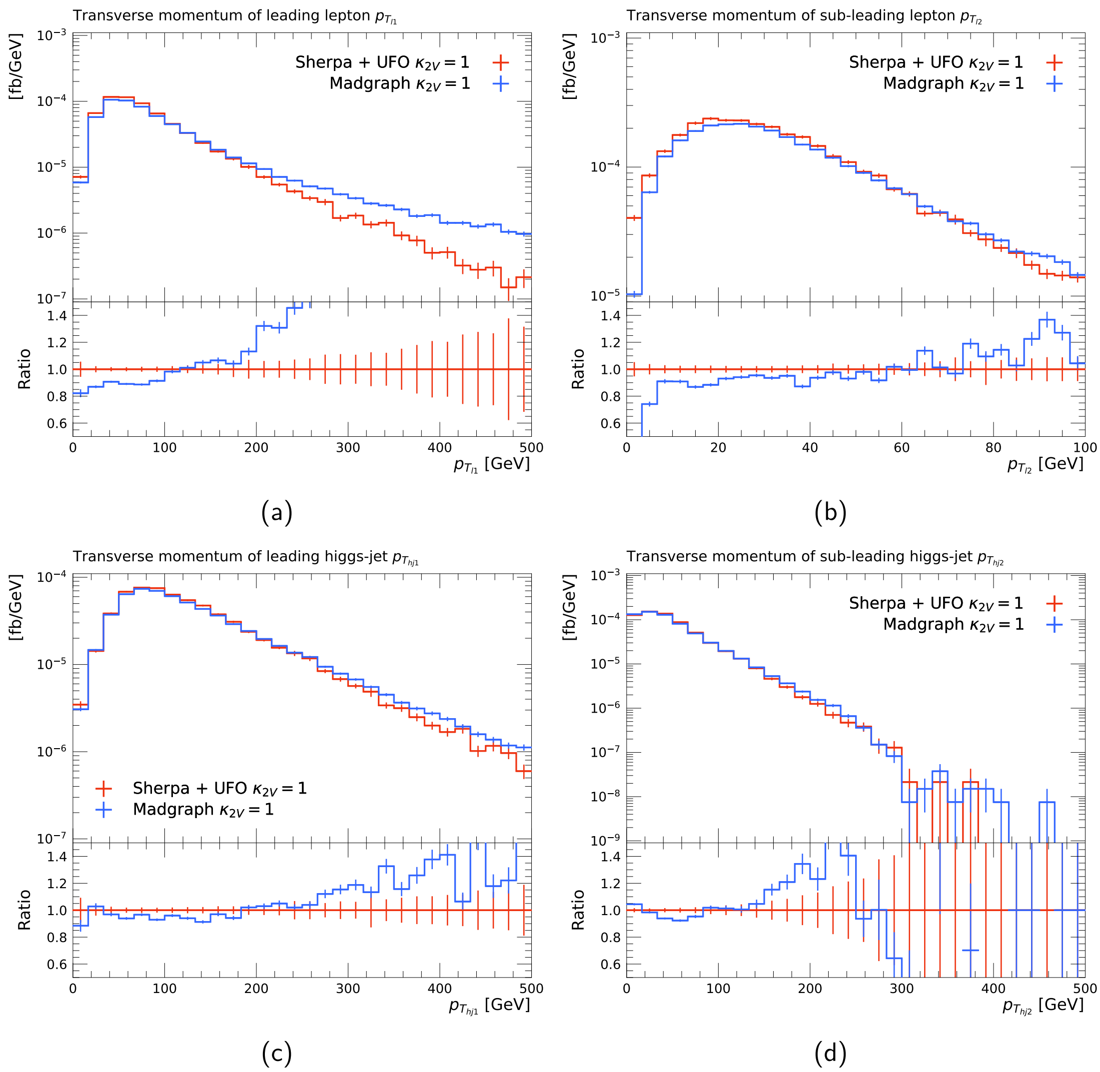

Abbildung 5.21: Comparison plots of the transverse momenta $\mathrm{p_T}$ for the leading and sub-leading Higgs-jets and leptons for the Madgraph and Sherpa samples in the Standard Model limit.

In almost all representations of the observables, the deviation beween Sherpa and Madgraph become most pronounced in the Standard Model limit. For values of κ_{2V} that deviate further from the Standard Model value, the differences between Madgraph and Sherpa can even become less apparent. The Observable with the most visible difference between Madgraph and Sherpa, that persist for every value of κ_{2V} chosen here, is $\mathrm{m_{hj_2}}$. As an example it will be shown for every κ_{2V} setting.

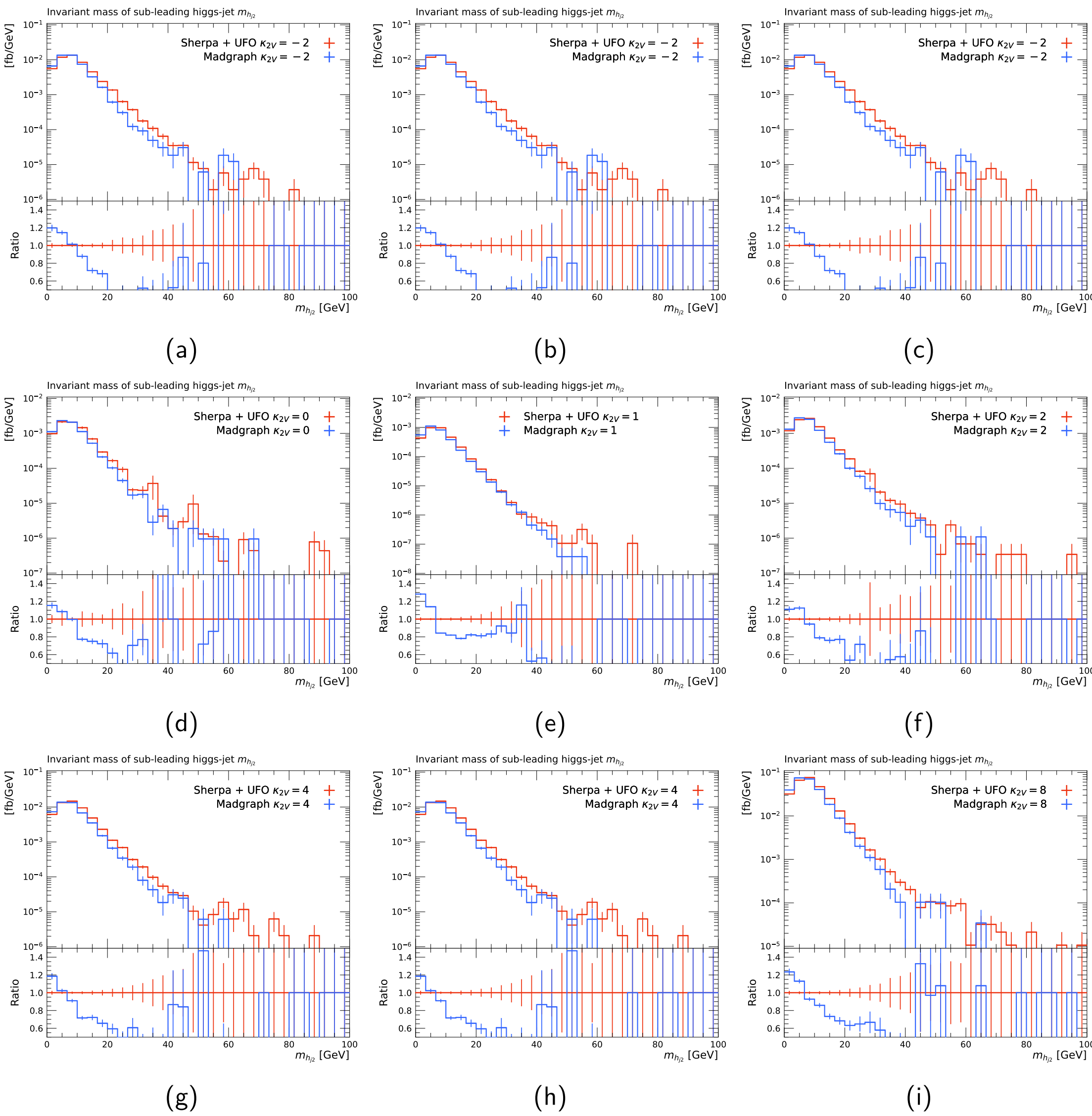

Abbildung 5.22: Comparisons of Madgraph and Sherpa samples for all the κ_{2V} settings regarding the observable $\mathrm{m_{hj_2}}$.

5.5 Variation of κ_{2V} at $100\,\mathrm{TeV}$ Center-of-Mass Energy

This section shall provide a first insight on the influence of varying values of κ_{2V} in regions of high center-of-mass energies.

The $100\,\mathrm{TeV}$ samples were generated with Sherpa3.0.1 and use mostly the same setting as specified in chapter 4 with only some minor extensions. Besides from obviously switching the beam energy setting from $13\,\mathrm{TeV}$ to $100\,\mathrm{TeV}$, there are also some adaptations in the selector cuts. The events are now generated with two additional FastjetSelectors being implemented, where one is granting that the invariant mass of the leading jets $\mathrm{m_{jj}}$ is equal or higher than $1.2\,\mathrm{TeV}$ and that the absolute

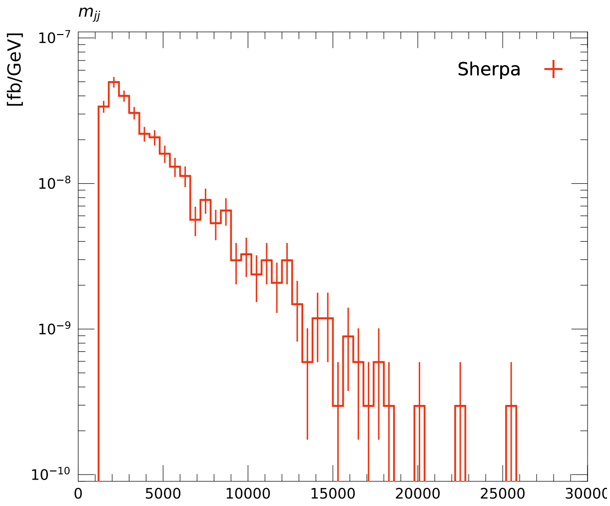

Abbildung 5.23: Invariant mass $\mathrm{m_{jj}}$ of two leading jets at 100 TeV center-of-mass energy. $\mathrm{m_{jj}}$ is shown in units of $[\mathrm{GeV}]$.

difference in pseudorapidity $\Delta\eta_{\mathrm{jj}}$ is bigger than 4.5. These selectors are more powerful than the single particles on their own, because when a cut on the Particle container 93 is set, it applies to all the separate quarks contained in it, without the context of a jet. With the FastjetSelector, the partons are already reconstructed in the event generation and evaluated as a jet and vetoed, if they do not fulfill the specified cuts.

Further cuts on the analysis side are chosen as in [18], even though they are simplified in some cases. The cuts are

1. Number of leptons $\stackrel{!}{=} 2$, same-sign leptons, $\Delta\mathrm{R_{ll}} \leq 0.4$.
2. More than 4 jets with $\mathrm{p_T} \geq 25\,\mathrm{GeV}$, ≥ 2 b-tagged jets with $\left|\eta_{\mathrm{jj}}\right| < 2.5$, ≥ 2 leading light jets with $\left|\eta_{\mathrm{jj}}\right| < 4.7$.
3. $\mathrm{E_{T,miss}} < 30\,\mathrm{GeV}$
4. Invariant mass of leptons $\mathrm{m_{ll}} \leq 50\,\mathrm{GeV}$
5. Invariant mass of b-tagged jets does not deviate further than $|\mathrm{m_{bb}} - \mathrm{m_h}| > 20\,\mathrm{GeV}$
6. $\left|\eta_{\mathrm{jj}}\right| \leq 5.0$ and $\mathrm{m_{jj}} \leq 1.5\,\mathrm{TeV}$

One Standard Model sample with the standard Sherpa setup was used to generate 100000 events. For the case of Sherpa implemented with the HHVBF_UFO-model, there were 30000 evens generated for each $\kappa_{2\mathrm{V}}$. The cross-sections listed in tab. 5.3 have been read directly from the Sherpa output. An analysis of the plotted data was planned, but could not be realized within the time of this thesis.

Value κ_{2V}	total σ_{Sherpa} [pb]
1	0,000022 $\pm 1,538 \cdot 10^{-6}$
8	0,003991 $\pm 7.710 \cdot 10^{-5}$
6	0,002027 $\pm 2,321 \cdot 10^{-5}$
4	0,000738 $\pm 6,239 \cdot 10^{-6}$
2	0,000107 $\pm 1,481 \cdot 10^{-6}$
0	0,000101 $\pm 2.056 \cdot 10^{-6}$
-2	0,000719 $\pm 8,312 \cdot 10^{-6}$
-4	0,001902 $\pm 2,894 \cdot 10^{-5}$
-7	0,006942 $\pm 8,203 \cdot 10^{-5}$

Tabelle 5.3: Total cross-sections of the event samples created with Sherpa for $100\,\text{TeV}$ center-of-mass energy.

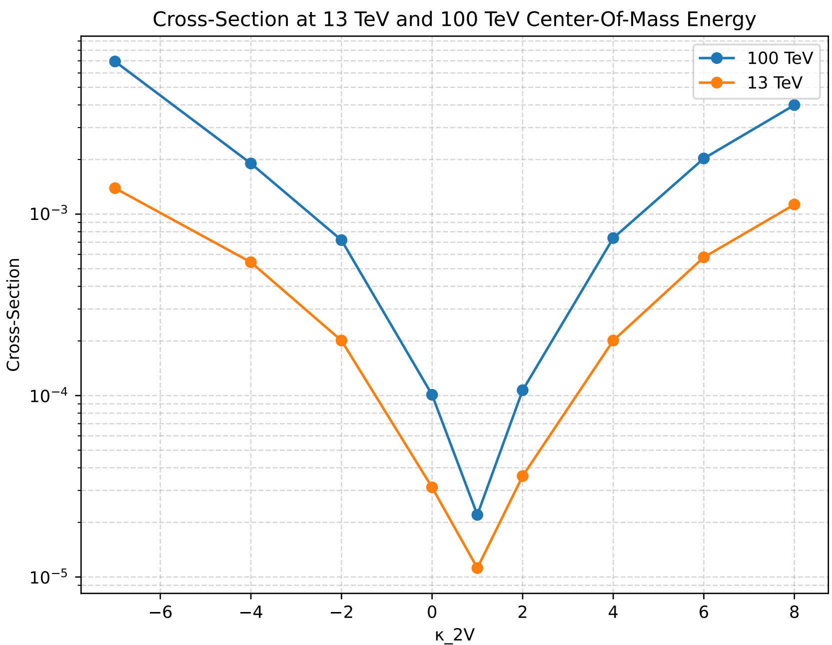

Abbildung 5.24: Comparison of cross-sections resulting from samples at $13\,\text{TeV}$ and $100\,\text{TeV}$ for varying values of κ_{2V}.

6 Conclusion and Outlook

The results of the validation for the Sherpa and Madgraph samples agree in some instances but also show strong deviations at times. When considering the total cross-sections that are calculated for both event generators in the Standard Model limit, they both match comparably well. Variations start to show up when regarding beyond Standard Model values of $\kappa_{2\mathrm{V}}$. Not only does the total cross-section increase the further it deviates from the Standard Model value, which confirms the behavior of the total cross-section shown in Ref. [13]. There is also a certain offset in ratio for the total cross-sections of both sample types established, that becomes constant for large deviations of $\kappa_{2\mathrm{V}}$.

For the analysis of the observables used in the deep neural network, it became apparent that the observables $\Phi_{\mathrm{l}_1}, \Phi_{\mathrm{l}_2}, \Phi_{\mathrm{hj}_1}$ and Φ_{hj_2} do not show any sensitivity to the variation of the $\kappa_{2\mathrm{V}}$-parameter. Some effect could be seen, when regarding the switch from Standard Model to beyond Standard Model, in the pseudorapidities η_{l_1}, η_{l_2}, η_{hj_1} and η_{hj_2}. All observables concerning the hadronic or leptonic transverse momenta $\mathrm{p_T}$, the invariant mass of the Higgs-jets or the missing transverse energy $\mathrm{E_{T,Miss}}$ could be identified to be influenced in shape by the varying values of $\kappa_{2\mathrm{V}}$. In the Standard Model limit of both sample types, there are already recognizable differences within the sensitive observables, most prominently the observables $\mathrm{p_{T_{l1}}}$. For the varying values of $\kappa_{2\mathrm{V}}$, especially the further it deviates from the Standard Model value, the more difficult it gets to read meaningful information from the plot. The ambiguity in the plot can be caused by the comparably small sample sizes. Another approach to explain is, that the beyond Standard Model contributions in the HHVBF_UFO-model overpower the Standard Model ones for larger deviations of $\kappa_{2\mathrm{V}}$. Since this is performed similarly in Sherpa and Madgraph that might be a reason how the initially different Standard Model contributions are evened out.

When investigating the sensitive observables connected to signature elements of the signal process, there were major differences between the results from the Sherpa and Madgraph samples, especially when considering the $\mathrm{m_{WW_T}}$ observable. The exact reason for the deviations could not be found within this thesis, however, it could be disproven, that it is connected to the generation level cuts implemented into the Madgraph samples. Since some of these observables are heavily linked to the subject of polarization, which was at most very superficially touch on in this thesis, one further step to take from this analysis would probably be to perform an analysis that leans more into the direction of polarization in context of the κ-framework. Another possible way to continue this study could be to move from the truth level towards a detector level analysis.

At last, there was a setup for the generation of Monte Carlo events at $100\,\mathrm{TeV}$ center-of-mass energy presented and a brief insight on the total cross-sections within the κ-framework, which behaved similar as in the $13\,\mathrm{TeV}$-case for changing values of $\kappa_{2\mathrm{V}}$. The only notable difference is the constant offset for the $100\,\mathrm{TeV}$ samples, towards higher total cross-sections. The next step in this analysis would be get a first impression common observables like transverse momentum and if there are any major differences to the $13\,\mathrm{TeV}$ center-of-mass energy case. Also the analysis cuts can be fine tuned further for the Sherpa samples, since the cuts used in this analysis are more compatible with Madgraph, which again, can use additional generation level cuts on the hard decay products.

Appendix

Quarklines for Matrix Element Calculations in HHVBF_UFO model

Process with specified quark lines	**Number of Diagrams**
• $jj \to W^+W^+hjj$:	
$u\bar{d} \to W^+W^+h \quad s\bar{c}$	360
$u\bar{s} \to W^+W^+h \quad s\bar{c}$	360
$u\bar{d} \to W^+W^+h \quad s\bar{u}$	360
$\bar{s}\bar{s} \to W^+W^+h \quad \bar{u}\bar{u}$	360
$cc \to W^+W^+h \quad ss$	360
$c\bar{d} \to W^+W^+h \quad s\bar{c}$	360
$uc \to W^+W^+h \quad ss$	360
$uc \to W^+W^+h \quad ds$	360
$c\bar{d} \to W^+W^+h \quad d\bar{u}$	360
$uu \to W^+W^+h \quad ss$	360
$cc \to W^+W^+h \quad ds$	360
$\bar{s}\bar{s} \to W^+W^+h \quad \bar{c}\bar{c}$	360
$\bar{d}\bar{d} \to W^+W^+h \quad \bar{c}\bar{c}$	360
$u\bar{s} \to W^+W^+h \quad s\bar{u}$	360
$u\bar{d} \to W^+W^+h \quad d\bar{c}$	360
$c\bar{d} \to W^+W^+h \quad s\bar{u}$	360
$\bar{d}\bar{s} \to W^+W^+h \quad \bar{c}\bar{c}$	360
$c\bar{s} \to W^+W^+h \quad s\bar{u}$	360
$\bar{s}\bar{s} \to W^+W^+h \quad \bar{u}\bar{u}$	360
$uu \to W^+W^+h \quad dd$	360
$\bar{d}\bar{d} \to W^+W^+h \quad \bar{u}\bar{u}$	360
$c\bar{d} \to W^+W^+h \quad d\bar{c}$	360
$u\bar{c} \to W^+W^+h \quad d\bar{u}$	360
$u\bar{s} \to W^+W^+h \quad d\bar{c}$	360
$uu \to W^+W^+h \quad ds$	360
$c\bar{s} \to W^+W^+h \quad s\bar{c}$	360
$\bar{d}\bar{d} \to W^+W^+h \quad \bar{u}\bar{c}$	360
$u\bar{d} \to W^+W^+h \quad d\bar{u}$	360
$uc \to W^+W^+h \quad dd$	360
$c\bar{s} \to W^+W^+h \quad d\bar{c}$	360
$c\bar{s} \to W^+W^+h \quad d\bar{u}$	360
$cc \to W^+W^+h \quad dd$	360
$d\bar{s} \to W^+W^+h \quad \bar{u}\bar{u}$	360
$\bar{d}\bar{s} \to W^+W^+h \quad \bar{u}\bar{c}$	360

Tabelle 6.1: Specific quark lines for matrix element calculation in HHVBF_UFO model for positive W-bosons.

Sensitive DNN-Observables Comparison for Sherpa and Madgraph Samples

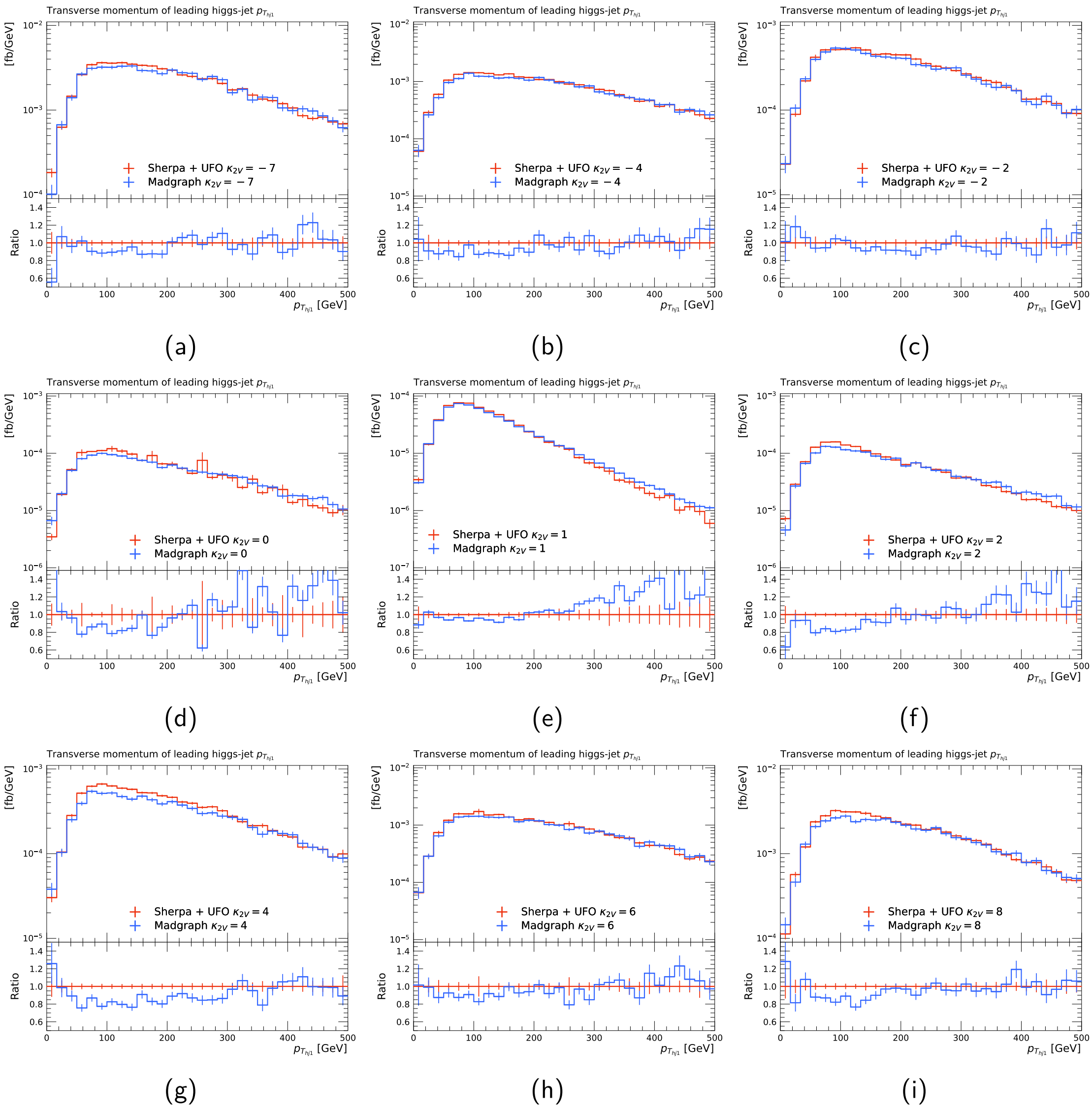

Abbildung 6.1: Comparisons of Madgraph and Sherpa samples for all the κ_{2V} settings regarding the observable p_{T,hj_1}.

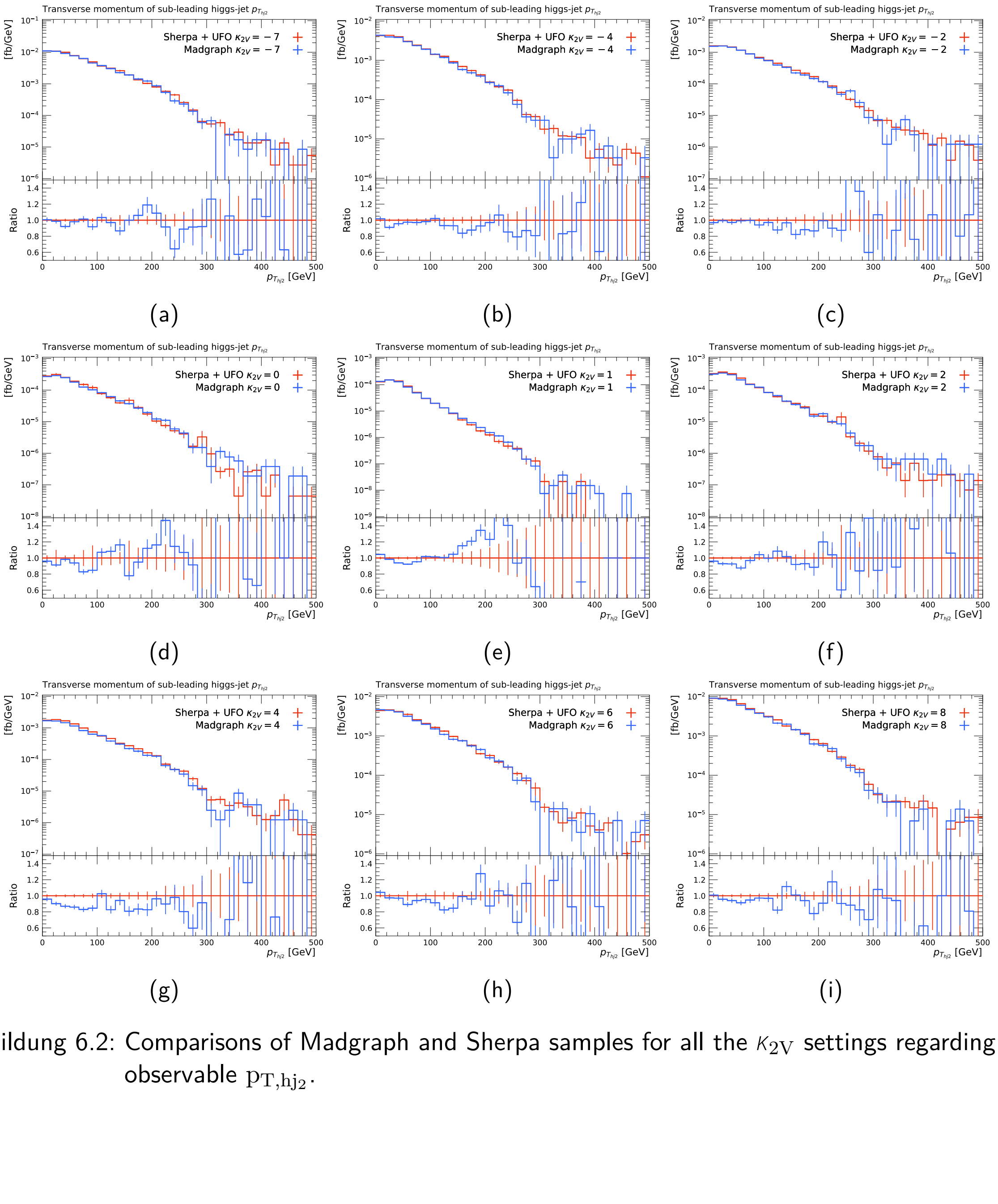

Abbildung 6.2: Comparisons of Madgraph and Sherpa samples for all the $\kappa_{2\mathrm{V}}$ settings regarding the observable $\mathrm{p_{T,hj_2}}$.

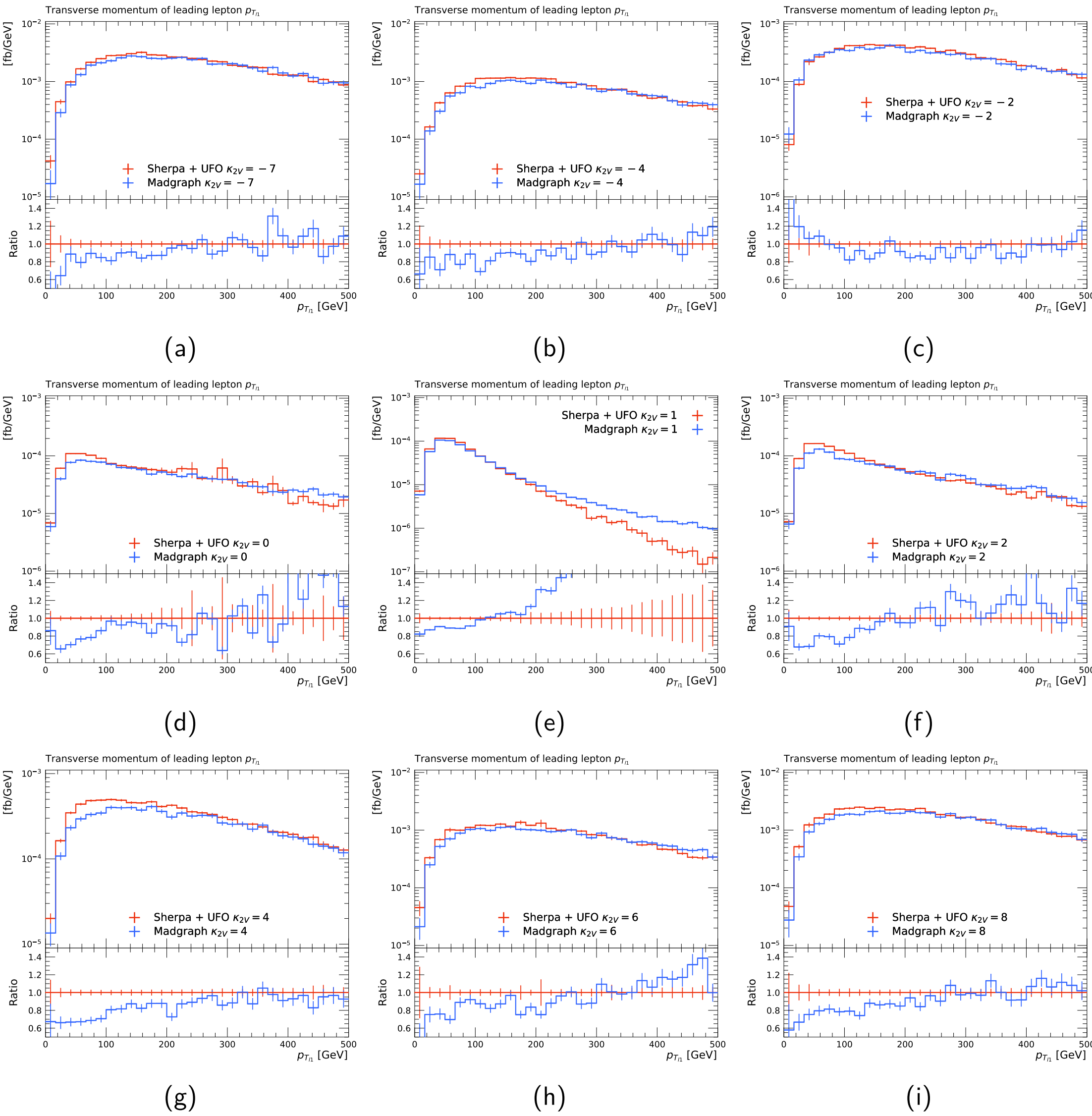

(a) (b) (c)

(d) (e) (f)

(g) (h) (i)

Abbildung 6.3: Comparisons of Madgraph and Sherpa samples for all the $\kappa_{2\mathrm{V}}$ settings regarding the observable $\mathrm{p}_{\mathrm{T},\mathrm{l}_1}$.

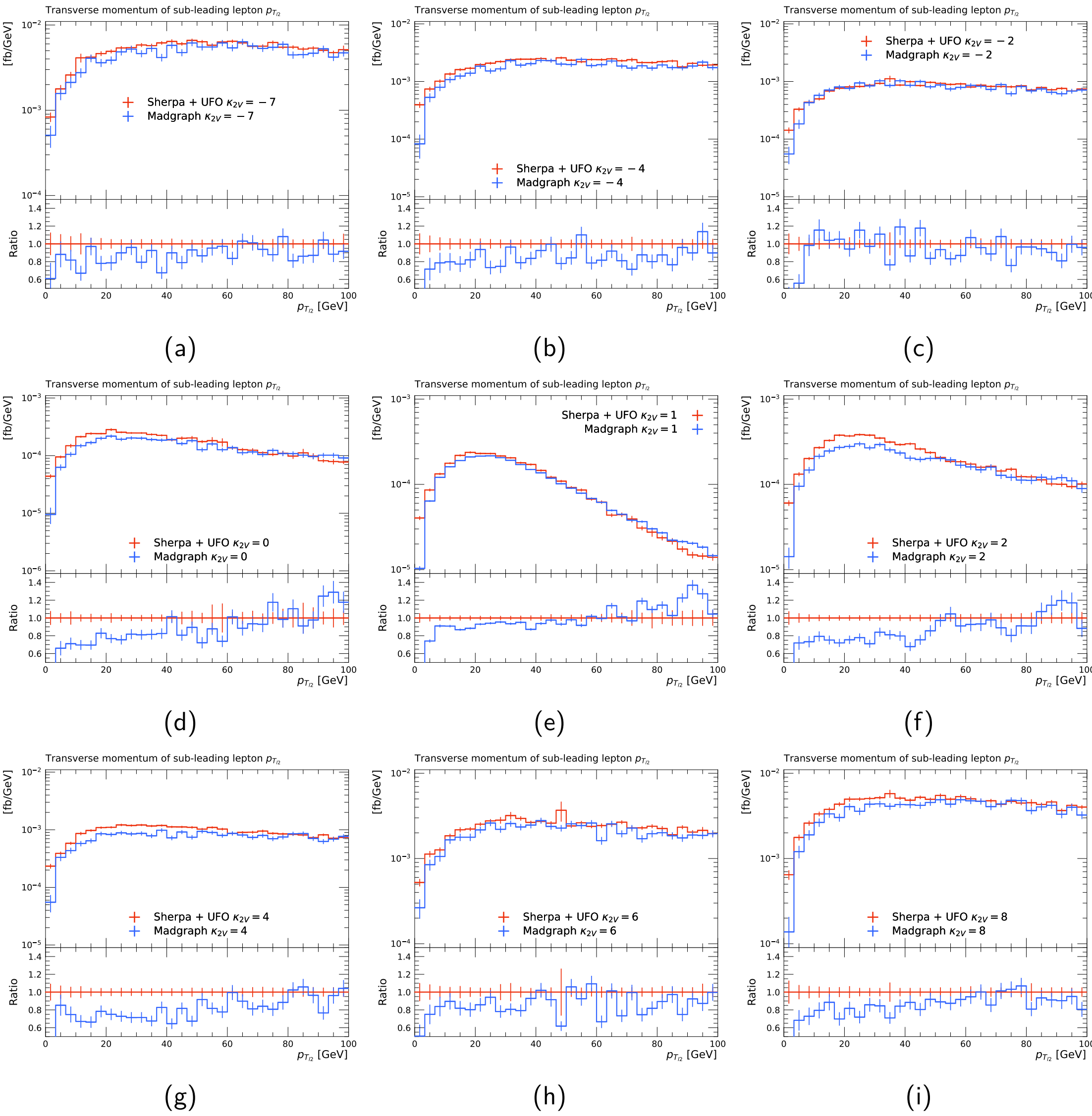

Abbildung 6.4: Comparisons of Madgraph and Sherpa samples for all the $\kappa_{2\mathrm{V}}$ settings regarding the observable $\mathrm{p}_{\mathrm{T},\mathrm{l}_2}$.

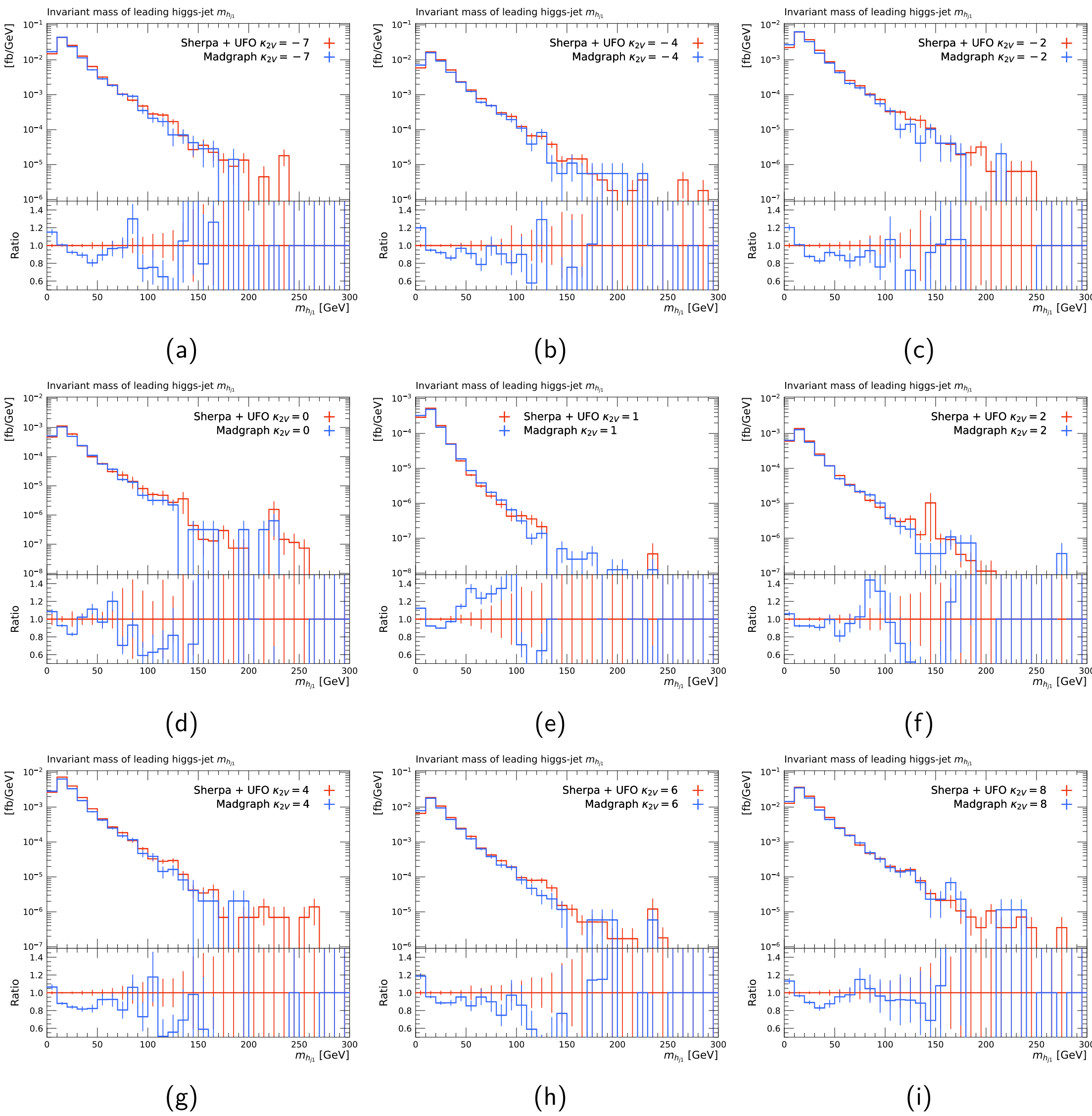

Abbildung 6.5: Comparisons of Madgraph and Sherpa samples for all the $\kappa_{2\mathrm{V}}$ settings regarding the observable $\mathrm{m_{hj_1}}$.

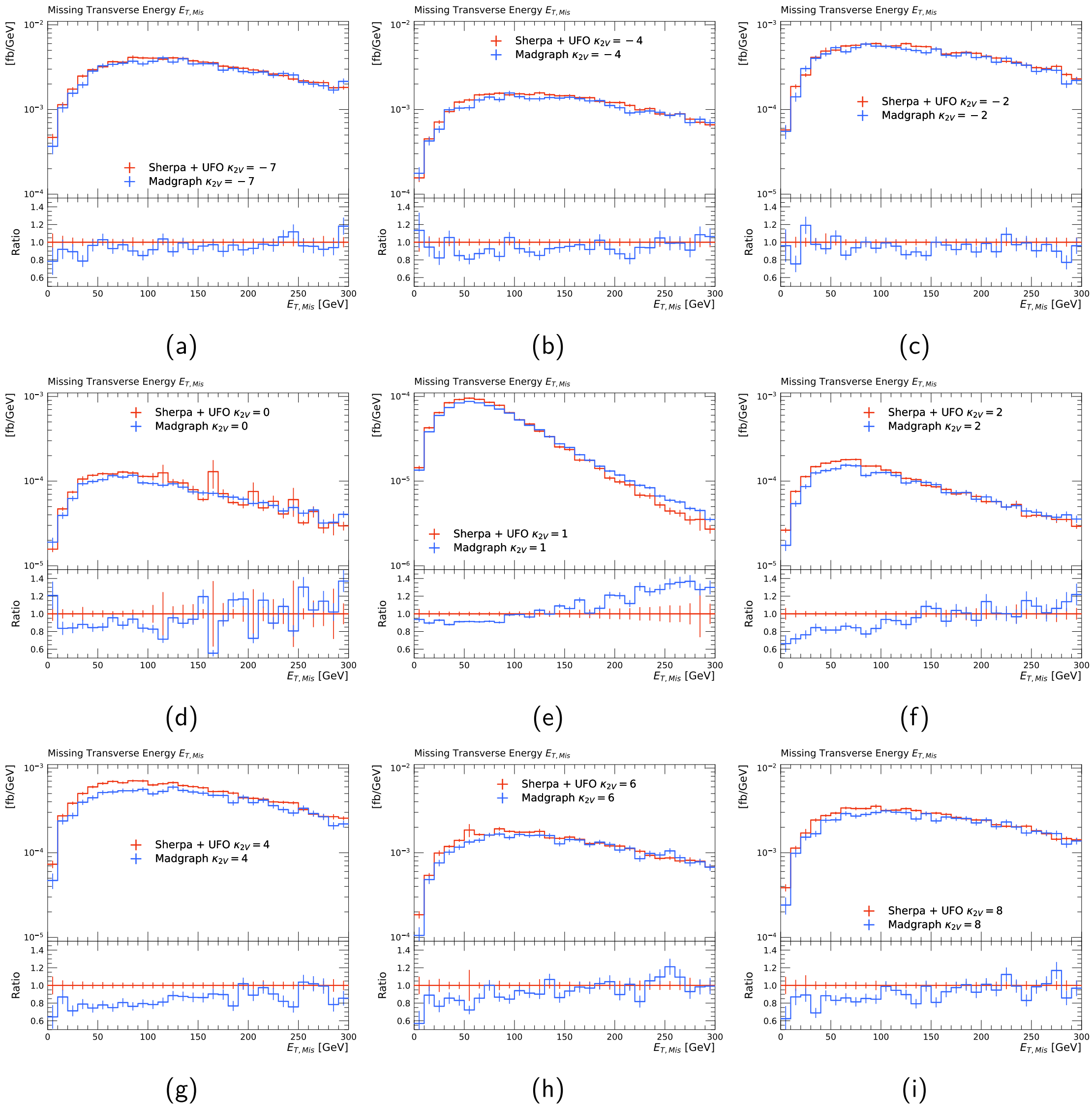

Abbildung 6.6: Comparisons of Madgraph and Sherpa samples for all the $\kappa_{2\mathrm{V}}$ settings regarding the observable $\mathrm{E}_{\mathrm{T,Miss}}$.

Literatur

[1] R. Akhoury, M. G. Sotiropoulos und V. I. Zakharov. “Kinoshita-Lee-Nauenberg theorem and soft radiation in gauge theories: Abelian case”. In: *Physical Review D* 56.1 (Juli 1997), S. 377–387. ISSN: 1089-4918. DOI: 10.1103/physrevd.56.377. URL: http://dx.doi.org/10.1103/PhysRevD.56.377.

[2] CMS Collaboration Alberto Zucchetta. *Searches for rare Higgs boson processes with the CMS detector*. Presenation held at: EPS-HEP 2025. Marseille, July 7. 2025.

[3] Christian Bierlich u. a. *Robust Independent Validation of Experiment and Theory: Rivet version 4 release note*. 2024. arXiv: 2404.15984 [hep-ph]. URL: https://arxiv.org/abs/2404.15984.

[4] Fady Bishara, Roberto Contino und Juan Rojo. “Higgs pair production in vector-boson fusion at the LHC and beyond”. In: *The European Physical Journal C* 77.7 (Juli 2017). ISSN: 1434-6052. DOI: 10.1140/epjc/s10052-017-5037-9. URL: http://dx.doi.org/10.1140/epjc/s10052-017-5037-9.

[5] Andy Buckley u. a. “Rivet user manual”. In: *Computer Physics Communications* 184.12 (Dez. 2013), S. 2803–2819. ISSN: 0010-4655. DOI: 10.1016/j.cpc.2013.05.021. URL: http://dx.doi.org/10.1016/j.cpc.2013.05.021.

[6] Maren Buhring. *Validating Sherpa for New Physics Simulations in Diboson Processes*. Mai 2023.

[7] Matteo Cacciari, Gavin P Salam und Gregory Soyez. “The anti-ktjet clustering algorithm”. In: *Journal of High Energy Physics* 2008.04 (Apr. 2008), S. 063–063. ISSN: 1029-8479. DOI: 10.1088/1126-6708/2008/04/063. URL: http://dx.doi.org/10.1088/1126-6708/2008/04/063.

[8] CERN. *ATLAS Experiment*. accessed on 18.06.2025. 2024. URL: https://home.cern/science/experiments/atlas.

[9] CERN. *Our History*. https://home.cern/about/who-we-are/our-history. accessed on 18.06.2025.

[10] CERN. *The CERN Accelerator Complex*. CERN-Brochure-2021-004-Eng. 2021. URL: https://cds.cern.ch/record/2809109/files/CERN-Brochure-2021-004-Eng.pdf.

[11] Michael S. Chanowitz und Mary K. Gaillard. “The TeV physics of strongly interacting W’s and Z’s”. In: *Nuclear Physics B* 261 (1985), S. 379–431. ISSN: 0550-3213. DOI: https://doi.org/10.1016/0550-3213(85)90580-2. URL: https://www.sciencedirect.com/science/article/pii/0550321385905802.

[12] CMS-Collaboration. “Limits on the Higgs boson lifetime and width from its decay to four charged leptons”. In: *Physical Review D* 92.7 (Okt. 2015). ISSN: 1550-2368. DOI: 10.1103/physrevd.92.072010. URL: http://dx.doi.org/10.1103/PhysRevD.92.072010.

[13] ATLAS Collaboration. "Search for boosted VBS W ±W ± h production in final states with leptons and b-jets at $\sqrt{s}$ =13 TeV using full Run 2 data". In preparation. 2025.

[14] ATLAS Collaboration. "Search for non-resonant Higgs boson pair production in the $2b + 2\ell + E_T^{miss}$final state in pp collisions at $\sqrt{s} = 13\,\mathrm{TeV}$ with the ATLAS detector". In: *Journal of High Energy Physics* 2024.2 (Feb. 2024). ISSN: 1029-8479. DOI: 10.1007/jhep02(2024)037. URL: http://dx.doi.org/10.1007/JHEP02(2024)037.

[15] Sherpa Collaboration. *Event generation with Sherpa 3*. 2024. arXiv: 2410.22148 [hep-ph]. URL: https://arxiv.org/abs/2410.22148.

[16] The ATLAS Collaboration. "The ATLAS Experiment at the CERN Large Hadron Collider". In: *Journal of Instrumentation* 3.08 (Aug. 2008), S08003. DOI: 10.1088/1748-0221/3/08/S08003. URL: https://dx.doi.org/10.1088/1748-0221/3/08/S08003.

[17] A. Denner und T. Hahn. "Radiative corrections to W+W− → W+W− in the electroweak standard model". In: *Nuclear Physics B* 525.1 (1998), S. 27–50. ISSN: 0550-3213. DOI: https://doi.org/10.1016/S0550-3213(98)00287-9. URL: https://www.sciencedirect.com/science/article/pii/S0550321398002879.

[18] Christoph Englert u. a. *VBS* $W^{\pm}W^{\pm}H$ *production at the HL-LHC and a 100 TeV pp-collider*. 2017. arXiv: 1702.01930 [hep-ph]. URL: https://arxiv.org/abs/1702.01930.

[19] J. R. Espinosa, C. Grojean und M. Mühlleitner. "Composite Higgs search at the LHC". In: *Journal of High Energy Physics* 2010.5 (Mai 2010). ISSN: 1029-8479. DOI: 10.1007/jhep05(2010)065. URL: http://dx.doi.org/10.1007/JHEP05(2010)065.

[20] Nicoletta Garelli. "Performance of the ATLAS Detector in Run-2". In: *EPJ Web Conf.* 164 (2017), S. 01021. DOI: 10.1051/epjconf/201716401021. URL: https://cds.cern.ch/record/2310929.

[21] Tanju Gleisberg und Stefan Höche. "Comix, a new matrix element generator". In: *Journal of High Energy Physics* 2008.12 (Dez. 2008), S. 039–039. ISSN: 1029-8479. DOI: 10.1088/1126-6708/2008/12/039. URL: http://dx.doi.org/10.1088/1126-6708/2008/12/039.

[22] Fred James. "Monte Carlo theory and practice". In: *Reports on Progress in Physics - REP PROGR PHYS* 43 (Sep. 1980), S. 1145–1189. DOI: 10.1088/0034-4885/43/9/002.

[23] Lisa Lehmann. "Sensitivity study on the Higgs boson's trilinear self-coupling with the VBS ssWWh signal at the ATLAS detector". Magisterarb. TU Dresden, 2024.

[24] Tao Liu u. a. "Probing the quartic Higgs boson self-interaction". In: *Physical Review D* 98.9 (Nov. 2018). ISSN: 2470-0029. DOI: 10.1103/physrevd.98.093004. URL: http://dx.doi.org/10.1103/PhysRevD.98.093004.

[25] Kristin Lohwasser. *The W Charge Asymmetry: Measurement of the Proton Structure with the ATLAS detector*. Mai 2010.

[26] S. Navas u. a. "Review of particle physics". In: *Phys. Rev. D* 110.3 (2024), S. 030001. DOI: 10.1103/PhysRevD.110.030001.

[27] Schweizerischer Nationalfonds. *Vorwort*. accessed on 18.06.2025. 2023. URL: https://www.lhc-facts.ch/.

[28] Michael H. Seymour und Marilyn Marx. *Monte Carlo Event Generators*. 2013. arXiv: 1304.6677 [hep-ph]. URL: https://arxiv.org/abs/1304.6677.

[29] Frank Siegert. "Monte-Carlo event generation for the LHC". Diss. Durham University, 2010.

[30] Torbjörn Sjöstrand, Stephen Mrenna und Peter Skands. "PYTHIA 6.4 physics and manual". In: *Journal of High Energy Physics* 2006.05 (Mai 2006), S. 063–065. ISSN: 1029-8479. DOI: 10.1088/1126-6708/2006/05/026. URL: http://dx.doi.org/10.1088/1126-6708/2006/05/026.

[31] Stefan Prestel. *MC event generator introduction*. https://indi.to/dM6Sv. CTEQ-MCnet summer school 2021. 2021.

[32] Mark Thomson. *Modern Particle Physics*. Cambridge University Press, 2013.

[33] Stefanie Todt. "The $\mathrm{W}^{\pm}\mathrm{W}^{\pm}$ Scattering Process – Theoretical Studies, Observation, Cross-section Measurement, and EFT Reinterpretation at $\sqrt{\mathrm{s}} = 13$ TeV with the ATLAS Detector". chapter 2.2.2. Diss. Dresden, Tech. U., Sep. 2022.

[34] C. S. Wu u. a. "Experimental Test of Parity Conservation in Beta Decay". In: *Phys. Rev.* 105 (4 Feb. 1957), S. 1413–1415. DOI: 10.1103/PhysRev.105.1413. URL: https://link.aps.org/doi/10.1103/PhysRev.105.1413.

Abbildungsverzeichnis

Acknowledgments

The last page of this thesis shall be dedicated to all the people that helped and supported me in any shape or form with this project.
First i want to thank Frank Siegert for having me in his group. Thank you for helping me out when ever it seemed like there were unsurpassable technical difficulties and for getting me back on track when ever i got sidetracked.
Then i want to thank Orcun Kolay and Maren Bühring, for being the first people that i could address to help me with any issues in setting up Sherpa, writing my first Rivet analysis or just to help me wrap my head around any physical concept.
I also want to thank Alexandro Martone for introducing me into the κ-framework and for supplying me with the Madgraph samples used in this thesis.
I also want to thank Tim Herrmann, Mareen Hoppe, Erik Bachmann and Philip Sommer for the feedback on my first drafts of this thesis. It was much appreciated.
At last i want to thank my girlfriend, my brother and my parents for all the support and the understanding in the time of writing this project down.

Eigenständigkeitserklärung

Hiermit erkläre ich, dass ich die vorliegende Arbeit im Rahmen der Betreuung am Institut für Kern- und Teilchenphysik ohne unzulässige Hilfe Dritter verfasst habe und alle verwendeten Quellen als solche gekennzeichnet habe.

Ort, Datum Unterschrift